Department of Engineering Science, University of Oxford

Direct Wavefront Sensing in Adaptive Microscopy

Saad Azmeen-ur-Rahman
Jesus College, Oxford

Trinity Term, 2012

A thesis submitted for the degree of Master of Science by Research at the University of Oxford

بِسْمِ ٱللَّهِ ٱلرَّحْمَٰنِ ٱلرَّحِيمِ

Abstract

Specimen-induced aberrations are frequently encountered in high resolution microscopy, particularly when high numerical aperture lenses are used to image deep into biological specimens. These aberrations distort the focal spot causing reduction in resolution, signal level and contrast. Aberrations arise due to refractive index variations in the specimen. Adaptive optics has been used in microscopes to correct for these effects and restore optimum imaging performance. An adaptive element, such as a deformable mirror, is used to compensate for aberrations by introducing equal but opposite phase distortions to that introduced by the specimen. Most adaptive optics systems in microscopy have employed indirect optimisation schemes that require several exposures of the specimen before the correction phase can be determined. This could lead to photo-toxicity and is sometimes unsuitable for real-time imaging. Direct wavefront sensing can significantly decrease the time required for aberration measurements by using dedicated sensors, but has limitations, particularly when backscattered light is used from thick specimens. While similar research has been undertaken in ophthalmology where the imaged retina is approximately two-dimensional, this report extends that work to three-dimensional specimens in microscopes. Aberration correction has already been demonstrated in single-pass systems for scattering specimens, but have employed either indirect wavefront sensing techniques or fluorescent beads as guide stars. The use of a Shack-Hartmann wavefront sensor for direct wavefront sensing using backscattered light in a dual-pass system is investigated here. Out-of-focus rejection using an axial selectivity pinhole is studied, along with the phase smoothing effect that is dependant on the pinhole size. The effectiveness of using asymmetric illumination and detection paths, and polarisation filtering in the retrieval of phase information are also demonstrated. It is shown that whilst direct quantitative measurements are not possible for scattering specimens, the measurements could be used in closed-loop adaptive optics systems to correct aberrations.

Acknowledgements

I am thankful to all the individuals in the Scanning Optical Microscopy group with whom I have crossed paths and had many discussions on optics and cricket, namely, Dr. Rimas Juškaitis, Dr. Edward Botcherby, Dr. Anisha Kubasik-Thayil, Dr. Alexander Corbett, Dr. Patrick Salter, Dr. Brian Patton, Dr. Daniel Burke and Dr. Christopher Smith. I would also like to thank the many visitors to Oxford - Biru Wang, Tao Liu, Emiliano Ronzitti and Lionel Fafchamps for their help and friendship.

I am grateful to Prof. Tony Wilson for his support during my first year. I am immensely grateful to Dr. Alexander Jesacher for all the help and advice he has provided in and out of the lab, and likewise to Dr. Simon Tuohy, with whom I have also enjoyed following cricket updates, and in particular, the Ireland-Bangladesh rivalry. I would also like to thank the EPSRC and the University of Oxford for funding my project, and the staff at Jesus College for their support and guidance.

I am very thankful for the friendship of Richard Simmonds, with whom I have spent hours dipping biscuits in tea and discussing a plethora of topics in the lab. I cannot express how grateful I am to my friends Mary Ngo, Imtiaj Murshed, Amer Reza, Tanvir Hussain, Rania Shahjahan, Zahid Rizve, Maruf Ahmed, Mash-Hud Iqbal, Abdul Quyyum, Fahad Rahman, Naif Islam, Saddika Haque, Dr. Dipayan Das and John Sulaitis for their support.

I am eternally indebted to Dr. Martin Booth for his patience and support. Words cannot express how grateful I am for his guidance and advice, and for the many hours he has invested in helping me get to this point.

I am grateful to my brothers Tamim Rahman, Areez Rahman and Antares Rahman, and Mehreen Syed for their support in every way, to Sadiqur Rahman and Syeeda Rahman for taking care of me all these years while I am away from home, and to all my family members for their support, prayers and warm wishes at all times.

Finally, I am and will forever be indebted and grateful to my parents for everything.

Table of Contents

List of Abbreviations

2D	two-dimensional
3D	three-dimensional
AFP	actual focal position
AO	adaptive optics
CARS	coherent anti-stokes Raman scattering
CCD	charge-coupled device
CoG	centre of gravity
DM	deformable mirror
FLC	ferroelectric liquid crystal
IR	infrared
IWC	intensity weighted centroiding
IWCoG	iteratively weighted centre of gravity
LCSLM	liquid crystal spatial light modulator
MEMS	microelectromechanical systems
NA	numerical aperture
NFP	nominal focal position
NLC	nematic liquid crystal
OPL	optical path length
PMT	photomultiplier tube
PSF	point spread function
RMS	root mean square
SHWS	Shack-Hartmann wavefront sensor
SLM	spatial light modulator
SNR	signal-to-noise ratio
SPIM	selective plane illumination microscope
SVD	singular value decomposition
THG	third harmonic generation
WCoG	weighted centre of gravity
WS	wavefront sensor

Chapter 1

Introduction

Various high resolution optical microscopes are used in the biomedical sciences. The confocal microscope is of particular interest as it provides three-dimensional (3D) images of volume specimens through optical sectioning methods. Other methods include wide-field sectioning and non-linear microscopy like two-photon, Third Harmonic Generation (THG) and Coherent anti-Stokes Raman Scattering (CARS). Often scientists are interested in obtaining images of structures in the depths of specimens rather than on the surface. However, resolution, signal level and contrast of images tend to diminish while going deeper into specimens due to the introduction of distortions known as aberrations. Aberrations can occur due to imperfections in the optical equipment, refractive index mismatches of media that light traverses, and can also be introduced by the specimen itself. In an optical system, such as the confocal microscope, aberrations cause the deformation of the focal spot responsible for imaging. Consequently, image quality degrades. The effects of aberrations tend to be worse when using objective lenses with high numerical apertures (NA) corresponding to a larger focussing angle in optical microscopes [1, 2].

Adaptive optics (AO) is a promising technology that allows the correction of aberrations [2, 3, 4]. The system measures aberrations by methods of wavefront sensing. Direct wavefront sensing can be performed employing instruments like the Shack-Hartmann wavefront sensor (SHWS). Otherwise, indirect optimisation methods [5, 6, 7, 8] can be used to determine the best signal in an optical system. AO then corrects the aberrations using an adaptive element, such as, a spatial light modulator (SLM) or a deformable mirror (DM). The technology has been used extensively in astronomy since the 1990s to correct images from telescopes, where atmospheric turbulence is the main source of aberrations. However, the inception of AO in microscopy was only about ten years ago.

Most AO systems implemented so far in microscopy have used indirect optimisation methods [5, 6, 7, 8], which have been successfully demonstrated in a number of microscopes. These indirect schemes require several exposures of the specimen before the correction aberrations can be determined, which could lead to photo-toxicity, particularly in fluorescence microscopes that use fluorescence labels. Contrastingly, direct wavefront sensing can measure aberrations in a short exposure and without any optimisation algorithm, hence avoiding the problems associated with indirect methods. However, direct sensing is not necessarily straightforward. Firstly, measurements are affected by out-of-focus light due to the 3D structure of specimens, for which some form of out-of-focus rejection is required [9, 10]. Secondly, the measured aberrations vary depending on the structure of specimens [11, 12]. It would, however, be useful to perform wavefront sensing using scattered light. Since fluorescence is not used, there is a lower chance of being affected by photo-toxicity. It was therefore decided to investigate the use of direct wavefront sensing using scattered light.

A SHWS was used in this project, chosen for its commercial availability, ease of use and vibration insensitivity, to investigate the use of light backscattered from specimens in a confocal reflection microscope. However, the results are in principle applicable to any epi-illumination microscope, such as two-photon or wide-field microscopes. The effects of specimen structure on wavefront measurements were studied. In particular, the difference between the measured and induced aberrations was investigated, and various schemes were introduced in order to improve the effectiveness of wavefront measurements. The following sections will discuss the basic concepts of microscopy and AO, which will lead onto the main aspects of this report in the later chapters.

1.1 Optical Microscopy

1.1.1 Conventional Wide-Field Microscope

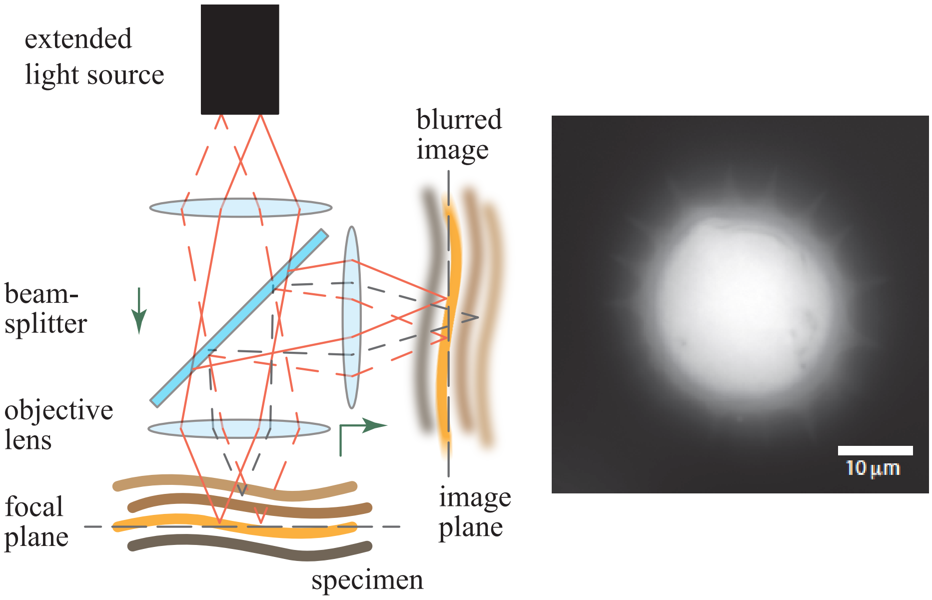

(a) (b)

Figure 1.1: (a) Schematic of a conventional wide-field microscope. Light from an extended light source uniformly illuminates a specimen. Reflected light forms an image of the illuminated part of the specimen. Out-of-focus light superimposes on in-focus detail, resulting in a blurred image. (b) Conventional fluorescence image of a pollen grain showing blurring due to out-of-focus light. Courtesy of Dr. R. Juškaitis and Dr. E. Botcherby.

Fig. 1.1a shows a simple schematic of a conventional wide-field optical microscope in reflection mode. In the microscope above, light from an extended source is focussed by an objective lens so as to illuminate a specimen uniformly (hence, wide-field) in the focal plane. Light is reflected by the specimen from the focal plane and collected by the objective lens. A portion of the collected light is separated by a beam-splitter, and an image is then formed in the image plane. The image can be viewed by eye or projected onto an image capture device. Inevitably, if the specimen extends in three dimensions, all parts of the specimen in the optical path are illuminated. Subsequently, out-of-focus light (light from depths other than the focal plane) is also reflected by the specimen, as shown with the grey dashed lines, which superimposes on the light gathered from the focal plane and appears as a blur in the image, hence obscuring the in-focus detail. Fig. 1.1b shows the image of a pollen grain obtained using a conventional fluorescence microscope.

1.1.2 Confocal Microscope

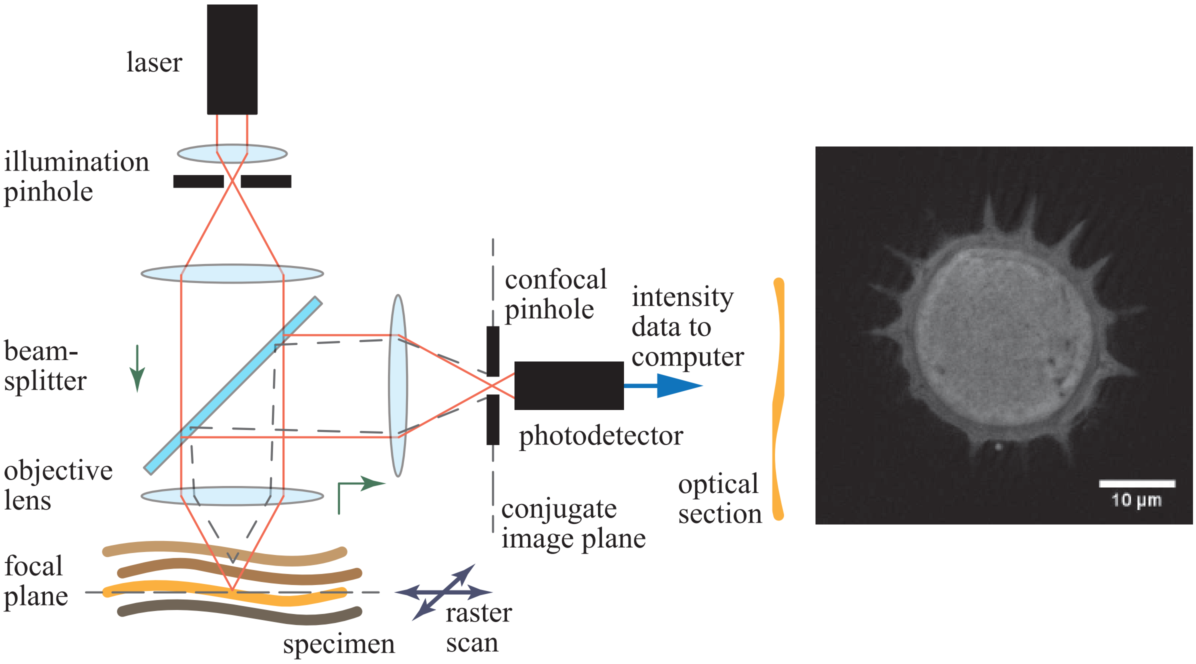

(a) (b)

Figure 1.2: (a) Schematic of a confocal reflection microscope. Light from a point source is focussed to a point into a specimen. Reflected light is collected by a photodetector through a confocal pinhole to image that point in the focal plane. The specimen is scanned to form an image of a plane within the specimen called an optical section. (b) Confocal fluorescence image of a pollen grain. An optical section is shown. Specimen detail can be observed due to out-of-focus rejection. Courtesy of Dr. E. Botcherby.

A confocal microscope can eliminate out-of-focus blur and acquire in-focus images from selected depths of a specimen. Fig. 1.2a shows a simple schematic of a confocal reflection microscope. In a confocal microscope, a laser source illuminating a pinhole acts as a point source of light, which is focussed by an objective lens to a spot in the focal plane at a desired depth within a specimen. The axial position (position along the depth) of the specimen can be adjusted by changing the position of the focal plane within the specimen to image the specimen at various depths. Light is scattered or reflected from that point by the specimen and collected by the same objective lens. Since the same objective lens is used for illumination and detection, the system is referred to as epi-illumination. Consequently, as light passes through the same parts twice, it is also referred to as dual-pass. A portion of the collected light is separated by a beam-splitter and focussed by a lens on a second pinhole that acts as a spatial filter. It is termed as a confocal pinhole as it is placed in a conjugate focal plane (another plane where the points in the illumination plane are perfectly imaged) to the plane of point illumination, and hence the term confocal microscopy arises. Light that passes through the confocal pinhole is collected by a photodetector, such as a photomultiplier tube (PMT) or an avalanche photodiode, which generates a signal proportional to the intensity of the reflected light, and thereby images the point on the specimen.

As the grey dashed lines in the diagram show, most of the out-of-focus light is blocked by the confocal pinhole. Subsequently, images with greatly enhanced axial resolution are obtained compared to those from a conventional microscope. This effect can be noticed by comparing Fig. 1.1b and Fig. 1.2b. More detail can be seen in the confocal image of the pollen grain in the latter figure. This process of depth selectivity using a spatial filter is known as optical sectioning.

The specimen is placed on a computer-controlled stage that performs the task of scanning the specimen relative to the laser focus. Alternatively, in a beam-scanning system, instead of moving the specimen, light is swept across it using rotating mirrors. In a raster or lateral scan, light from the specimen forms a sequence of points on a two-dimensional plane, which can be formed into an image of the plane in the specimen by an appropriate computer software, as illustrated in the diagram. Fig. 1.2b shows an optical section of a pollen grain under a confocal fluorescence microscope. A computer can then render a 3D or extended depth of field image of the specimen by assembling a stack of the optical sections from successive depths. Fig. 1.3 illustrates how optical sections from the image stack of a pollen grain can be combined to form an extended depth of field image.

A confocal microscope can operate in various different modes. In contrast to the reflection mode shown in Fig. 1.2a, light transmitting through a specimen is collected by another objective, called a collector, and used to form an image in a confocal transmission microscope. Such a system is referred to as dia-illumination. Compared to the dual-pass system, as light passes through the specimen only once, it is also called a single-pass system. The confocal microscope can also operate in fluorescence mode, which requires

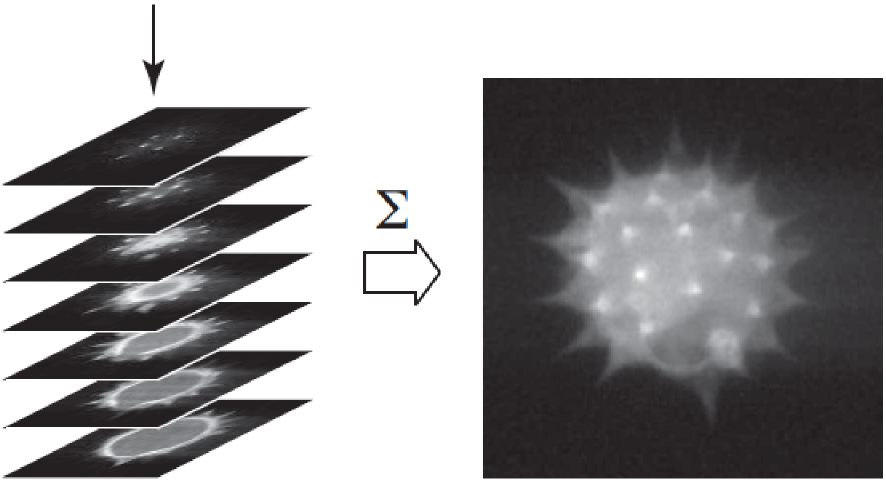

Figure 1.3: Stack of optical sections of confocal fluorescence images of a pollen grain. Images of two-dimensional (2D) optical sections from successive planes form an image stack. Half of the stack is used to create an extended depth of field image of the pollen. Courtesy of Dr. R. Juškaitis and Dr. E. Botcherby.

the labelling of specimens with fluorescence dyes. The dyes excite specimens to radiate light at different wavelengths, subsequently causing their detection.

1.1.3 Two-Photon Microscope

The two-photon microscope [13] is a fluorescence imaging system that utilises the non-linear nature of the absorption of two photons in the focal region by fluorophores embedded in a specimen. Fig. 1.4a shows a simple schematic of a two-photon microscope, which is similar to the confocal microscope shown in Fig. 1.2a, except that a confocal pinhole is not required.

When two photons carrying approximately half the energy necessary to excite a fluorophore are simultaneously absorbed, a fluorescence photon is emitted with approximately twice the energy than that of each excitatory photon. Consequently, the wavelength produced in the detection path is approximately half of the illumination wavelength. The probability of the simultaneous absorption of two photons is proportional to the square of the illumination intensity. As a result, two-photon fluorescence essentially occurs at the focus of the objective lens, giving the two-photon microscope its inherent optical sectioning capability. The fluorescent emission from the focal region at the new wavelength

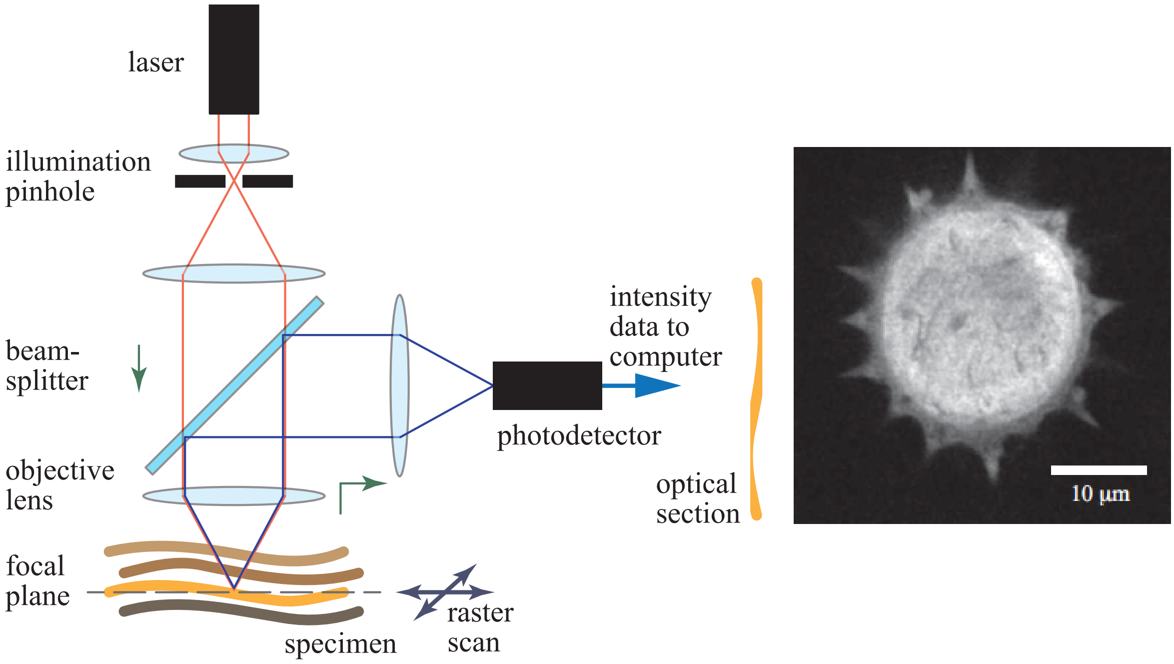

(a) (b)

Figure 1.4: (a) Schematic of a two-photon microscope. Two photons absorbed at the focus by a fluorophore cause fluorescent emission of a single photon that is collected by a photodetector to image that single point. The specimen is scanned, similar to the confocal microscope, to attain an optical section. (b) Two-photon image of a pollen grain. Courtesy of Dr. E. Botcherby.

is separated using a dichroic beam-splitter and detected using a photodetector, such as a PMT. By scanning the specimen, optical sections and 3D images can be achieved in a two-photon microscope similarly to a confocal microscope. Fig. 1.4b shows a two-photon optical section of a pollen grain.

Ultrashort pulsed lasers are used to achieve a high flux of photons at the focus, typically, femtosecond lasers. Commonly used fluorophores emit fluorescence in the 400 – 700nm wavelength range. Hence, infrared (IR) lasers are usually used to provide an illumination wavelength of around 700 – 1000nm. The degree of scattering depends strongly on the wavelength, such that the shorter wavelengths are much more strongly scattered than the longer ones. Using IR rather than visible light therefore reduces the scattering effect, and deeper penetration and efficient light detection are achieved over confocal microscopy. Photobleaching is also reduced, compared to confocal fluorescence microscopy, due to absorption being limited to a tight region within the focal spot.

Although the AO techniques discussed later in this report were demonstrated using the confocal reflection microscope, they are equally applicable for a two-photon microscope owing to the epi-illumination nature of the confocal and two-photon systems.

1.2 Diffraction-Limited Imaging

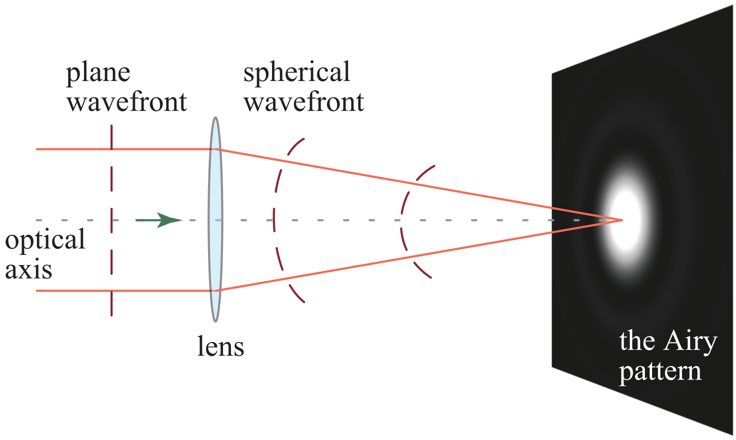

Figure 1.5: The Airy pattern. Due to diffraction by a lens, incident plane waves converge to a diffraction-limited spot called the Airy pattern [14]. The Airy pattern consists of a bright central spot surrounded by dimmer concentric rings. The central spot in the image is saturated to show the detail of the dimmer surrounding.

The phenomenon of the deviation of light from the predictions of geometrical optics during propagation is known as the diffraction of light. According to geometrical optics, light passing through a lens focusses to an infinitesimally small point in the focal plane, and light reflected back from that point in a specimen will perfectly reproduce an image of that point. But in practice, a collimated beam (beam consisting of plane waves or flat wavefronts) incident on a lens is diffracted to form a beam of converging spherical waves, as Fig. 1.5 illustrates. The waves converge to a bright spot containing about 80% of the incident energy surrounded by dimmer concentric rings in the radial direction, which is known as the Airy pattern [14]. The central spot is called the Airy disc. The size of the Airy disc determines the resolution of an imaging system, and any system producing this focal spot is said to be diffraction-limited.

1.3 Aberrations in Microscopy

Optical sectioning greatly improves imaging in a confocal microscope and enables 3D imaging. However, imaging encounters other distortions, especially when imaging deep within a volume specimen. Deviations of an optical system from the ideal diffraction-limited form cause distortion of the focus. These deviations are known as aberrations.

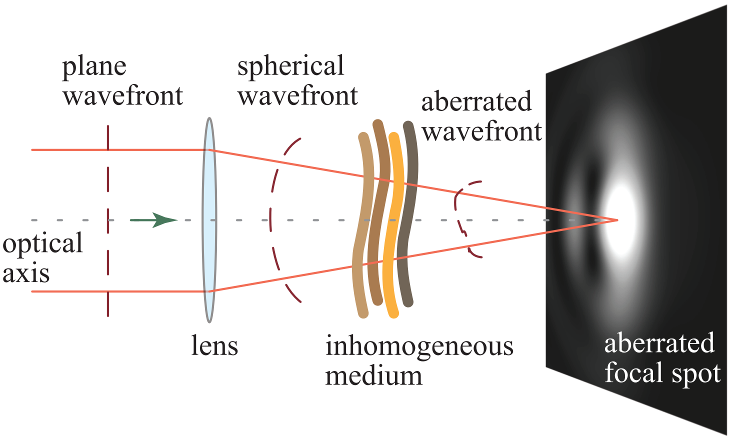

Figure 1.6: Distorted focal spot. As light is focussed through a specimen, converging spherical waves are distorted, and an aberrated focal spot is produced. The central spot in the image is saturated to show the detail of the dimmer surrounding.

It is known that the speed of light changes when travelling from one medium to another of a different refractive index, and as a consequence that it refracts. Therefore, if a collimated beam propagates through an inhomogeneous medium (medium with spatially varying refractive indices), different parts of a wavefront will travel at different speeds, thus resulting in a distorted or aberrated wavefront. In the same way, as light focusses through a specimen, as Fig. 1.6 shows, spherical waves are distorted, hence resulting in an aberrated focal spot. Comparing with the Airy pattern in Fig. 1.5, the illustration shows a focal spot that has been enlarged and deformed due to aberrations. Such a spot will produce images of poor resolution and quality.

1.4 Adaptive Optics

Adaptive optics (AO) is a technology used to achieve optimal imaging performance in systems affected by aberrations. It involves the measurement of aberrations by some method of analysing the wavefront, referred to as wavefront sensing, and then compensating for it using an adaptive element. The latter process of correcting aberrations is termed as adaptive correction.

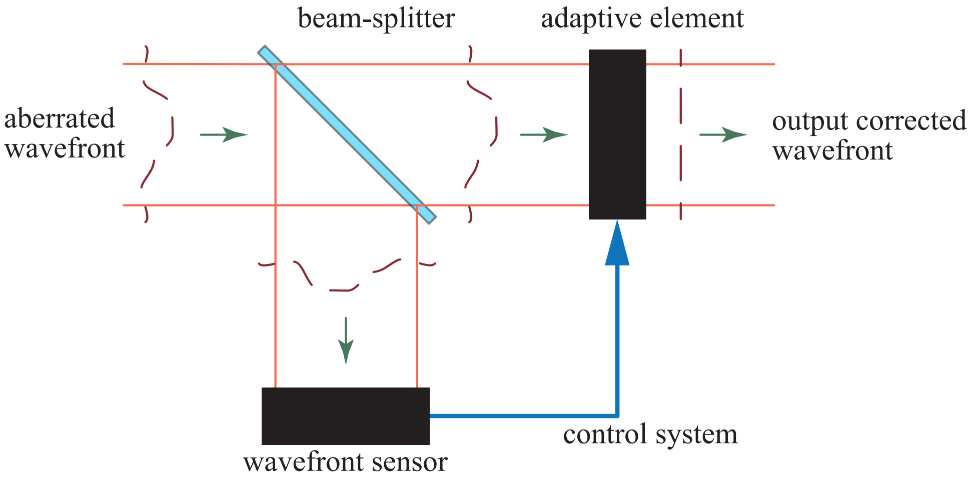

Figure 1.7: Schematic of a conventional AO system. A wavefront sensor analyses the structure of incoming wavefronts, and a control system accordingly compensates aberrations using an adaptive element.

Fig. 1.7 shows a simple AO system. The property of such a system is its ability to acquire phase information of incident wavefronts directly using a wavefront sensor (WS), such as the Shack-Hartmann wavefront sensor (SHWS) [3, 15]. In the diagram, aberrated light is split and coupled into a WS and an adaptive element. The WS estimates the shape of incident wavefronts. The adaptive element is some form of a spatial light modulator (SLM) or deformable mirror (DM), that can alter the shape of incident wavefronts in its transmission path. A control system, usually some hardware and specially programmed software, uses information from the WS to control the adaptive element and alter wavefronts in the transmission path so as to produce near-flat wavefronts [3, 16]. Thereby, aberrations are compensated and diffraction-limited imaging is restored in a AO system. It must be noted that Fig. 1.7 shows an open-loop system. Many systems are implemented in closed-loop, where the adaptive element is placed before the beam-splitter and WS, such as the wavefront sensing system discussed later in this report.

1.5 Motivation for this Project

Various methods exist for the measurement of wavefront phase. These include interferometry or the use of sensors like the SHWS and pyramid WS. Experiments conducted for large-optics metrology applications have shown that data retrieved from a SHWS closely matched that of a phase-shifting interferometer [17]. In fact, the interferometric data was prone to diffraction artefacts that were absent in the Shack-Hartmann data. Interferometric methods, in particular, are incompatible with various averaging schemes that may otherwise allow the detection of certain aberrations from backscattered light. SHWS has been employed for AO in single-pass systems [18] and ophthalmic studies [19]. Coherence-gated wavefront sensing has been demonstrated to determine aberrations directly in strongly scattering specimens in two-photon microscopes [20, 21]. Similarly, this project attempts to perform direct wavefront sensing from backscattered light in a dual-pass set-up. However, the system presented here is far easier to implement than the coherence-gated system. Backscattered light is always present in imaging systems and is essentially unused. This light could be coupled off and used for wavefront sensing without any extra photo-toxic or bleaching effects.

The goal of the research, presented in this report, is to investigate whether direct wavefront sensing could be used to detect aberrations from backscattered light. The project extends the work done in ophthalmic AO to 3D specimens in scanning optical microscopy. The research investigates the effects of specimen structure on aberration measurements by inducing known amounts of aberrations using a deformable mirror, and measuring the aberrations in the detection path using a SHWS. Various averaging schemes are investigated that may allow improved determination of aberrations. The consequences of using a pinhole for out-of-focus rejection in direct wavefront sensing are explored and the effects of pinhole sizes are studied. The effects of using asymmetric illumination and detection in a dual-pass optical system and polarisation filtering in the determination of aberrations are also investigated.

Chapter 2

Diffraction Theory

Diffraction theory describes how the wave nature of light affects the propagation of light fields. Diffraction theory is essential in accurately modelling the properties of optical systems, where geometrical or ray optics is no longer valid. It is a prerequisite to understand the imaging performance of an optical imaging system that operates near the diffraction limit of light.

This chapter introduces the concept of diffraction of light as consequences of its wave nature as postulated by Huygens and Fresnel, followed by the quantitive description of diffraction based on Kirchhoff and Rayleigh-Sommerfeld diffraction theories. The paraxial approximation to the diffraction formulae is discussed, which simplifies optical models. The formulae are used to illustrate the intensity distribution of the aberration-free focal spot and factors contributing to resolution are discussed. Finally, the chapter leads on to Fourier optics and the $4f$ system, which are essential to model the optical systems used for the experiments.

2.1 Huygens-Fresnel Principle

The Huygens-Fresnel principle describes each point on the wavefront of a disturbance to be a new source of a secondary spherical disturbance such that a wavefront at a later

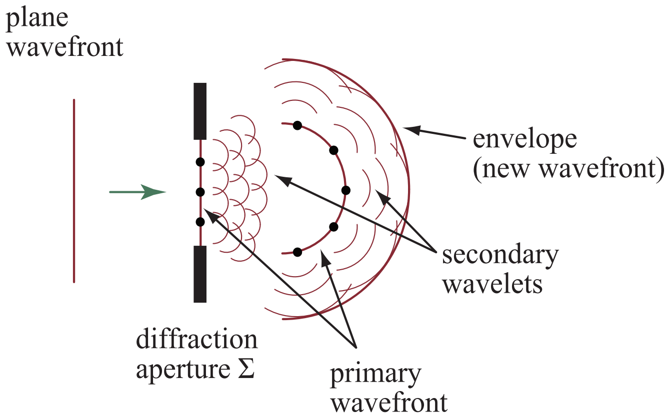

Figure 2.1: Illustration of the principle of the Huygens-Fresnel construction. Each point on the primary wavefront is a source of secondary spherical wavelets that superimpose to form subsequent wavefronts.

instant can be constructed by the envelope of the secondary wavelets, as diagrammatically illustrated in Fig. 2.1. This principle provides the mathematical basis for the formulation of a diffraction integral in which optical wavefronts are propagated through space.

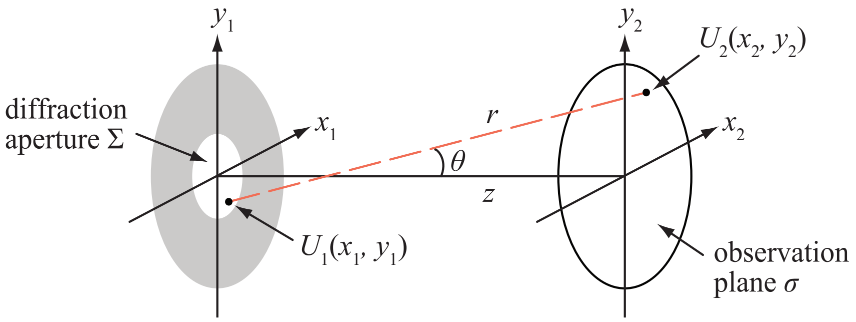

Figure 2.2: Diffraction geometry explaining the Huygens-Fresnel principle. Spherical wavelets in the diffraction plane (x_1, y_1) contribute to the image in the observation plane (x_2, y_2).

If the geometry shown in Fig. 2.2 is considered, light is obstructed by a diffraction aperture Σ in the diffraction plane (x_1, y_1) and a pattern in observed in the observation plane σ with coordinates (x_2, y_2). A diverging spherical wavelet of radius r originating from any point P_1 in the diffraction aperture can be mathematically represented as:

$$\frac{e^{-jkr}}{r}, \tag{2.1}$$

where the wave number k is defined as:

$$k = \frac{2\pi}{\lambda}. \tag{2.2}$$

If $U_1(x_1, y_1)$ represents the amplitude of illumination at P_1, by definition of the Huygens-Fresnel principle, the total amplitude of waves $U_2(x_2, y_2)$ at any point P_2 in the observation plane can be expressed as an integration of the wavelets originating from the aperture with respect to the aperture area Σ as:

$$U_2(x_2, y_2) = C \iint_{\Sigma} \frac{e^{-jkr}}{r} U_1(x_1, y_1)\, \mathrm{d}x_1\, \mathrm{d}y_1, \tag{2.3}$$

where C is a constant determined by the law of conservation of energy.

2.2 Rayleigh-Sommerfeld Diffraction Theory

The Huygens-Fresnel principle provides a good qualitative prediction of the diffraction of light. Accurate formulae can be derived by solving the Helmholtz wave equation derived from Maxwell's equations [22]. If $U_1(x_1, y_1)$ is now considered as a complex field in the diffraction aperture, the complex field $U_2(x_2, y_2)$ at any point in the observation plane can be determined by solving the Helmholtz equation and is given by [22]:

$$U_2(x_2, y_2) = -\frac{j}{\lambda} \iint_{-\infty}^{\infty} U_1(x_1, y_1) \frac{e^{-jkr}}{r} \cos\theta\, \mathrm{d}x_1\, \mathrm{d}y_1. \tag{2.4}$$

Eq. (2.4) is known as the Rayleigh-Sommerfeld diffraction integral. The complex-valued scalar field U for a monochromatic wave of amplitude $A(x, y)$ and phase $\phi(x, y)$ can be expressed as a function of position in (x, y):

$$U(x, y) = A(x, y)e^{-j\phi(x,y)}. \tag{2.5}$$

Although other diffraction formulae exist, the Rayleigh-Sommerfeld diffraction integral is often used given its similarity in expression with the Huygens-Fresnel principle given by Eq. (2.3). Eq. (2.4) adds an obliquity factor $\cos\theta$ and a $\frac{\pi}{2}$ radian phase shift represented by the imaginary factor j.

2.3 Paraxial Approximation

The diffraction pattern of light for a given aperture depends on the distance between the diffraction aperture and the observation plane. Very close to the aperture, the pattern is almost a projection of the aperture with slight fringing around the edges. At an intermediate distance, the fringes become more pronounced and the structure of the pattern changes with distance. This is known as Fresnel diffraction. Farther away from the aperture, the structure of the pattern no longer changes, but its size does. The pattern is known as Fraunhofer diffraction. The following sections discuss the Fresnel and Fraunhofer diffraction patterns and the conditions under which they form.

2.3.1 Fresnel Approximation

The paraxial approximation is assumed in most diffraction cases when light wave propagates along a direction which is close to the optical axis to reduce expressions to a simpler form. Accordingly, when the observation point P_2 is close to the optical axis, the distance r can be reduced using the binomial expansion $\sqrt{1+b} \approx 1 + \frac{b}{2}$:

$$\begin{aligned} r &= \sqrt{z^2 + (x_2 - x_1)^2 + (y_2 - y_1)^2} \\ &= z\sqrt{1 + \left(\frac{x_2 - x_1}{z}\right)^2 + \left(\frac{y_2 - y_1}{z}\right)^2} \\ &\approx z\left[1 + \frac{1}{2}\left(\frac{x_2 - x_1}{z}\right)^2 + \frac{1}{2}\left(\frac{y_2 - y_1}{z}\right)^2\right]. \end{aligned} \tag{2.6}$$

Eq. (2.6) is called Fresnel approximation. Under the paraxial approximation, the following conditions can be assumed:

$$\begin{cases} r \approx z, \\ \theta \to 0 \implies \cos\theta \to 1. \end{cases} \tag{2.7}$$

Using the approximations, the Rayleigh-Sommerfeld diffraction integral defined by Eq. (2.4) can be reduced to:

$$U_2(x_2, y_2) = -\frac{j}{\lambda z} e^{-jkz} \iint_{-\infty}^{\infty} U_1(x_1, y_1) e^{-\frac{jk}{2z}[(x_2-x_1)^2+(y_2-y_1)^2]} \, \mathrm{d}x_1 \, \mathrm{d}y_1, \tag{2.8}$$

which can be used to calculate the Fresnel diffraction pattern in the near-field. The intensity distribution of the pattern can be calculated by taking the squared modulus of the field:

$$I = |U(x, y)|^2. \tag{2.9}$$

The quadratic phase variation in the diffraction plane makes the calculation of Fresnel diffraction complicated. It is responsible for the changing structure of the Fresnel pattern as the distance between the diffraction aperture and the observation plane changes within the Fresnel region. Due to the paraxial approximation, Eq. (2.8) is not valid for diffraction very close to the aperture, where the angle θ will be larger and there will be considerable difference between z and r.

2.3.2 Fraunhofer Approximation

If the observation screen is farther away from the diffraction aperture such that it can be assumed:

$$z \gg \frac{k\,(x_1^2 + y_1^2)}{2}, \tag{2.10}$$

then the quadratic phase factor $e^{-\frac{jk}{2z}\left(x_1^2+y_1^2\right)}$, in Eq. (2.8), is approximately unity over the diffraction aperture. Hence, it can be assumed that the quadratic phase factor related to the diffraction plane changes by negligible amount within the region in the aperture that contributes significantly to the field at the corresponding point of the diffraction pattern. Subsequently, the equation used to calculate the Fraunhofer diffraction pattern in the far-field is given by:

$$U_2(x_2, y_2) = -\frac{j}{\lambda z} e^{-jkz} e^{-\frac{jk}{2z}(x_2^2+y_2^2)} \iint_{-\infty}^{\infty} U_1(x_1, y_1) e^{\frac{jk}{z}(x_1x_2+y_1y_2)} \, \mathrm{d}x_1 \, \mathrm{d}y_1, \tag{2.11}$$

As it is evident from Eq. (2.11), there are no non-linear phase variations in the integral, which describes why the Fraunhofer pattern only changes in size with distance and not in structure. Aside from the pre-multiplicative phase factors, the equation can be recognised as the 2D Fourier transform of the complex aperture distribution $U_1(x_1, y_1)$.

2.4 Diffraction by a Thin Lens

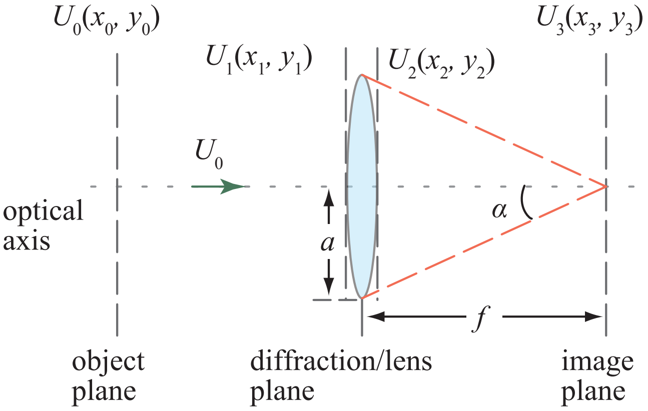

Figure 2.3: Diffraction by a positive bi-convex lens, which is composed of two spherical surfaces.

As Fig. 2.3 shows, a simple lens can be made of two spherical surfaces. When light passes through such a lens, it refracts and the change in optical path causes a phase change. The amplitude of the wave also changes due to the Fresnel reflection and transmission, although these effects are often small and can be neglected [22]. To simplify calculations, a lens is considered to be optically thin such that the lateral displacement of the beam passing through the lens is negligible. Therefore, the complex transmittance of a thin lens is given by:

$$t(x, y) = P(x, y) e^{\frac{jk}{2f}(x^2+y^2)}, \tag{2.12}$$

where f is the geometrical focal length of the lens. $P(x, y)$ is known as the pupil function and it represents the amplitude change in incident light confined to the aperture of the lens. The term $e^{\frac{jk}{2f}(x^2+y^2)}$ represents a quadratic phase function that is a paraxial approximation to the spherical phase change introduced by the lens.

Referring to Fig. 2.3, if $U_1(x_1, y_1)$ and $U_2(x_2, y_2)$ are the fields immediately before and after the lens, respectively, and plane wave of amplitude U_0 is incident on the lens, then the field immediately before the lens becomes:

$$U_1(x_1, y_1) = U_0. \tag{2.13}$$

Due to the phase and amplitude variation introduced by the lens, the field immediately after the lens is:

$$U_2(x_2, y_2) = U_0 P(x_2, y_2) e^{\frac{jk}{2f}(x_2^2+y_2^2)}. \tag{2.14}$$

A lens acts as a diffraction screen with the addition of the phase and amplitude changes described above. Therefore, using the Fresnel diffraction formula given by Eq. (2.8), the distribution in the back focal plane of the lens where $z = f$ is:

$$U_3(x_3, y_3) = -\frac{j}{\lambda f} U_0 e^{-jkf} e^{-\frac{jk}{2f}(x_3^2+y_3^2)} \iint_{-\infty}^{\infty} P(x_2, y_2) e^{\frac{jk}{f}(x_3 x_2 + y_3 y_2)} \, \mathrm{d}x_2 \, \mathrm{d}y_2, \tag{2.15}$$

where the quadratic phase factors within the integral cancel out. Comparing with Eq. (2.11), clearly the lens produces the Fraunhofer diffraction pattern of the pupil function $P(x, y)$ in its back focal plane, and the integral in Eq. (2.15) is the 2D Fourier transform of $P(x, y)$ at spatial frequencies of $\frac{x_3}{\lambda f}$ and $\frac{y_3}{\lambda f}$.

If the observation plane is out-of-focus by a distance Δz such that the distance of the plane from the lens is $z = f + \Delta z$, the distribution in the out-of-focus plane in the vicinity of the focal plane is given by the Fresnel diffraction formula defined by Eq. (2.8):

$$U_3(x_3, y_3) = -\frac{j}{\lambda z} U_0 e^{-jkz} \iint_{-\infty}^{\infty} P(x_2, y_2) e^{\frac{jk}{2f}(x_2^2+y_2^2)} e^{-\frac{jk}{2z}[(x_3-x_2)^2+(y_3-y_2)^2]} \, \mathrm{d}x_2 \, \mathrm{d}y_2. \tag{2.16}$$

2.5 Imaging with a Single Lens

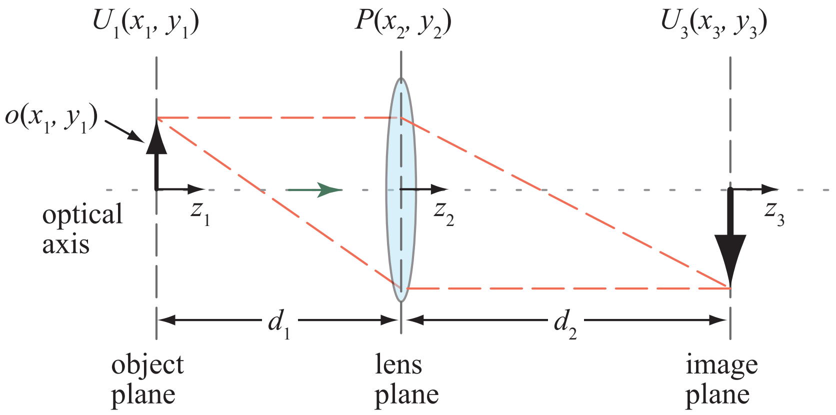

Figure 2.4: Imaging with a single lens. An object placed at a distance d_1 in front of the lens is imaged inverted at a distance d_2 behind the lens.

To analyse imaging by a single lens, the system in Fig. 2.4 is considered. A thin object of amplitude transmittance of $o(x_1, y_1)$ is placed in the object plane (x_1, y_1) at a distance d_1 from the lens situated in the lens plane (x_2, y_2). The object acts as a diffraction screen and hence, using the Fresnel diffraction formula given by Eq. (2.8), the field immediately before the lens is:

$$U_2(x_2, y_2) = -\frac{j}{\lambda d_1} e^{-jkd_1} \iint_{-\infty}^{\infty} o(x_1, y_1) e^{-\frac{jk}{2d_1}[(x_2-x_1)^2+(y_2-y_1)^2]} \, \mathrm{d}x_1 \, \mathrm{d}y_1. \tag{2.17}$$

Applying the transmittance of the lens given by Eq. (2.12), the field immediately after the lens is, therefore:

$$U_2'(x_2, y_2) = -\frac{j}{\lambda d_1} e^{-jkd_1} P(x_2, y_2) e^{\frac{jk}{2f}(x_2^2+y_2^2)} \iint_{-\infty}^{\infty} o(x_1, y_1) e^{-\frac{jk}{2d_1}[(x_2-x_1)^2+(y_2-y_1)^2]} \, \mathrm{d}x_1 \, \mathrm{d}y_1. \tag{2.18}$$

Substituting Eq. (2.18) into the Fresnel diffraction formula in Eq. (2.8) yields the field in the image plane (x_3, y_3) and leads to the equation:

$$\begin{aligned} U_3(x_3, y_3) = -\frac{e^{-jk(d_1+d_2)}}{\lambda^2 d_1 d_2} e^{-\frac{jk}{2d_2}(x_3^2+y_3^2)} \iiiint_{-\infty}^{\infty} & P(x_2, y_2) o(x_1, y_1) e^{-\frac{jk}{2d_1}(x_1^2+y_1^2)} \\ & e^{\frac{jk}{2}\left(\frac{1}{f}-\frac{1}{d_1}-\frac{1}{d_2}\right)(x_2^2+y_2^2)} \\ & e^{\frac{jk}{d_1}\left[x_2\left(x_1+\frac{d_1}{d_2}x_3\right)+y_2\left(y_1+\frac{d_1}{d_2}y_3\right)\right]} \,\mathrm{d}x_1 \,\mathrm{d}y_1 \,\mathrm{d}x_2 \,\mathrm{d}y_2. \end{aligned} \tag{2.19}$$

The expression gives a general relation between an object and its image formed by a lens. Eq. (2.19) can be further simplified by considering the lens law used in geometrical optics that defines the distances d_1 and d_2 required for an in-focus image. The lens law defines:

$$\frac{1}{d_1} + \frac{1}{d_2} = \frac{1}{f}, \tag{2.20}$$

whereby suitable distances before and after the lens can be determined for in-focus image such that the term $e^{\frac{jk}{2}\left(\frac{1}{f}-\frac{1}{d_1}-\frac{1}{d_2}\right)(x_2^2+y_2^2)}$ in Eq. (2.19) can be eliminated. Demagnification of the system can be defined as:

$$M = \frac{d_1}{d_2}. \tag{2.21}$$

Therefore, Eq. (2.19) simplifies to:

$$\begin{aligned} U_3(x_3, y_3) = -\frac{M e^{-jkd_1\left(1+\frac{1}{M}\right)}}{\lambda^2 d_1^2} e^{-\frac{jkM}{2d_1}(x_3^2+y_3^2)} \iint_{-\infty}^{\infty} & o(x_1, y_1) e^{-\frac{jk}{2d_1}(x_1^2+y_1^2)} \\ & h(x_1 + Mx_3, y_1 + My_3) \,\mathrm{d}x_1 \,\mathrm{d}y_1, \end{aligned} \tag{2.22}$$

where the 2D Fourier transform of the pupil function $P(x_2, y_2)$ in Eq. (2.19) is defined as:

$$h(x, y) = \iint_{-\infty}^{\infty} P(x_2, y_2) e^{\frac{jk}{d_1}(x_2 x + y_2 y)} \,\mathrm{d}x_2 \,\mathrm{d}y_2. \tag{2.23}$$

Considering a single point object on the optical axis, which can be modelled using the Dirac delta function as:

$$o(x_1, y_1) = \delta(x_1)\delta(y_1), \tag{2.24}$$

the image of the point object can be found using Eq. (2.22) as:

$$U_3(x_3, y_3) = -\frac{Me^{-jkd_1\left(1+\frac{1}{M}\right)}}{\lambda^2 d_1^2} e^{-\frac{jkM}{2d_1}(x_3^2+y_3^2)} h(Mx_3, My_3). \tag{2.25}$$

Ignoring the phase factors in Eq. (2.25), it can be clearly seen that $h(Mx_3, My_3)$ represents the image of a point. Therefore $h(x, y)$, as defined by Eq (2.23), gives the complex amplitude of the light field and is called the 2D amplitude point spread function or simply the point spread function (PSF). For perfect imaging, $h(x, y)$ should be equivalent to the delta function. In practice, the PSF should be as narrow as possible in order to produce an image that best represents the object.

A further approximation can be made that x_1^2 and y_1^2 are small compared to $2d_1/k$ and therefore the exponential term in the integrand is approximately 1. So the quadratic phase term in the integral of Eq. (2.22) can be simplified to give:

$$U_3(x_3, y_3) = -\frac{Me^{-jkd_1\left(1+\frac{1}{M}\right)}}{\lambda^2 d_1^2} e^{-\frac{jkM}{2d_1}(x_3^2+y_3^2)(1+M)} \iint_{-\infty}^{\infty} o(x_1, y_1) \\ h(x_1 + Mx_3, y_1 + My_3)\,\mathrm{d}x_1\,\mathrm{d}y_1. \tag{2.26}$$

As the intensity distribution in the image plane is of interest in imaging, the pre-multiplicative constants and phase factors can be dropped. Subsequently, the field in the image plane can be finally expressed simply as:

$$U_3(x_3, y_3) = \iint_{-\infty}^{\infty} o(x_1, y_1) h(x_1 + Mx_3, y_1 + My_3)\,\mathrm{d}x_1\,\mathrm{d}y_1, \tag{2.27}$$

which can be identified as a 2D convolution of the transmittance of the thin object with the PSF for the lens, and can thus be written using the convolution operator $\otimes$ as:

$$U_3 = o \otimes h. \tag{2.28}$$

Hence, the image of an object is the superposition of a series of PSFs formed as the images of each point on the object whose intensities are determined by the transmittance $o(x_1, y_1)$. This shows that the quality of the image and its resolution are determined by the properties of the PSF. A narrower PSF results in less blurring between images of neighbouring points and higher resolution is obtained.

2.6 3D Point Spread Function

As the PSF plays a vital role in the quality and resolution of imaging, it is of utmost importance to extend the concept of PSF into three dimensions to understand image formation of volume specimens.

Since a practical lens is circularly symmetric, its pupil function is only a function of the radial coordinate. Aberrations may break this symmetry, but rotational symmetry is assumed for simplicity in the present analysis. Hence, it is convenient to use polar coordinates such that:

$$\begin{cases} P(x, y) = P(r), \\ r = \sqrt{x^2 + y^2}, \end{cases} \tag{2.29}$$

where $P(r)$ can be considered a uniform circular aperture of radius a and expressed as:

$$P(r) = \begin{cases} 1, & r \leq a, \\ 0, & \text{otherwise}. \end{cases} \tag{2.30}$$

Since the 2D PSF was obtained as the Fresnel diffraction of the pupil function in the image plane, it follows that the 3D PSF can be calculated using the Fresnel diffraction formula for a lens given by Eq. (2.16). Consequently, taking $U_0 = 1$, the distribution in the back focal plane of a lens is given by Eq. (2.16) and therefore, the 3D PSF can be expressed in polar coordinates as:

$$U_3(r_3) = -\frac{j}{\lambda z} e^{-jkz} e^{-\frac{jk}{2z} r_3^2} \int_0^\infty P(r_2) e^{\frac{jk}{2} r_2^2 \left(\frac{1}{f} - \frac{1}{z}\right)} J_0\left(\frac{k r_2 r_3}{z}\right) 2\pi r_2 \, \mathrm{d}r_2, \tag{2.31}$$

where J_0 is a Bessel function of the first kind of order zero defined as:

$$J_0(x) = \frac{1}{2\pi} \int_0^{2\pi} e^{\pm jx\cos\theta}\, \mathrm{d}\theta. \tag{2.32}$$

From Eq. (2.31), the out-of-focus pupil function can be defined as:

$$P(r_2, z) = P(r_2) e^{\frac{jk}{2} r_2^2 \left(\frac{1}{f} - \frac{1}{z}\right)}, \tag{2.33}$$

so that Eq. (2.31) can be simplified to:

$$U_3(r_3) = -\frac{j}{\lambda z} e^{-jkz} e^{-\frac{jk}{2z} r_3^2} \int_0^{\infty} P(r_2, z) J_0\left(\frac{k r_2 r_3}{z}\right) 2\pi r_2 \,\mathrm{d}r_2, \tag{2.34}$$

Introducing the normalised coordinates — u for the axial optical coordinate, v for the transverse (radial) optical coordinate in the observation plane and ρ for the radial coordinate in the lens plane, and the Fresnel number N:

$$\begin{cases} u = ka^2 \left(\dfrac{1}{f} - \dfrac{1}{z}\right) \approx k\Delta z \dfrac{a^2}{f^2}, \\ v = k r_3 \dfrac{a}{z} \approx k r_3 \dfrac{a}{f}, \\ \rho = \dfrac{r_2}{a}, \\ N = \dfrac{\pi a^2}{\lambda f}, \end{cases} \tag{2.35}$$

where the approximation $z \approx f$ has been used since $\Delta z \ll f$ in the vicinity of the focal region. The pupil function can be redefined as:

$$P(\rho) = \begin{cases} 1, & \rho \leq a, \\ 0, & \text{otherwise.} \end{cases} \tag{2.36}$$

Using the definitions above, the normalised 3D PSF is given by:

$$U_3(v, u) = -2jN e^{-jkf} e^{-\frac{jv^2}{4N}} \int_0^1 e^{\frac{ju\rho^2}{2}} J_0(v\rho)\rho \,\mathrm{d}\rho. \tag{2.37}$$

2.6.1 Intensity Distribution in the Focal Plane

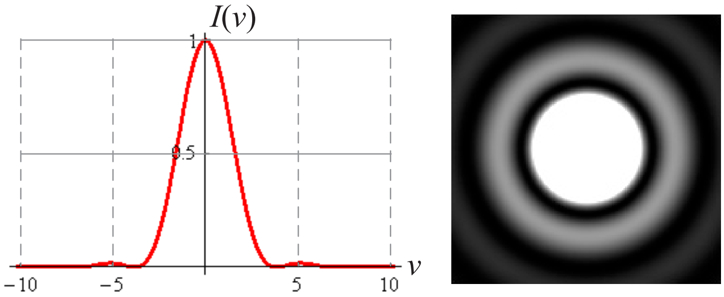

(a) (b)

Figure 2.5: Normalised intensity distribution of the 3D PSF (a) along the radial direction in the focal plane, (b) in the focal plane, which is called the Airy pattern. The figure is saturated in the centre to show the detail in the outer rings.

The intensity distribution of the diffraction spot defined by the PSF can be obtained by applying Eq. (2.9) to Eq. (2.37). Therefore, the field in the focal plane for $u = 0$ is:

$$I(v, u = 0) = |U_3(v, u = 0)|^2 = (\pi N)^2 \left(\frac{2J_1(v)}{v}\right)^2, \tag{2.38}$$

where J_1 is a Bessel function of the first kind of order unity defined as:

$$\int_0^x x_0 J_0(x_0)\,\mathrm{d}x_0 = xJ_1(x). \tag{2.39}$$

Clearly, Eq. (2.38) is the Airy pattern [Sec. 1.2] of a lens [14]. From the normalised intensity profile of the pattern along the radial direction, shown in Fig. 2.5a, it is evident that about 80% of the intensity lies in the Airy disc. The intensity drops to zero at $v \approx 3.83$. The Airy pattern in the focal plane is shown in Fig. 2.5b.

Referring to Fig. 2.3, the numerical aperture (NA) of a lens is given by:

$$NA = n \sin\alpha \approx n\frac{a}{f}. \tag{2.40}$$

where n is the refractive index of the immersion medium of the lens, α is the semi-aperture angle of the lens, and the approximation is valid for small values of α. The NA of a lens represents the angles over which it can converge light — a higher NA corresponds to a larger maximum angle of convergence. Recalling the definition of v in Eq. (2.35), from Eq. (2.38) it can be noted that size of the Airy disc is directly proportional to the wavelength of incident light and inversely proportional to the NA of the lens. Thus, it can be concluded that higher resolution can be obtained using shorter wavelength and higher NA. This relationship is evident from the equation of the diameter of the first zero in the focal plane, that is, of the Airy disc, which is given by [23]:

$$d_0 = \frac{1.22\lambda}{NA}. \tag{2.41}$$

The objective lens is a vital component of any optical microscope as it determines the magnification and resolution of images. Hence, high NA objective lenses are used for high resolution imaging as they produce finer focal spots.

2.6.2 Intensity Distribution in the Axial Plane

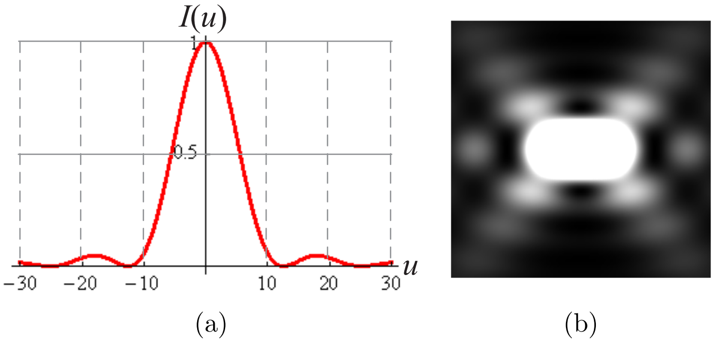

Figure 2.6: Normalised intensity distribution of the 3D PSF (a) on the optical axis, (b) in the axial plane. The figure is saturated in the centre to show the detail in the side lobes.

The intensity distribution of the diffraction spot along the optical axis can be found by substituting $v = 0$ in Eq. (2.37) such that:

$$I(v = 0, u) = |U_3(v = 0, u)|^2 = N^2 \left(\frac{\sin \frac{u}{4}}{\frac{u}{4}} \right)^2. \tag{2.42}$$

Fig. 2.6a shows the intensity profile along the optical axis. The axial size of the diffraction spot is observed to be approximately three times as large as its transverse size in normalised units when compared with Fig. 2.5a, the intensity dropping to zero at $u \approx 12.57$.

The width of the first zero of the spot in the axial direction can be found using Eq. (2.42) and Eq. (2.35), and is given by:

$$w_0 = \frac{4\lambda}{NA^2}. \tag{2.43}$$

Fig. 2.6b shows the intensity distribution in the axial plane. The intensity is noted to be symmetric with respect to the focal plane.

2.7 4f System

Discarding the lens law given by Eq. (2.20) and considering instead the configuration where:

$$d_1 = d_2 = f, \tag{2.44}$$

the relationship of the light fields in the front and back focal planes can be found. Subsequently, Eq. (2.19) reduces to:

$$U_3(x_3, y_3) = -\frac{e^{-2jkf}}{j\lambda f} \iint_{-\infty}^{\infty} o(x_1, y_1) e^{\frac{jk}{f}(x_1 x_3 + y_1 y_3)} \, \mathrm{d}x_1 \, \mathrm{d}y_1, \tag{2.45}$$

which, ignoring the pre-multiplicative phase factor, can be identified as the 2D Fourier transform of the transmittance of the object $o(x_1, y_1)$ evaluated at spatial frequencies of $\frac{x_3}{\lambda f}$ and $\frac{y_3}{\lambda f}$. Therefore, the image in the back focal plane can be said to be the frequency spectrum of the object in the front focal plane. The finite-sized pupil aperture of the lens, which normally takes the form of a circular mask in the Fourier plane, cuts off high frequencies, resulting in the frequency spectrum of the object being low-pass filtered.

An imaging system can be formed using two lenses where the back focal plane of one forms the front focal plane of the other, as illustrated in Fig. 2.7 by the plane (x_2, y_2). The system is aptly named the 4f optical imaging system. For simplicity, a unity magnification system is considered where $f_1 = f_2$. Assuming that the object placed in the front focal plane of the first lens is much smaller than the diameter of the lens and $U_1(x_1, y_1)$ represents the field in that plane, the field in the back focal plane of the lens

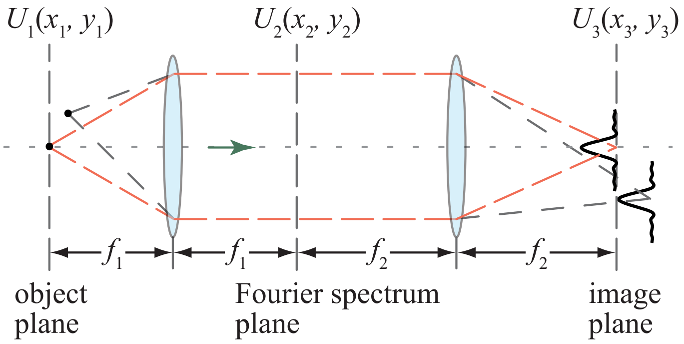

Figure 2.7: Imaging properties of the $4f$ system. An object in the front focal plane of the first lens is imaged in the back focal plane of the second lens.

can be expressed as:

$$U_2(x_2, y_2) = \mathcal{F}\left\{U_1(x_1, y_1)\right\}, \tag{2.46}$$

where $\mathcal{F}$ denotes the 2D Fourier transform given by Eq. (2.45). The back focal plane of the first lens is called the Fourier spectrum plane where the spatial spectrum of the object is observed. $U_2(x_2, y_2)$ is the field in the front focal plane of the second lens. Therefore, the image in the back focal plane of this lens is:

$$U_3(x_3, y_3) = \mathcal{F}\left\{U_2(x_2, y_2)\right\} = U_1(-x_1, -y_1), \tag{2.47}$$

where the minus sign implies that the image is inverted. In practice, the focal lengths of the two lenses may be different such that the demagnification is given by:

$$M = \frac{f_1}{f_2}, \tag{2.48}$$

where f_1 and f_2 are the focal lengths of the first and second lenses, respectively. Consequently, the image by a $4f$ system is given by:

$$U_3(x_3, y_3) = U_1\left(-\frac{x_1}{M}, -\frac{y_1}{M}\right). \tag{2.49}$$

$4f$ systems are vital components in the design of AO systems as they make it is possible to preserve the amplitude and phase distributions of light. In AO systems, the adaptive element, such as a DM, is imaged onto the pupil of the objective lens in this manner.

2.8 Conclusions

This chapter introduced the mathematical foundations for image formation based on the diffraction theory, leading onto Fourier optics. The $4f$ system is, in particular, used extensively to model the various imaging systems used in this project. The 3D model of the focal spot is also of importance in order to investigate the effects of filtering using a pinhole, and to observe the effects the aberrations on the focal spot.

Chapter 3

Optical Microscopy

The confocal microscope offers three-dimensional imaging of volume specimens. This opens up a range of applications, for example, the non-invasive imaging of specimens. Whilst fluorescence microscopes are most widely used in biological investigations, the confocal reflection microscope has been used for the experiments presented in this report as it requires minimal specimen preparation compared to other fluorescence systems. An analysis of the confocal microscope and its depth discrimination property via a pinhole are provided in this chapter, which will be used in the following chapters building up to the dual-pass wavefront sensing system. The incoherent nature of the confocal fluorescence microscope is also briefly discussed.

3.1 Confocal Reflection Microscope

To analyse the confocal reflection microscope [24], it is useful to unfold the optical system in Fig. 1.2a and draw it in a transmission configuration. The microscope can be represented as two $4f$ systems [Sec. 2.7] representing the illumination and detection paths as Fig. 3.1 shows. The $4f$ systems can be considered to behave as single lenses with pupil functions $P_1(m_1, n_1)$ and $P_2(m_2, n_2)$, where (m, n) denote coordinates in the Fourier plane that correspond to the pupil plane. The laser illuminates a pinhole, which acts as a point

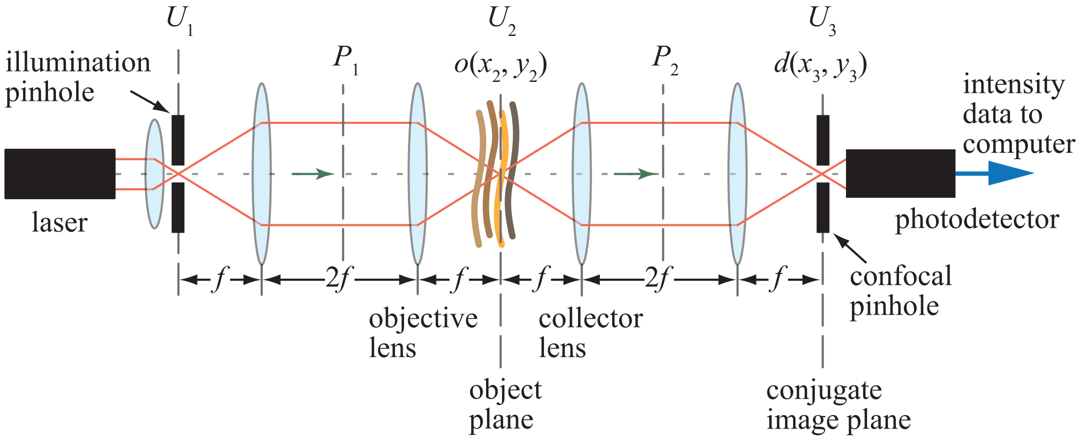

Figure 3.1: Optical arrangement of the confocal reflection microscope unfolded. Two $4f$ systems represent the illumination and the detection paths of the microscope.

source of light, so that:

$$U_1(x_1, y_1) = \delta(x_1)\delta(y_1). \tag{3.1}$$

Subsequently, the objective lens images light from the point source to a focal spot defined by its PSF [Sec. 2.5], where the 2D Fourier transform given by Eq. (2.23) can be written as:

$$h_1(x_2, y_2) = \mathcal{F}\left\{P_1(m_1, n_1)\right\}. \tag{3.2}$$

The focal spot probes a thin specimen with reflectivity spectrum $o(x_2 - x_s, y_2 - y_s)$, where x_s and y_s denote the scanning positions of the specimen with respect to the focal spot position in the (x_2, y_2) plane. The reflected field after interaction with the specimen is, therefore:

$$U_2(x_2, y_2) = h_1(x_2, y_2)o(x_2 - x_s, y_2 - y_s). \tag{3.3}$$

Light reflected from the specimen is collected by the collector lens of pupil function $P_2(m_2, n_2)$. For the purposes of the diagram, this reflected light is shown in the transmission direction. The objective lens effectively images the reflected field into the plane of the detector. Considering unity magnification for simplicity, the field before the detector is given by Eq. (2.27) as:

$$U_3(x_3, y_3) = \int_{y_2}\int_{x_2} h_1(x_2, y_2)o(x_2 - x_s, y_2 - y_s)h_2(x_2 + x_3, y_2 + y_3)\,\mathrm{d}x_2\,\mathrm{d}y_2. \tag{3.4}$$

This field is incident upon a confocal pinhole of transmittance $d(x_3, y_3)$ so that the field reaching the detector is:

$$U_3(x_3, y_3) = d(x_3, y_3) \int\limits_{y_2} \int\limits_{x_2} h_1(x_2, y_2) o(x_2 - x_s, y_2 - y_s) h_2(x_2 + x_3, y_2 + y_3) \, \mathrm{d}x_2 \, \mathrm{d}y_2. \tag{3.5}$$

Ideally, the confocal pinhole behaves as a point source of transmittance:

$$d(x_3, y_3) = \delta(x_3)\delta(y_3), \tag{3.6}$$

so that the field at the detector is given by:

$$U_3(0, 0) = \int\limits_{y_2} \int\limits_{x_2} h_1(x_2, y_2) o(x_2 - x_s, y_2 - y_s) h_2(x_2, y_2) \, \mathrm{d}x_2 \, \mathrm{d}y_2, \tag{3.7}$$

and the detected intensity signal is proportional to the modulus squared of this field. The intensity of the image at any particular scanned position of the specimen can be written using the convolution operator and expressed using Eq. (2.9) as:

$$I(x_s, y_s) = |U_3|^2 = |h_1 h_2 \otimes o|^2, \tag{3.8}$$

where, comparing with Eq. (2.27), it is clear that $h_1 h_2$ is the PSF of the confocal microscope. Since the illumination and detection paths are the same for the confocal reflection microscope so that:

$$h_1 = h_2 = h, \tag{3.9}$$

the amplitude PSF for the confocal reflection microscope is given by h^2, and the intensity of the image is therefore:

$$I(x_s, y_s) = |U_3|^2 = |h^2 \otimes o|^2, \tag{3.10}$$

Finally, the intensities at each point within a 2D plane across a specimen can be gathered by a computer to form an image of a slice through the specimen. Multiple 2D slices can be obtained along the depth of the specimen by scanning along z_2 in the specimen plane, and these slices can be used to render a 3D reconstruction of the specimen structure.

3.2 Confocal Fluorescence Microscope

In confocal fluorescence microscopy, the optical arrangement is unchanged from the set-up shown in Fig. 3.1. Image contrast is achieved by measuring the fluorescence from fluorophores that a specimen is stained with instead of the light that is reflected or scattered back by the specimen. Fluorescence is proportional to the intensity of the illumination light exciting the fluorophores. Assuming no change of wavelength during the fluorescence process, the intensity of the image at any particular point of the specimen is given by [25]:

$$I(x_s, y_s) = |h_1|^2 |h_2|^2 \otimes o_f, \tag{3.11}$$

where, o_f is the fluorescence emitted from the fluorophores at any scanned position. For the epi-illumination system, since the amplitude PSF of the illumination and detection paths are identical, the intensity of the fluorescence image is given by:

$$I(x_s, y_s) = |h|^4 \otimes o_f. \tag{3.12}$$

Phase coherence is lost in confocal fluorescence microscopy due to the dependence of fluorescence on the excitation intensity. It is evident from Eq. (3.11) and Eq. (3.12), where the phase information is lost after measuring the square of the absolute values of the amplitude PSFs. Subsequently, confocal fluorescence microscopy is an incoherent system.

3.3 Depth Discrimination Property of a Pinhole

The size of the confocal pinhole dictates the optical sectioning property of the confocal microscope. While the ideal pinhole is infinitesimally small, as given by Eq. (3.6), such a detector is not practical and too small a pinhole will block most of the light. To investigate the depth discrimination property of a finite-sized circular detector of the coherent confocal microscope, a planar reflector can be modelled to be moved out-of-focus with respect to the focal spot so that the intensity from out-of-focus regions can be calculated as [25]:

$$I(u) = \int |h(2u, v)|^2 d(v)\, \mathrm{d}v, \tag{3.13}$$

where u and v are the normalised coordinates introduced in Eq. (2.35), and $d(v)$ represents the transmittance of the detector pinhole. Note that $2u$ represents the double axial path traversed by the light from the focal region to the planar surface and back.

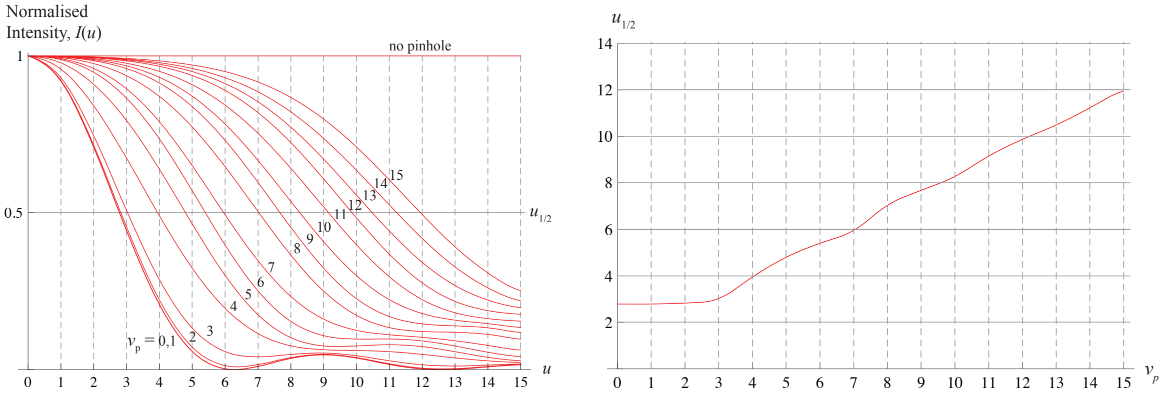

(a) (b)

Figure 3.2: Depth discrimination property of a confocal pinhole of various radii v_p. (a) Variation of normalised intensity against the axial distance u. (b) Half-width of the intensities in Fig. (a) as a function of the normalised detector radius v_p.

Fig. 3.2a illustrates the reduction in the sectioning strength as the pinhole radius v_p increases. The graph shows the fall in intensity, normalised with respect to the maximum central intensity, from out-of-focus regions. As expected, more light is collected farther away from the focal plane as the detector size increases. Fig. 3.2b shows the half-width $u_{\frac{1}{2}}$ of the intensity for the different pinhole sizes. For v_p less than about 2.5, the half-width of the intensity, and hence the depth discrimination, remains constant. Therefore, detector radius satisfying $v_p \leq 2.5$ is required for optical sectioning. Since the intensity of the Airy disc drops at $v \approx 3.83$ [Sec. 2.6.1], it follows that to obtain optimal resolution in confocal microscopy, a very small pinhole of the order of half the diameter of the first zero of the focal spot is used [25]. The actual diameter d_p is given by substituting Eq. (2.35):

$$d_p \leq \frac{2.5\lambda}{M\pi \sin\alpha}, \tag{3.14}$$

where M is the demagnification of the lens system between the object and detector planes given by Eq. (2.48), which arises in the equation above as v_p is measured relative to the object plane.

3.4 Conclusions

This chapter discussed the mathematical model of the confocal reflection microscope and briefly introduced the incoherent confocal fluorescence microscope. The confocal reflection microscope was used in the project to image specimens. The mathematical design of this system is especially important in this project as the AO system is also based on the detection of backscattered or reflected light. The axial depth selection of the confocal pinhole was also discussed, a property that will also be covered in later chapters to investigate the effects of a pinhole in aberration detection.

Chapter 4

Aberrations

In a perfect optical system, light focusses to a small bright spot surrounded by dimmer concentric rings, known as the Airy pattern [Sec. 1.2], represented by the point spread function (PSF) [Sec. 2.5, Sec. 2.6]. This is termed as the diffraction-limited focal spot. In laser scanning optical microscopes and similar systems, a single diffraction-limited spot images a single point in the specimen. The resolution of the image is thus governed by the size of the bright central spot called the Airy disc. Inevitably, inherent imperfections or misalignments in optical systems, refractive index variations encountered while focussing in specimens and various other factors cause light to refract unpredictably. When this light is focussed, the rays do not converge to form the diffraction-limited spot. The focal spot is deformed, enlarged and elongated. This phenomenon is called aberration. Consequently, the aberrated focal spot yields a distorted image of the specimen. Aberrations can severely affect the quality of imaging, particularly in microscopes used for imaging biological specimens, where high NA objective lenses are usually employed. To compensate for aberrations in any optical system, it is therefore vital to be able to represent aberrations mathematically and to isolate the sources of aberrations.

4.1 Phase Aberrations

A wavefront can be represented by the exponential of its phase function Φ as [22, 26]:

$$P'(x, y) = P(x, y)e^{-j\Phi}, \tag{4.1}$$

where $P(x, y)$ is the aberration-free pupil function [Sec. 2.4] and $P'(x, y)$ is the resulting wavefront affected by the phase function Φ. Although aberrations can be introduced at various points along the optical path, they can be modelled using the effective pupil function of an objective lens given by $P'(x, y)$. The phase function of the wavefront gives the phase aberration with respect to an aberration-free reference wavefront.

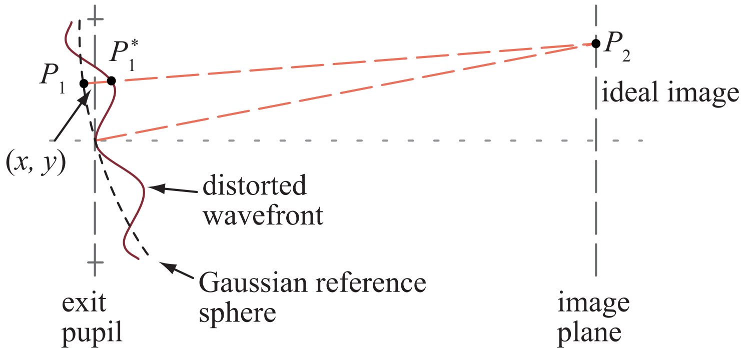

Figure 4.1: Defining phase aberrations. The optical path difference between the distorted and reference wavefronts gives the phase difference caused by aberrations.

Fig. 4.1 shows an ideal image of a point source at the point P_2 in an image plane. Due to aberrations, the wavefront over the lens aperture may not necessarily be spherical. Hence, a Gaussian reference sphere, centred on P_2 and passing through the intersection of the lens aperture and the optical axis, is created to represent the aberration-free wavefront. The difference between the reference sphere and the wavefront is the phase aberration in the system. To quantify this aberration, a ray is traced back from P_2 to an arbitrary point P_1 on the reference sphere. The extension of this line intersects the aberrated wavefront at P_1^*. The aberration is given by the optical path length (OPL), which is defined as the distance between the points P_1 on the reference sphere and P_1^* on the aberrated wavefront. The aberration can also be described in terms of the phase difference Φ of the wavefront as:

$$\Phi = \frac{2\pi}{\lambda} OPL. \tag{4.2}$$

4.1.1 Other Forms of Aberrations

While an emphasis is put on phase aberrations in this report, aberrations can also affect the intensity of detected light. Intensity variations can arise due to absorption of energy by the unwanted out-of-focus layers of the specimen. Such aberrations are referred to as amplitude aberrations and have a smaller effect on image quality than phase aberrations. They cannot be recovered as the light is absorbed or lost. The only way to equalise the amplitude would be to decrease the amplitude of the remaining brighter parts, thus causing more loss. Hence, they can often be neglected.

Another form of aberration is chromatic aberration, which occurs as a consequence of the dispersion of light. As refractive index of a medium varies with the wavelength of light, lenses refract different wavelengths of a broad bandwidth of light at different angles, resulting in dispersion. Subsequently, a lens focusses different wavelengths at different positions. This leads to images of different colours in different places and different aberrations affecting separate wavelengths as they traverse a slightly varied path. Chromatic aberrations are significantly reduced by the use of achromatic or apochromatic lenses, which focus the different wavelengths in the same plane. They are not of concern in optical systems utilising monochromatic sources where the bandwidth is very narrow.

4.2 Sources of Aberrations in Microscopy

Aberrations can arise due to a number of reasons. Some of the main factors contributing to aberrations in microscopy are discussed below.

i. Aberrations occur due to intrinsic imperfections in optical elements. For example, the surfaces of lenses may not be perfect, causing the wavefronts passing through a lens to deviate from their ideal form.

ii. Misalignments in an optical system can contribute to aberrations by transforming low-order aberrations to higher-order ones [3]. For example, a converging beam entering an optical element tilted at an angle will be affected by astigmatism [Sec. 4.3].

iii. If the refractive indices of the immersion medium of the objective lens and that of the specimen do not match, refraction of light at the interface between the media causes induction of spherical aberration [Sec. 4.3]. Objective lenses are generally designed to correct for such mismatches by replacing the gap between the lens and the specimen by an immersion medium matching the refractive index of the immersion medium of the specimen.

iv. Spherical aberration [Sec. 4.3] can also arise if a coverslip of incorrect thickness is used since there is refractive index mismatch between the coverslip glass and the immersion medium [27]. Objective lenses are designed to correct aberrations introduced by coverslips of specific thicknesses. The effect of spherical aberration is particularly significant with high NA lenses.

v. When light is focused deep into a specimen, it passes through layers of the specimen where there may be spatial variations in the refractive index. This causes the light to travel at different speeds through different parts of the specimen and consequently wavefronts become distorted on propagation through the specimen [1, 28, 12].

vi. Small variations in temperature responsible for turbulence cause changes to the refractive index. The cumulative effect of these minute fluctuations can also give rise to aberrations [3].

4.2.1 Effects of Numerical Aperture

Resolution in an optical system is dictated by the size of the focal spot, which is dependent on the wavelength and NA [Sec. 2.6.1]. The wavelength is usually restricted by the available light source or specimen properties that require illumination by a fixed wavelength. Therefore, higher resolution is obtained by increasing the NA. Eq. (2.40) shows that the NA is directly proportional to the refractive index n of the medium light focusses through and the converging angle α of the focussing cone. The immersion medium, and therefore the refractive index, is determined by the specimen. For example, biological specimens tend to be water-based and so objective lenses designed for water as the immersion medium are used. Using a different immersion medium will induce unwanted spherical aberration [Sec. 4.3]. Subsequently, high NA is obtained using lenses with large focussing angles.

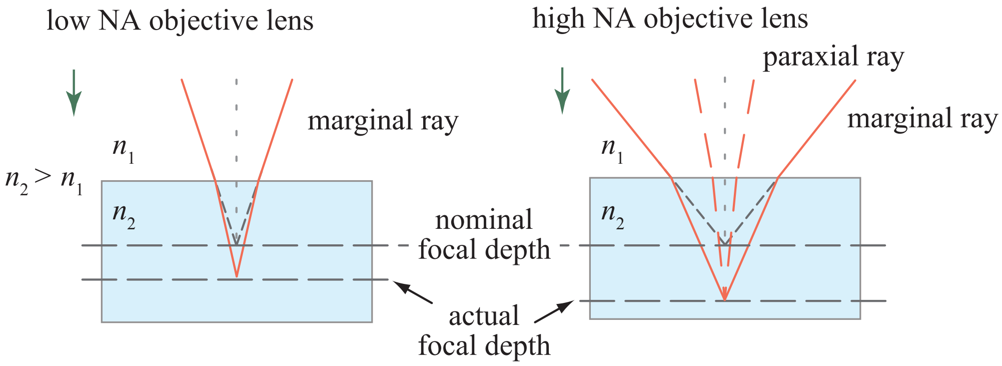

Figure 4.2: Effect of numerical aperture on aberrations. Marginal rays focussed by a high NA lens propagate a longer path through a specimen than in the case of a low NA lens, and are consequently affected more by specimen-induced aberrations.

As light is focussed by an objective lens, the rays refract on entering the specimen due to the changes in refractive indices. As a result, some form of refocussing of the light occurs, which is proportional to the portion of the focussing cone entering the specimen medium [29, 30, 31]. This causes an artificial scaling of the image in the axial direction. For example, on entering a medium of higher refractive index, the actual focal position (AFP) lies deeper than the nominal focal position (NFP), as illustrated in Fig. 4.2. The difference between the NFP and AFP increases as the NA of the lens increases. Conversely, the axial shift is decreased if the specimen medium has a smaller refractive index. The AFP is almost linearly proportional to the NFP [31, 32].

For high NA lenses, axial resolution and image brightness are known to reduce with increasing depth [29, 33, 30], and aberrations also increase. Although the immersion medium used between the lens and the coverslip reduces spherical aberrations, the varying refractive index within the specimen introduces other aberrations. Also, a high NA lens focusses light over greater angles compared to a low NA lens, as explained above. The marginal rays from a high NA lens traverse a longer optical path compared to its paraxial rays (located alongside the optical axis), and are therefore affected more by aberrations than the paraxial rays. Thus, images using high NA objectives are affected more by aberrations.

4.3 Representation of Aberrations

The wavefront phase Φ [Sec. 4.1] can be assumed to be represented by the expansion of an infinite sum of weighted orthogonal functions [34, 35]. Due to the circular apertures involved in most optical systems, a complete set of polynomials is required that is orthogonal over the interior of a circle [22]. Some such series include Zernike [22, 36] and Lukosz [8]. 2D Legendre polynomials [37] are used when square apertures are of interest.

The Zernike circle polynomials are often used in optics as they form an orthogonal set of functions defined over a unit circle and have simple properties of invariance [22]. Low-order Zernike polynomials correspond to simple shapes that can be reproduced accurately in AO systems [34], and they represent aberrations such as astigmatism, coma and spherical aberration that are commonly encountered in most optics systems and ophthalmology. Zernike polynomials can be defined in polar coordinates so that they are a product of angular basis functions of azimuthal frequency m and radial polynomials of degree n, and are defined as [38]:

$$Z_n^m(\rho,\theta) = \begin{cases} \sqrt{2(n+1)}R_n^{-m}(r)\sin(-m\theta), & m < 0, \\ \sqrt{n+1}R_n^0(\rho), & m = 0, \\ \sqrt{2(n+1)}R_n^m\cos(m\theta), & m > 0, \end{cases} \tag{4.3}$$

where ρ is the normalised radial coordinate, $m \leq n$ and $n - |m|$ is even. Eq. (4.3) defines a set of orthonormal Zernike polynomials that has been normalised so that each polynomial has a root mean square (RMS) value of one radian over the unit circle, and for $n \neq 0$, the mean is zero and variance is π radians [38, 36]. For $n = 0$, Z_0^0 or piston has a mean of one radian and variance of zero. The radial polynomials R_n^m are defined as:

$$R_n^m(\rho) = \sum_{s=0}^{\frac{n-|m|}{2}} \frac{(-1)^s (n-s)!}{s! \left(\frac{n+m}{2} - s\right)! \left(\frac{n-m}{2} - s\right)!} \rho^{n-2s}. \tag{4.4}$$

For convenience of ordering, the Zernike polynomials can be identified with a single index k [39] that is a function of n and m. The indexing scheme used here assigns positive value of m to cosine terms and negative value of m to sine terms [38]. The first fifteen Zernike polynomials are defined in Tab. 4.1. Z_1 or piston is not considered an aberration since it shifts the entire wavefront by a constant phase.

k	n	m	$Z_k(\rho,\theta)$ or $Z_n^m(\rho,\theta)$	Term
1	0	0	1	piston
2	1	1	$2\rho\cos\theta$	tip
3	1	-1	$2\rho\sin\theta$	tilt
4	2	0	$\sqrt{3}(-1+2\rho^2)$	defocus
5	2	2	$\sqrt{6}\rho^2\cos 2\theta$	astigmatism
6	2	-2	$\sqrt{6}\rho^2\sin 2\theta$	astigmatism
7	3	1	$2\sqrt{2}(-2\rho+3\rho^3)\cos\theta$	coma
8	3	-1	$2\sqrt{2}(-2\rho+3\rho^3)\sin\theta$	coma
9	3	3	$2\sqrt{2}\rho^3\cos 3\theta$	trefoil
10	3	-3	$2\sqrt{2}\rho^3\sin 3\theta$	trefoil
11	4	0	$\sqrt{5}(6\rho^4-6\rho^2+1)$	primary spherical
12	4	2	$\sqrt{10}(4\rho^4-3\rho^2)\cos 2\theta$	secondary astigmatism
13	4	-2	$\sqrt{10}(4\rho^4-3\rho^2)\sin 2\theta$	secondary astigmatism
14	4	4	$\sqrt{10}\rho^4\cos 4\theta$	quadrafoil
15	4	-4	$\sqrt{10}\rho^4\sin 4\theta$	quadrafoil

Table 4.1: Definitions of the first 15 Zernike polynomials with names of the modes.

The phase Φ of an aberrated wavefront can therefore be expressed as the weighted sum of Zernike polynomials as:

$$\Phi(\rho,\theta) = \sum_{k=1}^{\infty} c_k Z_k(\rho,\theta), \tag{4.5}$$

where c_k is the modal coefficient corresponding to the aberration given by the Zernike mode k.

The Zernike aberrations are made up of one or more classical aberrations indicated by the radial polynomials. The classical aberration of the highest degree is optimally balanced with classical aberrations of equal or lower degrees so that variance across the pupil is minimised [39]. Looking up Z_{11} in Tab. 4.1, for example, the primary spherical aberration consists of the classical primary spherical aberration ρ^4 optimally balanced with defocus ρ^2. The piston term ensures that the mean over the unit circle is zero. Similarly, all the other Zernike polynomials are optimally balanced.

The radial polynomials in Eq.(4.4), and consequently the Zernike polynomials defined in Eq. (4.3), can be classified as even functions when n or m are even, and odd functions when n or m are odd, on the basis of their symmetry. Accordingly, system aberrations can be expressed as the sum of even and odd Zernike modes as:

$$\Phi = \Phi_e + \Phi_o, \tag{4.6}$$

where Φ_e and Φ_o are the sum of the even and odd polynomials, respectively. Fig. 4.3 illustrates the shape of the aberration functions given by the first fifteen Zernike polynomials where each row separates the even and odd polynomials — modes 1 and 4 – 6 are even, and modes 2 – 3 and 7 – 10 are odd.

The orthogonality relationship of the polynomials is given by [38]:

$$\frac{1}{\pi}\int_0^1 \int_0^{2\pi} Z_k(\rho,\theta) Z_{k'}(\rho,\theta)\,\mathrm{d}\theta\,\mathrm{d}\rho = \delta_{kk'}, \tag{4.7}$$

where $\delta_{kk'}$ is the Kronecker delta function defined as:

$$\delta_{kk'} = \begin{cases} 1, & k = k', \\ 0, & k \neq k'. \end{cases} \tag{4.8}$$

The coefficients c_k of the expansion terms in an aberration function Φ represent the

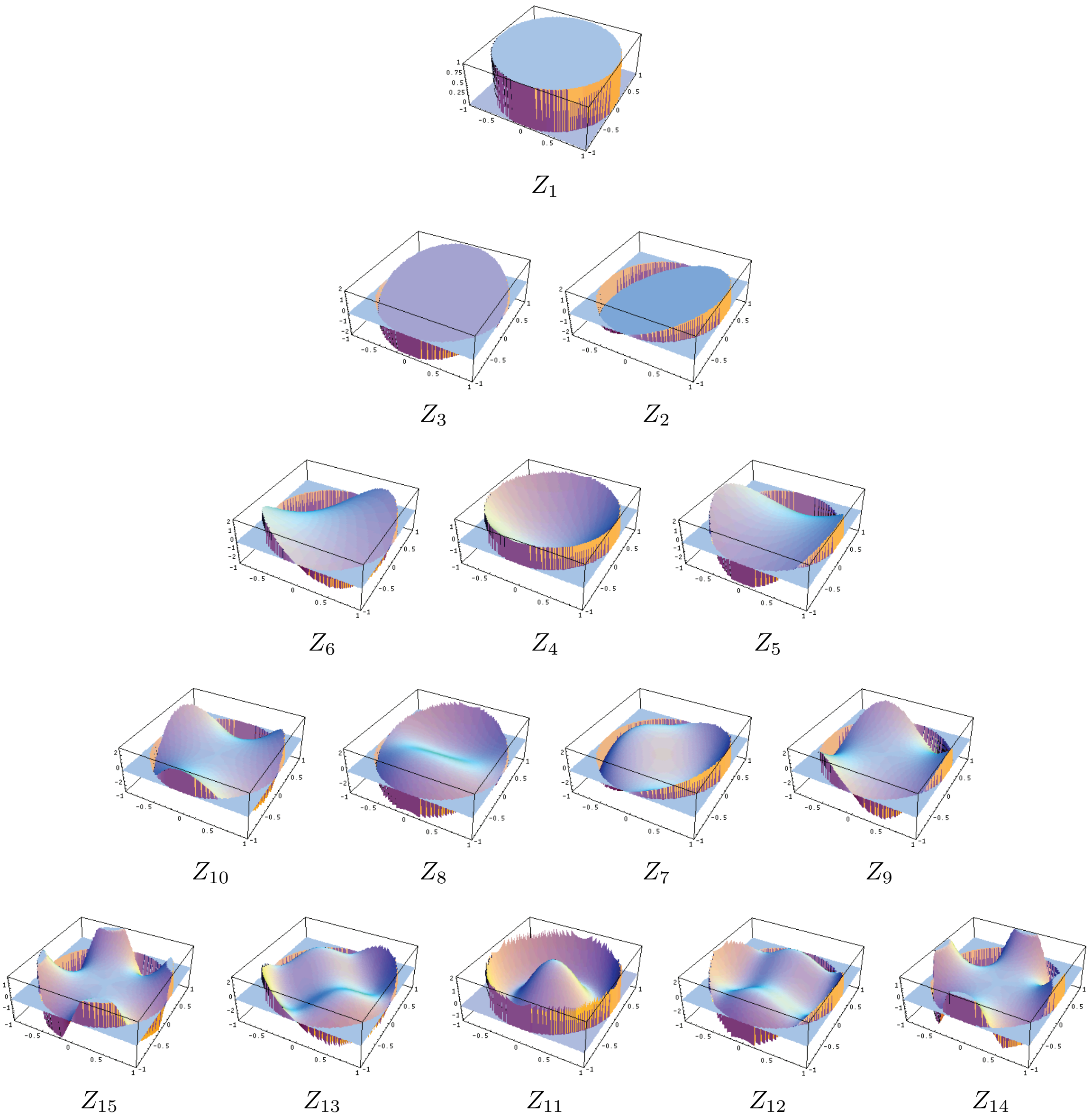

Z_1

Z_3 Z_2

Z_6 Z_4 Z_5

Z_{10} Z_8 Z_7 Z_9

Z_{15} Z_{13} Z_{11} Z_{12} Z_{14}

Figure 4.3: Shape of the first 15 Zernike polynomials.

standard deviations of the constituent Zernike polynomials Z_k. The orthogonality of the polynomials implies that the variance σ^2 of the expansion given by Eq. (4.5) is:

$$\sigma^2 = \sum_{k=2}^{\infty} c_k^2, \tag{4.9}$$

where σ is the standard deviation of the expansion.

4.4 Conclusions

This chapter discussed the sources of phase aberrations in microscopy and the effects of the NA of objective lenses. The mathematical representation of phase aberrations as an orthonormal series of Zernike polynomials was presented, which will serve as an essential tool to model the detection of aberrations from backscattered light in the dual-pass optical system. These models are used extensively in the following chapters to discuss the effects of filtering on phase aberrations by pinholes of various sizes, how non-uniform backscattering of light from specimens affect the phase changes of specimen-induced aberrations, and the estimation of aberrations by a SHWS as a series of Zernike polynomials.

Chapter 5

Adaptive Optics

Adaptive optics (AO) is used in microscopy to detect and correct aberrations. Direct wavefront sensing has advantages over indirect techniques since it requires shorter exposures. A Shack-Hartmann wavefront sensor (SHWS) can perform direct wavefront sensing by measuring the phase of incident light, while a deformable mirror (DM) can alter the phase of incident light by applying a phase equal, but opposite in magnitude, to the phase aberrations, thereby correcting aberrations. The SHWS can also be used to align the optics of a system [40], which can otherwise contribute to system aberrations [Sec. 4.2].

5.1 Adaptive Optics of Scattering Specimens

The effect of dual-pass imaging has been extensively studied in the field of ophthalmology. It has been shown theoretically and empirically that the asymmetric light distribution in the first pass is forced to be even-symmetric after the second pass as a result of odd aberrations, resulting in the loss of phase information [41]. However, odd aberration phase information was preserved using unequal entrance and pupil sizes [42, 43]. Simulations of the human eye have revealed that the phase information retained in a dual-pass system also depends on the scattering of light due to specimen structure [11].

Complex wavefront corrections have recently been demonstrated in deep tissue imaging using the concept of optical coherence microscopy in a dual-pass system [44]. Coherence gating and confocal detection using a pinhole were combined to achieve confinement of backscattered light to a single scatterer within volume specimens, and parallel optimisation method was employed to iteratively determine the wavefront correction phase for an SLM. Fast convergence of the focal spot to near-diffraction limit was demonstrated after 3 iterations and greater penetration depth was achieved. A similar parallel optimisation compensation of aberrations was also applied to multiphoton microscopy and demonstrated for deep tissue imaging [45].

One method restored the focal spot scattered through a strongly scattering specimen by constructing wavefronts that invert the diffusion of light using a non-iterative algorithm [46, 47]. By fixing a target or multiple targets, the phase modulation introduced by an SLM using this technique was shown to form a single focus or multiple foci, respectively. Based on a similar technique, adaptive correction was performed in the imaging of thin slices of brain tissue using two-photon microscopy [48].

Direct wavefront sensing using a SHWS has been shown to correct aberrations of thick inhomogeneous specimens in the detection path of a selective plane illumination microscope (SPIM) [49]. Fluorescent beads were inserted into the specimens as point source references, similar to the concept of guide stars in astronomy. Use of guide stars in a AO loop has also been demonstrated in fluorescence wide-field microscopy [50, 51] and confocal fluorescence microscopy [52]. The fluorescent light from a bead was used by a SHWS to determine the single-pass aberrations.

A SHWS has also been implemented in closed-loop AO in a confocal microscope, where structures like centrosomes were labelled with fluorescent proteins and used as biological guide stars [53, 54]. A guide star searching algorithm was used to locate suitable reference sources within specimens from obtained confocal images.

The inherent nature of two-photon microscopy producing a localised point source inside samples, which is also attributed to the depth-discrimination property of the microscope, was used as a non-linear guide star to demonstrate adaptive correction using a SHWS of C. elegans and mouse brain [55]. A SHWS and DM have been used to perform closed-loop AO of scattering tissue in a two-photon microscope by using a confocal pinhole for depth discrimination [56].

Direct wavefront sensing with backscattered light using a SHWS has not yet been done in microscopy. The following sections cover the theory of the SHWS and DM, which are prerequisites to set up such a AO system.

5.2 Shack-Hartmann Wavefront Sensor

Direct wavefront sensing relies on instruments to measure wavefront aberrations in real-time. Various modal wavefront sensors exist that directly output the aberrations as combinations of aberration modes, such as, Zernike polynomials. One of these sensors include the Shack-Hartmann wavefront sensor [3, 15] that is widely used in astronomy, and has recently been demonstrated in many microscopy applications. Modifications of the SHWS include the adaptive SHWS [57]. A WS based on reflective liquid crystal on silicon (LCOS) [58] has recently been demonstrated, which works similarly to the principle of the SHWS. A hierarchical wavefront sensor [59] uses several sensors for different spatial frequencies, and has been demonstrated for a SHWS. Various holography-based wavefront sensors [60, 61, 62, 63] have also been proposed in the last few years. The pyramid wavefront sensor [64] has been widely used, which uses a pyramidal prism to work out the phase gradient of wavefronts. Since a SHWS has been used in the experiments reported later, it is discussed herein.

Fig. 5.1 shows the schematic of a SHWS. It consists of an array of lenslets (small lenses), called a microlens array, mounted in front of a charge-coupled device (CCD) camera. The CCD camera is positioned in the focal plane of the lenslets. Light incident on the microlens array is focussed by the lenslets to form the Hartmann spot pattern that is detected by the CCD camera. When a plane wavefront impinges on a lens normally, it is focussed to a spot in the focal plane and on the optical axis. Accordingly, when a plane

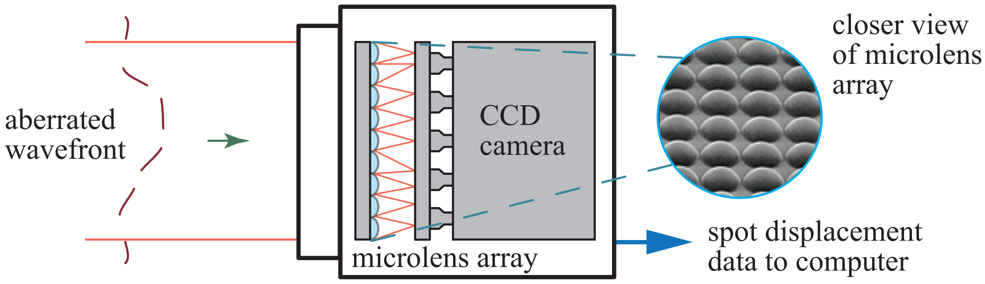

Figure 5.1: Schematic of a Shack-Hartmann wavefront sensor. A microlens array is mounted on a charge-coupled device camera. Light incident on the microlens array is focussed to a spot pattern and picked up by the camera. Deviation of the spots is used to estimate the phase of wavefronts.

wavefront is incident normally on the microlens array, light illuminating each lenslet is focussed on the optical axis in the focal plane of the lenslet and onto the CCD camera. This position is referred to as the reference spot position. The Hartmann spot pattern thus obtained from aberration-free light is called the reference spotfield, which is shown in Fig. 5.2a. The confines of each spot on the CCD camera due to the aperture of a lenslet can be termed as the domain of the lenslet. The spots will therefore be centred in their domains in the reference spotfield.

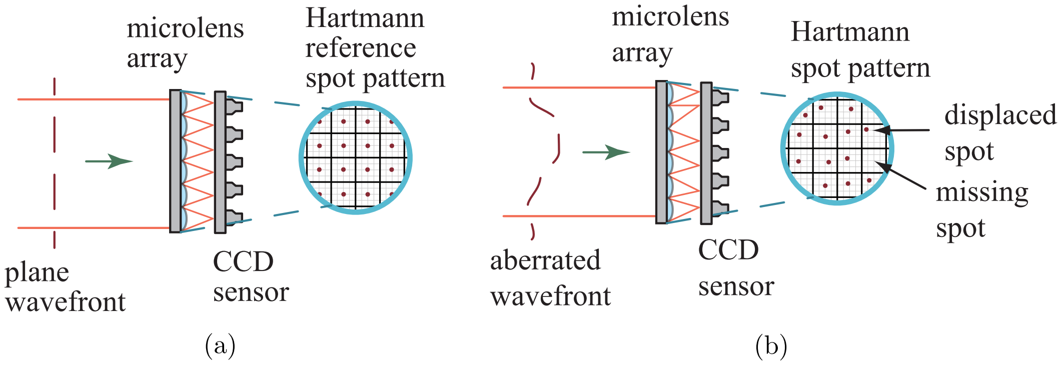

Figure 5.2: Hartmann spots. (a) Plane wavefront normally incident on the SHWS produces the reference spotfield. (b) Spots are displaced due to aberrations.

5.2.1 Centroiding

If it is assumed that the phase of an aberrated wavefront impinging on the microlens array does not vary too rapidly, then the wavefront across each sub-aperture can be approximated to be flat, but tilted. Hence, the focal spots will be shifted from the centre of their domains on the CCD camera. In practice, this is the average of the tilt over each sub-aperture. Therefore, an inherent instrumental error exists in the system. An aberrated spotfield is illustrated in Fig. 5.2b. The centre of the displaced spots need to be located to estimate the aberrations of the wavefront. Centroiding is one such method.

For more rapid phase variations, the approximation of tip/tilt across the sub-aperture will not hold. Under such circumstances, the spot will be shifted and severely aberrated. If the aberration is very complex across the sub-aperture, then the spot may, in effect, not be visible. Special algorithms are required for aberration measurements to cope with such anomalies. In the simplest case, provided that the incident wavefront is not affected by severe aberrations, the position of maximum intensity of a spot on the Hartmann pattern coincides with the centroid of the spot in a sub-aperture.

To locate the centroid, the lateral positions of a spot in the x and y directions, respectively, can be determined by the first moments, or centre of gravity (CoG) method, as:

$$\begin{aligned} S^x = \bar{x} &= \frac{1}{I_t} \int\limits_y \int\limits_x x I(x,y) \, \mathrm{d}x \, \mathrm{d}y, \\ S^y = \bar{y} &= \frac{1}{I_t} \int\limits_y \int\limits_x y I(x,y) \, \mathrm{d}x \, \mathrm{d}y, \end{aligned} \tag{5.1}$$

where I_t is the total intensity over the sub-aperture given by:

$$I_t = \int\limits_y \int\limits_x I(x,y) \, \mathrm{d}x \, \mathrm{d}y. \tag{5.2}$$

Eq. (5.1) is computationally very fast [65, 66] and produces measurements with very low error and high repeatability [67]. The weight of the centroid can be shifted by background noise, therefore yielding wrong lateral positions of the spot. However, this is easily rectified by applying a threshold to reduce the background to zero, given the signal-to-noise ratio (SNR) is significantly high [18]. Statistically, the error is low when background noise is uniform and the number of pixels under observation is large [65].

There are a few variations to the first moments or CoG method, such as, weighted centre of gravity (WCoG), iteratively weighted centre of gravity (IWCoG) and intensity weighted centroiding (IWC) [65, 66]. The WCoG takes into account that a spot has a Gaussian spread and accordingly weights the intensity function with a Gaussian distribution. IWCoG improves on the errors caused in CoG and WCoG due to noise by iteratively correcting the position of the Gaussian centre and it also gives more accurate measurements for large spot shifts [68, 65, 66]. However, IWCoG is computationally more intense. IWC uses a weighted function that is intensity dependent, and it performs better under low light conditions.

Cross-correlation between a given sub-aperture and all remaining sub-apertures can be performed to determine the local displacement of each of the spots [68]. Correlation based techniques are more robust than the aforementioned centroiding methods as correlation is insensitive to the errors due to background light and noise. Correlation provides better results in the presence of large aberrations that lead to spots exhibiting elongation, smearing or secondary peaks [69]. Matched filtering is a technique similar to correlation where the peak from a convolution in the spatial domain is used to determine the local gradient in each sub-aperture [68]. However, these methods are very complex and require intense computation.

The aforementioned centroiding methods have been investigated thoroughly in many literatures [68, 65, 66, 70]. Some of these methods provide better centroid measurements compared to the CoG method, particularly in situations involving large aberrations, speckle, noise and low SNR. However, Eq. (5.1) can be solved much faster and is sufficient for systems with high SNR and small aberrations, such as those investigated in this report.

5.2.2 Wavefront Reconstruction

The method for the reconstruction of a wavefront from slope measurements can be distinguished as either zonal or modal. Zonal estimation refers to those methods where integration of local slopes is performed to create a discrete phase field with minimum difference with respect to the measured slopes [37]. Modal estimation approximates the wavefront by fitting known aperture functions [37], such as Zernike polynomials [Sec. 4.3]. Modal estimation is superior to zonal estimation in terms of error propagation, particularly when a fixed number of modes are of interest, and the former is computationally easier and faster [37]. Consequently, modal estimation was used for the experiments reported herein, and a description of the reconstruction method follows.

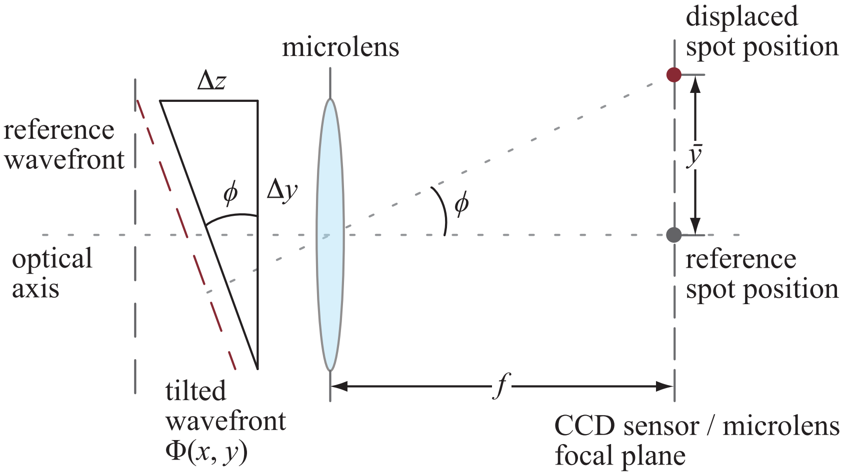

Figure 5.3: Hartmann spot displacement is directly proportional to the gradient of the wavefront phase.

Using Fig. 5.3, a local wavefront incident on a lenslet at an average angle of ϕ will produce a focal spot in the focal plane displaced by a distance of $\bar{y}$ from the optical axis and making an angle ϕ with the optical axis. If the wavefront is given by the phase function $\Phi(x, y)$, then the gradient of the wavefront with respect to a plane wavefront incident normally on the lenslet is:

$$\frac{\delta}{\delta y}\Phi(x, y) = \tan\phi = \frac{\bar{y}}{f}. \tag{5.3}$$

Hence, the displacements $\bar{x}$ and $\bar{y}$ of the spot centroid in any sub-aperture can be shown to be dependent on the gradient of the wavefront phase:

$$\begin{aligned}\bar{x} &= f\frac{\delta\Phi}{\delta x},\\ \bar{y} &= f\frac{\delta\Phi}{\delta y}.\end{aligned} \tag{5.4}$$

The wavefront can be estimated from the wavefront slope measurements [37] and modelled using the Zernike polynomials. Using Eq. (4.5), the slope measurements given by Eq. (5.4) can be expressed using Zernike polynomials as:

$$\begin{aligned}S^{x}_{i,j} &= \sum_{k=2}^{M} c_k \frac{\delta}{\delta x} Z_k(x,y)_{i,j},\\ S^{y}_{i,j} &= \sum_{k=2}^{M} c_k \frac{\delta}{\delta y} Z_k(x,y)_{i,j},\end{aligned} \tag{5.5}$$

where the indices i and j denote the appropriate sub-apertures of the microlens array with N lenslets, and M is the highest mode of Zernike polynomial used for wavefront estimation. The summation starts from $k = 2$ to exclude piston, which has a zero gradient. $\mathbf{S}^x$ and $\mathbf{S}^y$ can be defined as the vectors comprising of all the displacements in the x and y directions, respectively. From Eq. (5.5), it can hence be derived that:

$$\mathbf{S} = \mathbf{Dc} + \mathbf{n}, \tag{5.6}$$

where $\mathbf{S}$ is a concatenated vector of $\mathbf{S}^x$ and $\mathbf{S}^y$, $\mathbf{D}$ is a concatenated matrix containing all partial derivatives of $Z_k(x, y)$ with respect to x and y, and the vector $\mathbf{c}$ contains the $M - 1$ phase coefficients c_k. In reality, the slope measurements consist of the local tilt $\mathbf{Dc}$ and noise $\mathbf{n}$. This noise arises due to instrumental error and background noise [Sec. 5.2.1]. Since the system is overdetermined (having more equations than unknowns), an approximate solution for $\mathbf{c}$ can be found by minimising the norm:

$$\min_{\mathbf{c}} \|\mathbf{Dc} - \mathbf{S}\|, \tag{5.7}$$

which is called the least-squares solution $\hat{\mathbf{c}}$. Although piston is excluded, minimum norm is assured since all the Zernike polynomials have zero mean. Assuming the matrix $\mathbf{D}$ has full column rank (all the equations are linearly independent), the least-squares solution is calculated by the pseudo-inverse of the $2N \times (M-1)$ matrix $\mathbf{D}$ as given by:

$$\hat{\mathbf{c}} = [(\mathbf{D}^{\mathrm{T}}\mathbf{D})^{-1}\mathbf{D}^{\mathrm{T}}]\mathbf{S}, \tag{5.8}$$

where $\mathbf{D}^{\mathrm{T}}$ is the transpose of the matrix $\mathbf{D}$. Having obtained a set of coefficients c_k based on the slope measurements, the wavefront incident on the SHWS can be reconstructed as the weighted sum of the Zernike polynomials as given by Eq. (4.5). The elements of the matrix $(\mathbf{D}^{\mathrm{T}}\mathbf{D})^{-1}\mathbf{D}^{\mathrm{T}}$ can be predetermined as they depend only on the sensor geometry. Furthermore, the matrix $\mathbf{D}^{\mathrm{T}}\mathbf{D}$, and thus its inverse, are sparse. These factors lead to fast computation of aberration modes.

While the Zernike circle polynomials are orthogonal over the unit circle, their derivatives are not. For Zernike polynomials up to mode 6, $\mathbf{D}^{\mathrm{T}}\mathbf{D}$ is diagonal. However, on increasing the number of polynomials, the matrix is no longer diagonal. This results in a phenomenon called aberration cross coupling [34, 71]. The matrix is still sparse and yields fast computation. But the coupled modes with off-diagonal elements are estimated as the weighted sums of those modes. Estimation error due to cross coupling can be reduced by reducing the number of Zernike modes [34], but at the cost of increasing modelling error [71]. Another solution to cross coupling would be to use a set of polynomials whose derivatives are orthogonal [34, 71].

In practise, the columns of the matrix $\mathbf{D}$ are not always linearly independent. This results in the higher-order aberrations being estimated as linear combinations of lower-order aberrations. This effect is known as aberration aliasing. The higher-order aberration modes affected depends on the total modes used and the Hartmann spot configuration [71]. It is therefore recommended to limit the number of Zernike polynomials used to prevent aliasing.

Although Eq. (5.8) can be used under ideal circumstances, software for wavefront sensing generally include advanced algorithms to tackle anomalies, such as missing spots and low brightness, to mention a few. Information on the precision and accuracy of the SHWS can be found in [67].

5.3 Deformable Mirror

The phase information retrieved by a WS can be used by a suitable adaptive element to correct aberrations of the incident light [3, 16]. These adaptive elements include a variety of SLMs and DMs. The choice of hardware depends on the application — response time of the hardware, maximum aberration that can be compensated, hysteresis, etc.

A liquid crystal SLM (LCSLM), filled with either ferroelectric liquid crystal (FLC) or nematic liquid crystal (NLC), can modulate light in amplitude and phase. An LCSLM achieves modulation using the polarisation effects of liquid crystals. Consequently, phase modulation is restricted to 2π or one wavelength. These devices can operate in the kilohertz range.

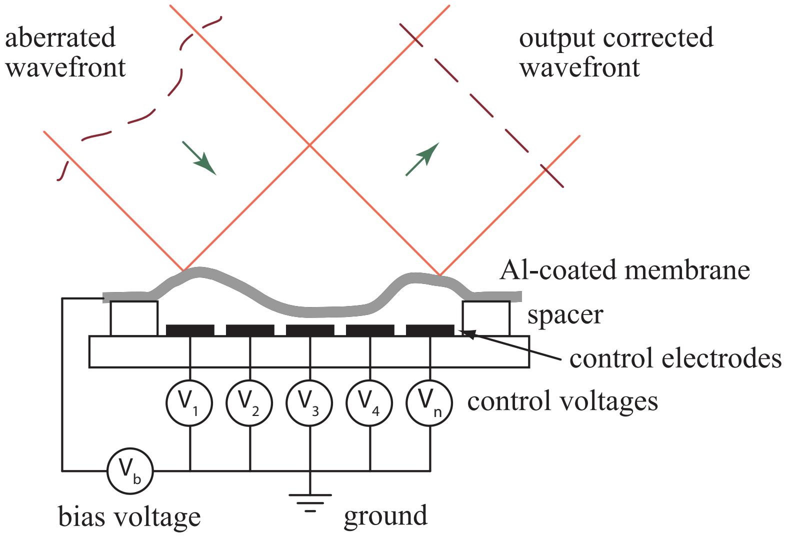

Figure 5.4: Schematic of a deformable mirror. Voltages in the electrodes modulate the shape of the membrane and thereby alter the phase of incident wavefronts. The mirror introduces a phase of equal, but opposite, magnitude to perform phase conjugation.

A DM consists of a flexible mirror surface that can be deformed in order to modulate the phase of light. Fig. 5.4 shows the schematic of one such DM called the micro-machined membrane deformable mirror, which consists of a flexible membrane suspended above an array of electrodes. The membrane is made from silicon nitride, for example, for the 37 actuator OKO DM used in the experiments described later in this report. The membrane is coated with aluminium for the reflective surface. Applying voltages to the electrodes creates potential differences between the electrodes and the mirror surface, resulting in electrostatic forces that change the shape of the mirror [72]. Since the membrane is clamped at the edge, typically the pupil is reduced to two-thirds of the diameter of the membrane DM to allow correction of aberrations at the edge of the pupil [73].

A slight variation to the micro-machined membrane DM is the microelectromechanical systems (MEMS) DM [74]. The MEMS DM contains actuators based on MEMS technology, and consequently, a DM can have thousands of actuators. Such a DM provides very fast and precise actuation and is well suited for real-time AO systems.

A piezoelectric DM [75] consists of a reflective quartz plate with free edge to avoid the problem of modulating phase at the edge suffered by the membrane DM. The plate is suspended on piezoelectric actuators that shape the mirror. The features of a piezoelectric DM attribute to its higher actuator stroke (the maximum distance displaced by an actuator) and sharper influence function (the mirror response to the stimulation of a single actuator). Subsequently, it can produce higher phase changes compared to a membrane DM. However, the hysteresis of such a DM has been found to be higher [75].

A bimorph mirror [75] is made from two active layers with electrodes built into the material. The layers are separated by a ground electrode. Deformation occurs on application of voltages to the electrodes. A bimorph mirror has actuator stroke similar to a piezoelectric DM, but suffers from a much smaller hysteresis [75].

There are several parameters that govern the choice of DM. Number of actuators, actuator pitch (distance between neighbouring actuators) and actuator stroke determine the maximum wavefront gradients and maximum phase that can be compensated in a AO system. Influence function and actuator coupling (displacement of neighbouring actuators) will determine the accuracy of wavefront phase reconstruction. Hysteresis and response time are crucial in determining if the DM is suitable for fast, real-time adaptive correction in a closed-loop set-up. Since a membrane DM was used in the experiments discussed later in this report, the following section briefly explains the mirror characterisation techniques of such a mirror.

5.3.1 Mirror Characterisation

If a wavefront of phase profile Φ is incident on the SHWS, the SHWS estimates the phase as a function Ψ that is given by Eq. (4.5) as a sum of Zernike polynomials. Ideally, a DM introduces a phase that is equal, but opposite in magnitude, to the estimated phase in order to compensate the aberrations. Consequently, a plane wavefront is formed after reflection off the DM. This form of adaptive correction is called phase conjugation, which is illustrated in Fig. 5.4. Phase conjugation is applied to any adaptive element in a AO system to compensate for aberrations. In reality, however, due to the various parameters discussed in the previous section, a DM cannot perfectly recreate the given phase profile. This results in a phase modulation of $\tilde{\Psi}$ by a DM, given by:

$$\tilde{\Psi} \approx -\Psi = -\sum_{k} c_k Z_k. \tag{5.9}$$

In the membrane DM, to allow movement of the mirror surface both toward and away from the electrodes, a constant offset voltage is usually applied to all electrodes, and the curvature of the resultant mirror surface is compensated by illuminating the surface with a suitably divergent beam. The mean deflection of the surface in the vicinity of an electrode is found to be proportional to the square of the applied voltage [76]. Therefore, control signals proportional to the square root of the electrode voltage are used to modulate the mirror membrane. The DM typically tends to have an initial aberration of astigmatism due to deformation of the membrane caused by residual stresses in the substrate that must be removed before the DM can be used properly [76].

One method for training the control system for a membrane DM is by utilising a wavefront generator [76]. An iterative procedure based on a modal wavefront sensor [38] is used to measure the input wavefront aberrations and thereby work out the DM control matrix. However, one drawback to this system is that it requires a calibrated wavefront generator.

The set of DM control signals that allow the generation of Zernike modes can also be obtained using interferometric methods [76, 75]. One such method performs fringe analysis and phase unwrapping in an interferometer to measure the phase of wavefronts generated by a membrane DM [76]. Pseudo-inversion of the control matrix by singular value decomposition (SVD) permits additional control of the DM. By changing the amount of singular values, the modes likely to saturate the DM can be removed [76, 75].

There are other methods that rely on a WS to evaluate the DM modulation in order to work out the control matrix. However, mirror characterisation based on interferometric methods are often chosen as they can be set up readily using standard optics. Additionally, they provide more control over the membrane DM control matrix. Corrections based on low order Zernike modes have already been shown to provide significant imaging improvements in optical microscopes, although diffraction-limit may not be restored [12], and correction up to third order spherical aberration has been shown to essentially restore diffraction limit [1].

5.4 Conclusions

A brief review of various works on AO systems for scattering specimens has been presented in order to shed light on the importance of this project. While the SHWS has been used in conjunction with targets or guide stars in various researches, direct wavefront sensing using information from backscattered light has yet to be tried in microscopy. This chapter therefore discussed the working principles of the SHWS, various centroiding algorithms and the wavefront reconstruction algorithm used to estimate phase aberrations based on the least-squares model. Various types of SLMs and DMs were discussed as they are an integral part of any AO system. Since a DM was used in the experiments, it was briefly discussed herein.

Chapter 6

Direct Wavefront Sensing using Backscattered Light

The aberrations in the illumination path need to be corrected to achieve a diffraction-limited focal spot. But in a dual-pass system, such as the confocal reflection microscope [Ch. 3], light passes through the same parts of the specimen in both the illumination and detection paths. Consequently, aberrations are also induced in both paths. A WS placed in the detection path may measure erroneous phase due to the dual-pass effect. Research in ophthalmology has already shown the ambiguity in aberration measurements in an ocular dual-pass system arising from the loss of phase information, particularly for the case of odd aberration modes. The odd aberration modes have been shown to cancel out [11, 41, 42].

It is difficult to induce controllable variable aberrations using an aberrating specimen. However, a DM can be used to simulate specimen-induced aberrations. To model the dual-pass nature, the DM should be positioned where it can induce aberrations in both paths. Backscattered light, after being aberrated by the DM, will be detected by the WS.

A practical system incorporating a SHWS was implemented in order to investigate the effects of using backscattered light as the source for wavefront sensing in a laser scanning microscope. In this chapter, the system is modelled for different specimens and configurations, and the nature of wavefront sensing is discussed.

6.1 Wavefront Sensing in Dual-Pass Imaging System

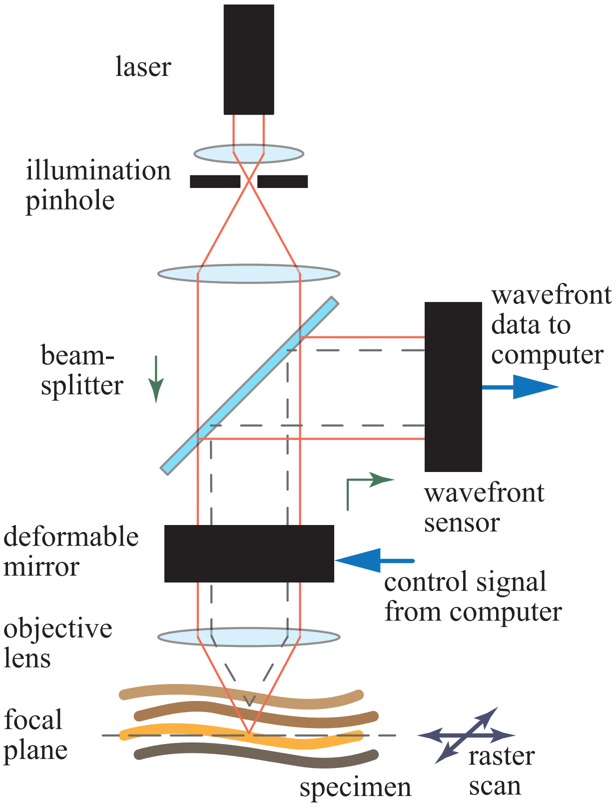

Figure 6.1: Wavefront sensing in dual-pass imaging system. Light passes through the DM and the specimen both in the illumination and detection paths, and is therefore aberrated in both paths.

Fig. 6.1 shows a possible set-up for wavefront sensing in a dual-pass adaptive microscope. In the illumination path, light extended from a laser source impinges on a DM, shown as a box in the diagram for simplicity. Light is modulated and reflected by the DM, and then focussed by an objective lens into a specimen. Light scattered back by the specimen is once again modulated and reflected by the DM, but in the detection path, and then finally picked up by a WS. The aberrations from different parts of the system and specimen can be modelled as part of the effective pupil function [Sec. 4.1], and therefore DM-induced aberrations can represent controllable specimen-induced aberrations.

6.1.1 Measuring Phase in Dual-Pass Imaging System

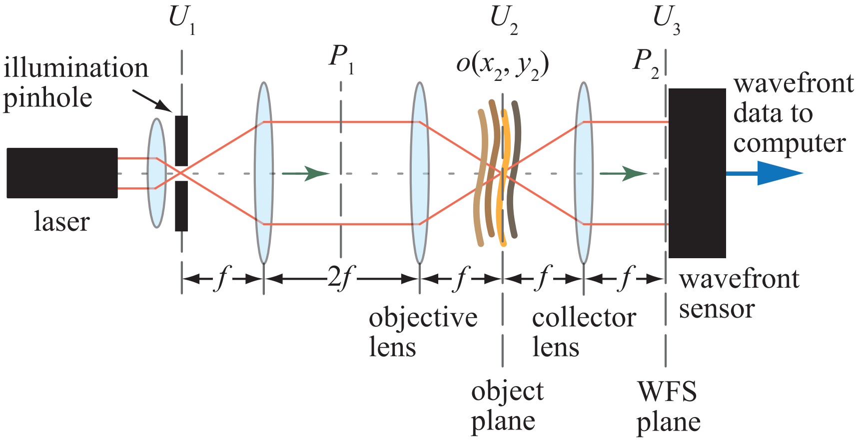

Figure 6.2: Optical arrangement of the dual-pass wavefront sensing system unfolded. The phase modulations of the DM are incorporated in the effective pupil functions P_1 and P_2.

The dual-pass wavefront sensing system can be unfolded using the $4f$ system [Sec. 2.7], as shown in Fig. 6.2. The effective pupil function P_1 represents the specimen-induced aberrations induced by the DM in the illumination path. Since the illumination path in the dual-pass wavefront sensing system is identical to that of the confocal reflection microscope in Fig. 3.1, the field after interaction with the specimen is given by Eq. (3.3):

$$U_2(x_2, y_2) = h_1(x_2, y_2)o(x_2 - x_s, y_2 - y_s). \tag{3.3}$$

The pupil image detected by the WS, given by the field at U_3, lies in the Fourier spectrum plane of the collector lens. Therefore, the field before the WS can be given by Eq. (2.46) as:

$$U_3(x_3, y_3) = \mathcal{F}\left\{h_1(x_2, y_2)o(x_2 - x_s, y_2 - y_s)\right\} P_2(x_3, y_3), \tag{6.1}$$

where P_2 is the pupil function in the detection path. Referring to Fig. 6.2, after converging into the specimen in the illumination path, the rays fall on opposite sides of the optical axis in the detection path. Since the objective and collector lenses are the same in the dual-pass set-up, P_2 is essentially the spatial inversion of P_1 and can be expressed as $\tilde{P}_1$, leading to:

$$P_2(x_3, y_3) = P_1(-x_1, -y_1) = \tilde{P}_1(x_3, y_3). \tag{6.2}$$

For simplicity, if the specimen is considered stationary by taking $x_s = 0$ and $y_s = 0$, then the spectrum of the specimen in the Fourier domain can be expressed as:

$$O(x_3, y_3) = \mathcal{F}\left\{o(x_2, y_2)\right\}. \tag{6.3}$$

Hence, the Fourier term in Eq. (6.1) can be identified as a convolution in the Fourier domain, and the pupil image before the WS can be written simply as:

$$U_3 = (P_1 \otimes O)\tilde{P}_1. \tag{6.4}$$

Hence, the wavefront phase Ψ measured by an ideal WS in a dual-pass system is given by:

$$\Psi = \arg\left\{U_3\right\} = \arg\left\{(P_1 \otimes O)\tilde{P}_1\right\}, \tag{6.5}$$

where the function arg{} gives the phase of the operand. Clearly, the presence of the Fourier spectrum of the specimen in Eq. (6.5) implies the dependence of aberration measurement on specimen structure.

6.2 Effects of Specimen Structure

The detection of aberrations can vary widely due to the structure of specimens. To illustrate the effects of specimen structure on detected phase measurements, specimens consisting of an aberrating medium were modelled. The effects on even and odd aberrations were considered separately [Sec. 4.3]. Half of an RMS radian of the even aberration astigmatism, Z_5, and the odd aberration coma, Z_7, were independently introduced into the effective pupil function of the theoretical model. The phase of the induced aberrations, in radians, along the diameter of the effective pupil at $\theta = 0°$ are shown in Fig. 6.3a — the peak-to-peak phase variations for astigmatism and coma being 1.22 and 2.83 radians, respectively.

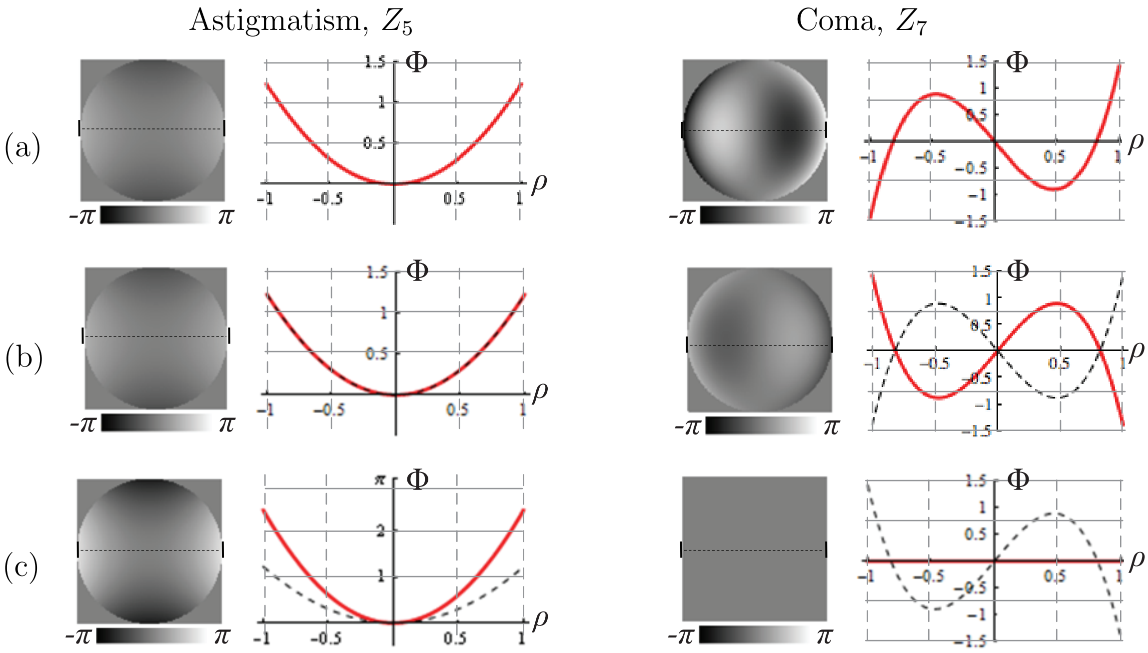
Astigmatism, Z_5

Coma, Z_7

Figure 6.3: Argument of WS pupil function in a dual-pass optical system showing the phase in the pupil plane (left) and its cross-section shown with the dotted lines (right). (a) Induced phase aberrations in the illumination path. Measured phase aberrations from (b) a point-like specimen and (c) a specular specimen. Dashed lines in the cross-sections show the induced aberrations shown in (a).

6.2.1 Point-like Specimen

A point-like object, which is smaller than the focal spot illuminating it, will scatter the energy from the incident light and re-emit aberration-free spherical wavefronts. The scattered light will be distorted again in the detection path, but the phase aberration will be inverted due to the spatial inversion of the pupil function in the detection path [Sec. 6.1.1]. Hence, the detected aberration Ψ is the same as the spatially-inverted specimen-induced aberration $\tilde{\Phi}$ in the detection path.

The reflectivity of a point-like object on the optical axis is given by the Dirac delta function of Eq. (2.24):

$$o(x_1, y_1) = \delta(x_1)\delta(y_1). \tag{2.24}$$

whose Fourier transform given by Eq. (6.3) is a constant. For simplicity, if the Fourier transform is considered to be 1, the field formed by a point-like object in the pupil plane of the WS is given by Eq. (6.4):

$$U_3 = (P_1 \otimes 1)\tilde{P}_1 = k\tilde{P}_1 = kP_2, \tag{6.6}$$

where k is a constant arising from the convolution. Using Eq. (6.5), the phase measurement of the aberration made by the WS from a point-like object can be verified as the aberration in the detection path:

$$\Psi = \arg\left\{k\tilde{P}_1\right\} = \arg\left\{\tilde{P}_1\right\} = \tilde{\Phi}. \tag{6.7}$$

Comparing Fig. 6.3a with Fig 6.3b, these findings can be verified via simulation since the maximum phase values are the same for induced and detected aberrations, and the odd aberration coma is detected as spatially-inverted.

6.2.2 Specular Specimen

A specular or mirror-like specimen will reflect all of the incident light. Hence, light will be aberrated in the illumination path by the phase aberration Φ, and then by the spatially-inverted aberration $\tilde{\Phi}$ in the detection path. The reflectivity of a specular specimen can be defined as 1. Using Eq. (6.3), the Fourier transform of the object is $\delta(x_3)\delta(y_3)$. Therefore, the pupil image detected by the WS is given by Eq. (6.4):

$$U_3 = (P_1 \otimes \delta)\tilde{P}_1 = P_1\tilde{P}_1. \tag{6.8}$$

Due to spatial inversion:

$$\begin{cases} \tilde{\Phi}_e = \Phi_e, \\ \tilde{\Phi}_o = -\Phi_o, \end{cases} \tag{6.9}$$

where, Φ_e, Φ_o, $\tilde{\Phi}_e$ and $\tilde{\Phi}_o$ represent the even and odd aberrations in the illumination and detection paths, respectively, defined in Eq. (4.6). Hence, the phase measured by the WS is given by Eq. (6.5) as:

$$\Psi = \arg\left\{P_1\tilde{P}_1\right\} = \Phi + \tilde{\Phi} = 2\Phi_e, \tag{6.10}$$

which shows that the WS measures twice the phase of the even aberrations, while odd components cancel out due to spatial inversion in a dual-pass imaging system. Comparing Fig. 6.3a with Fig 6.3c, the simulation results show that the maximum phase measurement for the even aberration astigmatism is around 2.44 radians, which is twice the amount induced as part of the effective pupil function P_1. Also, the measured phase is zero for the odd aberration coma. Indeed, all odd aberrations will remain undetected in a dual-pass imaging system if a specular specimen is being observed.

6.2.3 Random Scatterer

Most realistic specimens do not have the idealised point-like or planar structures considered above, but rather more complex structures. Any scattering specimen can be thought of as being composed of many point scatterers. In the extreme case, a plane fully packed with point scatterers will form a specular surface. Light is therefore scattered collectively from the points in the focal region of the imaging system. Each scatterer contributes its own wavefront, so the ensemble of scatterers creates a superposition of wavefronts before the WS. Since scattering is a coherent process, the superposition of wavefronts causes phase and amplitude variations, leading to ambiguous wavefront sensing.

To represent a general scattering specimen, a 1601 × 1601 square pixels array comprising of randomly scattered points was modelled. Each scattering point was modelled as a pixel of reflectivity 1, whilst the remainder of the array had reflectivity of 0. In accordance with the Nyquist-Shannon sampling theorem, any feature will appear as a point if its area is less than half the area covered by the Airy disc. Subsequently, the parameters in the simulation were chosen so that the aberration-free focal spot had a diameter of 13 pixels, thus covering an area of approximately 133 square pixels. The specimen structure

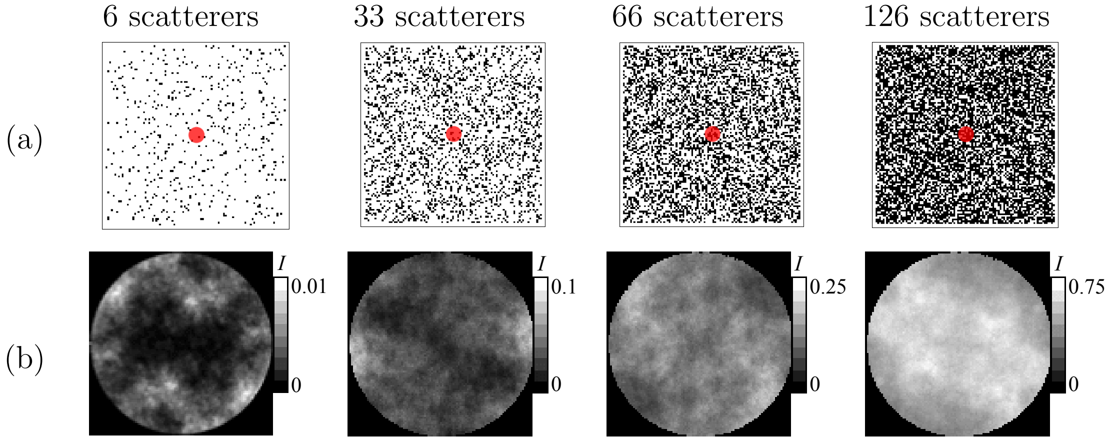

Figure 6.4: Sample specimens with varying point-like scatterer density. (a) 100×100 pixel samples shown with red spot illustrating relative size of the aberration-free focal spot. (b) Pupil intensity before the WS from the corresponding samples. I is the normalised intensity of light reflected by a specular surface. Image intensity became more uniform as the number of scatterers increased.

was changed by varying the percentage of scattering pixels between 1% and 99% of the array area, resulting in the change of the average number of point scatterers per unit area of the Airy disc. Fig. 6.4a shows 100 × 100 square pixel samples within some of the modelled specimens, while a red spot illustrates the relative size of the first zero of the aberration-free focal spot to the point scatterers. Fig. 6.4b illustrates the calculated intensity pattern in the pupil plane from a stationary focal spot probing the corresponding random scatterer sample. I is the normalised intensity of light reflected by a specular surface, given by Eq. (2.9). Very little light was scattered back from the sparse specimens. It can be seen that the maximum intensity with the specimen with 6 scatterers was only 1% of the light reflected by a specular surface. As the density of scatterers was increased, the pupil image before the WS became brighter and more uniform as expected.

Fig. 6.5 shows that as the number of scatterers probed by the focal spot increased, the superposition of light from multiple scatterers resulted in more uniform phase measurements. The non-uniform pupil intensity, shown in Fig. 6.4b, and accompanying phase variations from sparse specimens contributed to erroneous phase readings. Fig. 6.5a shows that with more than 33 scatterers probed by the focal spot, almost twice the induced even aberration phase was measured, similar to that expected for a specular specimen. It can be seen in Fig. 6.5b that with only 6 scatterers being probed by the focal spot, the mea-

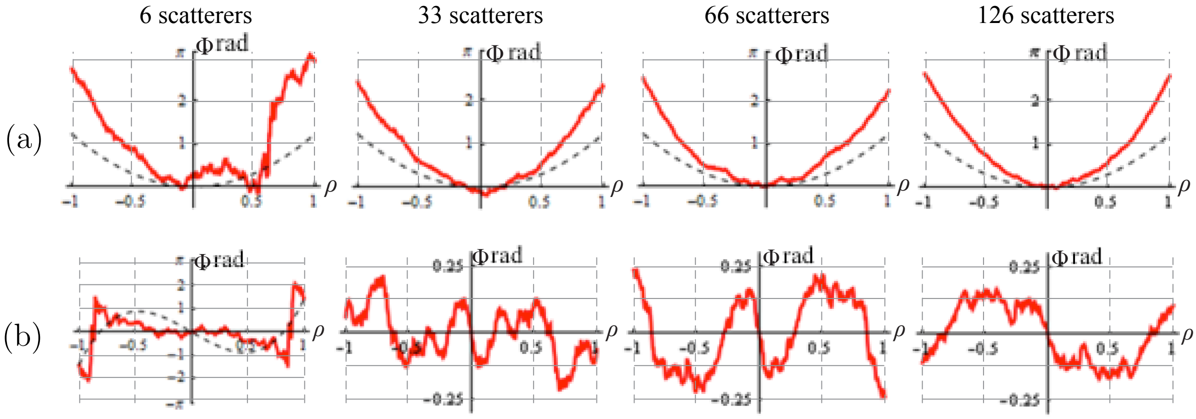

Figure 6.5: Argument of WS pupil function from variable density random scatterer samples. (a) Measured phase from even aberration astigmatism. (b) Measured phase from odd aberration coma. Where shown, the dashed lines show the induced aberrations of Fig. 6.3a. Phase measurements became more uniform as the number of scatterers increased.

surement is dominated by tilt and phase wrapping. As the number of scatterers increased, the phase profile resembled that of coma. Also, as specimen structure became more like a specular specimen, the maximum phase dropped to about 15% of the induced phase as the superposition of reflected light caused partial cancellation of odd aberrations. A slight decrease in the measured phase was also observed as the number of scatterers increased from 33 to 66, and then to 126.

6.3 Effect of Scanning in Wavefront Sensing

Clearly, the phase in the WS pupil relies largely on the specimen structure. Even for the same specimen, the measurements may vary depending on the position of the focal spot in the specimen. Amplitude variations in the pupil are problematic when performing direct wavefront sensing from backscattered light. A simple method to smooth these amplitude variations would be to average several measurements from neighbouring positions in the specimen. In practice, the exposure of the CCD camera of the SHWS can be set to a high value while scanning a specimen over a small region so as to capture an averaged image of the region in one exposure. Consequently, more light will be received by the sensor while making one measurement, and a smoother pupil image should be expected compared to the speckle patterns observed in Fig. 6.4b. An assumption is made that the specimen-induced aberrations are constant over the small region being scanned. The averaged complex-valued field $\bar{U}_3$ can be expressed mathematically as the integration of the field U_3, given by Eq. (6.1), over the the scanning coordinates (x_s, y_s) in the (x_3, y_3) plane as:

$$\bar{U}_3(x_3, y_3) = \int\limits_{y_s}\int\limits_{x_s} \mathcal{F}\left\{h_1(x_2, y_2) o(x_2 - x_s, y_2 - y_s)\right\} \tilde{P}_1(x_3, y_3)\, \mathrm{d}x_s\, \mathrm{d}y_s. \tag{6.11}$$

Since the reflectivity of the specimen is the only term in Eq. (6.11) dependent on the scanning coordinates (x_s, y_s), the integration can be brought within the Fourier transform. Hence, the scanned object reflectivity $o_s(x_2, y_2)$ can be defined as:

$$o_s(x_2, y_2) = \int\limits_{y_s}\int\limits_{x_s} o(x_2 - x_s, y_2 - y_s)\, \mathrm{d}x_s\, \mathrm{d}y_s. \tag{6.12}$$

Using Eq. (6.3), the Fourier spectrum of the scanned specimen can be introduced as $O_s(x_3, y_3)$. Hence, Eq. (6.11) can be simply written using the convolution operator as:

$$\bar{U}_3 = (P_1 \otimes O_s)\tilde{P}_1. \tag{6.13}$$

Due to the convolution with the Fourier spectrum of the scanned specimen, the exposure time of the CCD camera used for a measurement will depend largely on the specimen structure. For example, a sparse scattering specimen will need to be averaged over a longer exposure time so that a larger area is covered compared to a denser specimen. Accordingly, the function $o_s(x_2, y_2)$ in Eq. (6.12) will tend toward a constant as the scan area extends over an infinitely large area. Hence, Eq. (6.13) can be approximated as Eq. (6.8) for a specular object.

To investigate the scanning and averaging technique in simulation, a specimen with an average of 33 point scatterers per unit area of the Airy disc was used. Multiple images were taken from neighbouring positions in the specimen within a square array, and the array was enlarged to simulate increase of the size of the scanned area. The focal spot

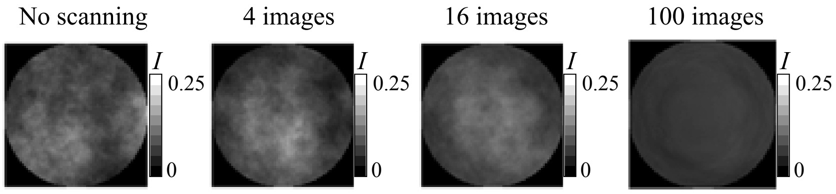

Figure 6.6: Averaged pupil intensity before the WS calculated by averaging the complex field from several measurements as the focus was scanned over a small area. I is the normalised intensity of light reflected by a specular surface. Pupil intensity became more uniform as the number of images averaged was increased.

was moved to the neighbouring scanning position within the scanned array by its radial length to fulfil the Nyquist-Shannon sampling theory and avoid aliasing, and the field U_3 was imaged. The images were then averaged to attain $\bar{U}_3$. Fig. 6.6 shows the pupil images as a consequence of averaging. As the area being scanned increases, the amplitude variations reduce, resulting in a smoother intensity distribution in the pupil plane.

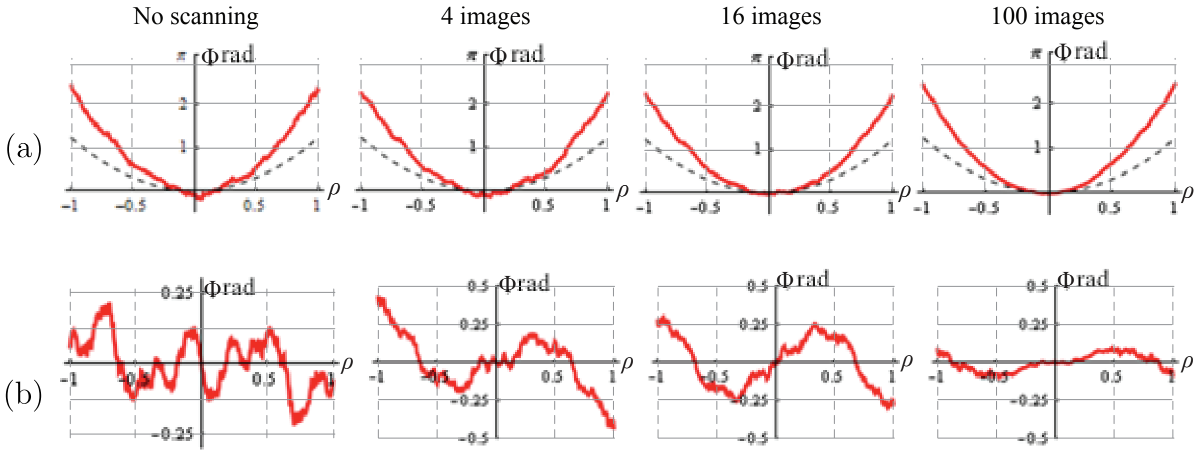

Figure 6.7: Argument of WS pupil function from a random scatterer sample being scanned and averaged over different areas. (a) Measured phase from even aberration astigmatism. (b) Measured phase from odd aberration coma. Where shown, the dashed lines show the induced aberrations of Fig. 6.3a. Phase measurements became more uniform as the number of images averaged was increased.

As Fig. 6.7 shows, the uniform averaged pupil intensity resulting from scanning caused a smoother phase distribution in the WS pupil. The measurements for even aberration in Fig. 6.7a show that nearly twice the induced even aberration is measured. However, as Fig. 6.7b shows, increasing the scanned area causes the phase measurement to decrease for the odd aberration. This is clearly due to the fact that over a larger area of integration, the specimen appears more and more specular, and that odd aberrations cancel out in a dual-pass set-up. The detected phase measurement is observed to lie between 10% to 15% of the induced odd aberration.

6.4 Axial Selectivity with a Wavefront Sensor Pinhole

The modelling in the previous section concerned only 2D specimens, whereas most realistic microscope specimens are 3D in nature. As Fig. 6.1 illustrates using the dashed rays, imaging a volume specimen will entail the reflection of light not only from the focal plane, but also from out-of-focus layers, which will contribute to erroneous aberration measurements. Hence, a method of out-of-focus rejection is required. This problem can be resolved using a pinhole to introduce axial selectivity. A pinhole effectively blocks light from out-of-focus planes, permitting only light from a region around the focus to pass through [Sec. 3.3]. When combined with the WS, this ability in turn prohibits light from out-of-focus regions affecting the actual aberration measurements. However, a very small pinhole, as would typically be used for high resolution confocal microscopy, cannot be used. It will filter out too much light, resulting in the failure to detect aberrations. Too large a pinhole will allow too much out-of-focus light, defeating the purpose of the WS pinhole. An appropriate compromise must therefore be found to carefully select the depth along the optical axis that can be allowed for wavefront sensing.

Fig. 5.3 showed that the displacement $\bar{y}$ of the focal spot away from the optical axis is directly proportional to the gradient of the wavefront phase. Accordingly, the direction of rays is dependent on the phase gradient where the rays pass the pupil. Therefore, if $\bar{y}$ is greater than the radius of the pinhole centred on the optical axis, then light focussed outside the pinhole aperture will be cut off. Clearly, the maximum allowable gradient of the phase is directly proportional to the radius of the pinhole. Therefore, the maximum phase gradient of the paraxial rays in the pupil that will allow the rays to pass through a pinhole of diameter d_p when focussed can be found using Eq. (5.3) as:

$$\left(\frac{\delta\Phi}{\delta x}\right)_{max} = \left(\frac{\delta\Phi}{\delta y}\right)_{max} = \frac{d_p}{2f}, \tag{6.14}$$

where $\frac{d_p}{2}$ replaces $\bar{y}$ to give the maximum allowable displacement of the rays.

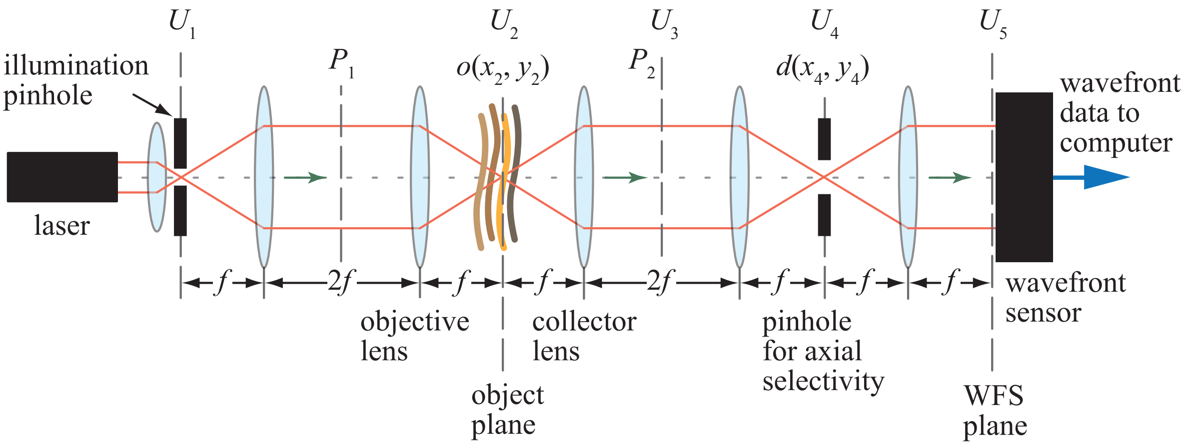

Figure 6.8: Optical arrangement of a dual-pass wavefront sensing system with a WS pinhole. Reflected light from the specimen is focussed through the WS pinhole and the filtered light is detected by the WS.

The dual-pass unfolded $4f$ arrangement of the wavefront sensing system in Fig. 6.2 can be extended to include a WS pinhole, as shown in Fig. 6.8. The pinhole acts as a mask of transmittance $d(x_4, y_4)$. The field $\bar{U}_3$ for the scanned and averaged pupil is given by Eq. (6.13). Consequently, the field after interaction with the pinhole can be written as:

$$\bar{U}_4 = \mathcal{F}\left\{(P_1 \otimes O_s)\tilde{P}_1\right\} d. \tag{6.15}$$

The field in the entrance pupil of the WS can therefore be found as:

$$\bar{U}_5 = \left[(P_1 \otimes O_s)\tilde{P}_1\right] \otimes \mathcal{F}\left\{d\right\}, \tag{6.16}$$

where the convolution operator $\otimes$ signifies that the pinhole acts as a smoothing mask besides performing out-of-focus rejection, which can be described as the local averaging of the pupil image $\bar{U}_3$. Using Eq. (6.11), the field $\bar{U}_5$ given by Eq. (6.16) can be expanded as:

$$\bar{U}_5(x_5,y_5) = \left[\mathcal{F}\left\{h_1(x_2,y_2)\int\limits_{y_s}\int\limits_{x_s} o(x_2-x_s,y_2-y_s)\,\mathrm{d}x_s\,\mathrm{d}y_s\right\}\tilde{P}_1(x_3,y_3)\right]\otimes\mathcal{F}\left\{d(x_4,y_4)\right\}. \tag{6.17}$$

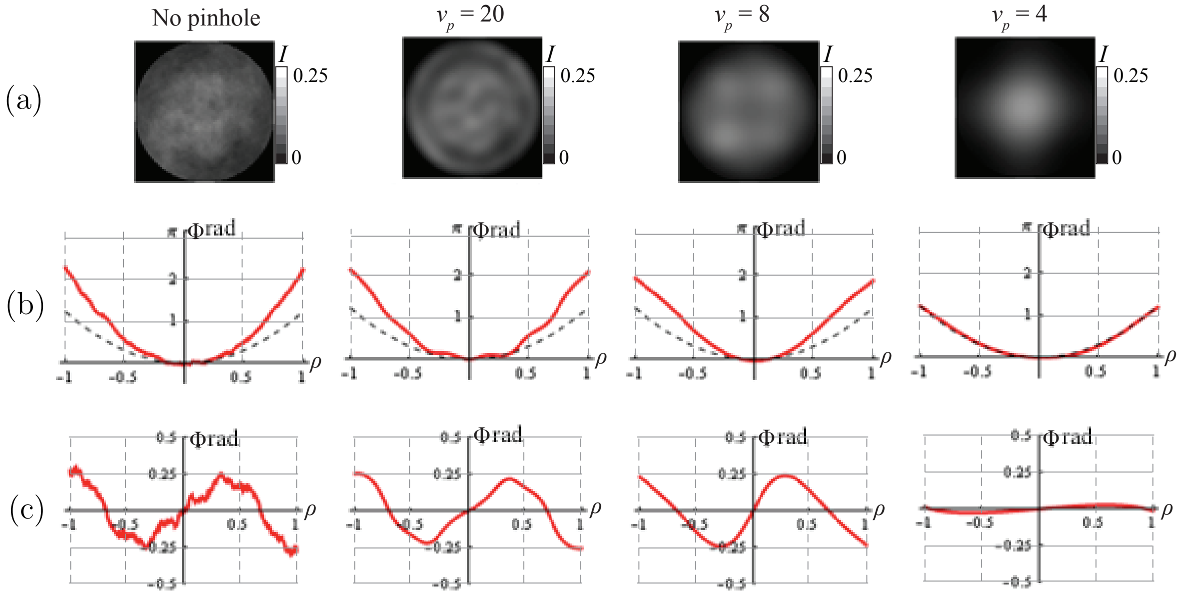

Figure 6.9: Effect of using pinholes of different sizes for axial selectivity. (a) Pupil intensity before the WS calculated by using pinholes of various radii, v_p, as the transmission mask. (b) Measured phase from even aberration astigmatism. (c) Measured phase from odd aberration coma. Where shown, the dashed lines show the induced aberrations of Fig. 6.3a. I is the normalised intensity of light reflected by a specular surface. The smoothing effect increased as the pinhole became smaller.

Fig. 6.9 shows simulations of the WS incorporating the pinhole for various radii, v_p, given by Eq. (2.35). As the pinhole became smaller, less light passed through, as expected. The smoothing effect also became stronger and when the pinhole was too small, the phase reading diminished. The pinhole acts as a spatial filter by blocking out the higher frequencies, resulting in the smoother signals. These data suggest that $v_p \geq 8$, which is approximately twice the size of the first zero of the focal spot [Sec. 2.6.1], is a sensible choice for wavefront sensing using light backscattered from volume specimens.

6.5 Wavefront Sensing using Shack-Hartmann Wavefront Sensor

The mathematical derivations and simulations in the preceding sections have thus far been based on calculation of phase from the averaged complex field in the WS pupil. A SHWS, however, measures the phase gradient (S^x, S^y) of the incident wavefront [Sec. 5.2], whose average complex field $\bar{U}_5$ is given by Eq. (6.16). Hence, the local phase gradient measured by the SHWS is given by Eq. (5.4) as:

$$\begin{aligned} S^x &= f\frac{\delta}{\delta x}\arg\left\{\bar{U}_5\right\} = f\frac{\delta}{\delta x}\arg\left\{\left[(P_1 \otimes O_s)\tilde{P}_1\right] \otimes \mathcal{F}\left\{d\right\}\right\}, \\ S^y &= f\frac{\delta}{\delta y}\arg\left\{\bar{U}_5\right\} = f\frac{\delta}{\delta y}\arg\left\{\left[(P_1 \otimes O_s)\tilde{P}_1\right] \otimes \mathcal{F}\left\{d\right\}\right\}. \end{aligned} \tag{6.18}$$

It has already been shown in the previous sections that the argument of the average complex field $\bar{U}_5$, used in the theoretical model of the WS, yields phase measurements. Therefore, it is reasonable to assume that the equation will also hold for general volume specimens, and it is a reasonable equivalent expression for the measurement by a SHWS.

The SHWS uses the centroid measurements to estimate the set of Zernike polynomial coefficients **a** given by Eq. (5.8). Sets of the coefficients **a** from multiple consecutive measurements can be taken and averaged to achieve reliable and stable readings. Since Eq. (5.8) is linear, the averaging of the coefficients is equivalent to the averaging of the vector **S**, and hence, the spot centroid displacements.

6.6 Experimental Design

Fig. 6.10 shows a simplified schematic of the wavefront sensing system used for the experimental verification of the simulated model. The specifications of the various equipment used in the set-up are provided in Tab. 6.1. Light of wavelength 633nm from

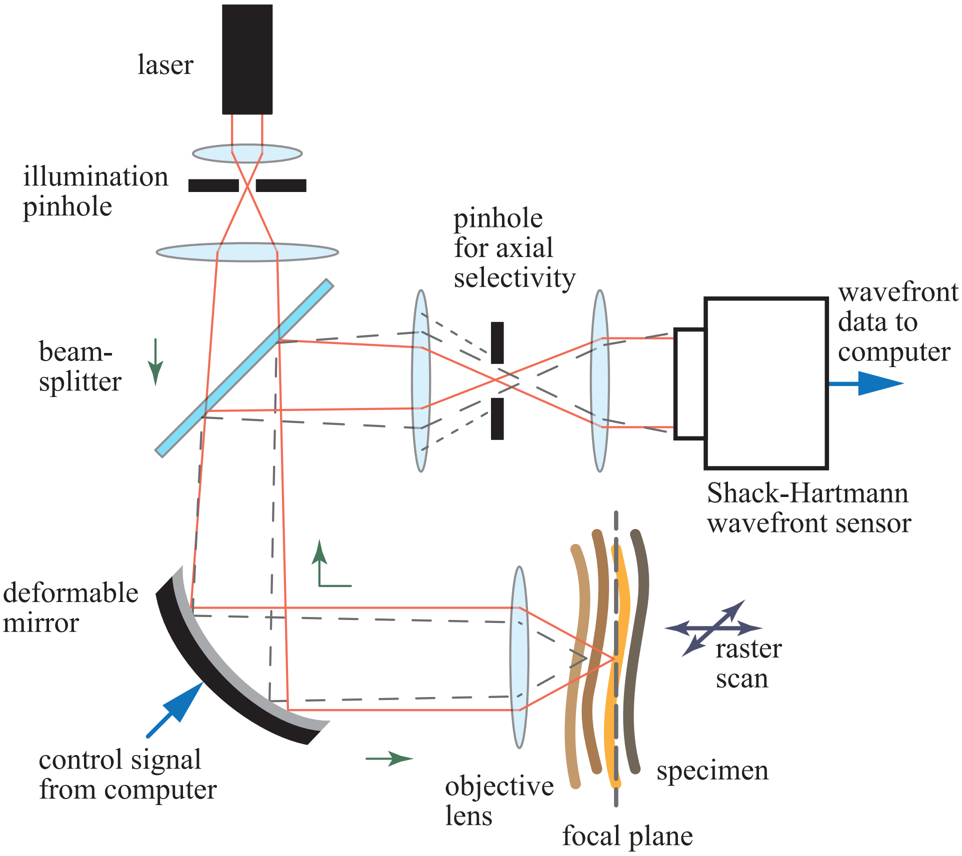

Figure 6.10: Simple schematic of a dual-pass wavefront sensing system. Some optical elements have been omitted for clarity.

a laser source was expanded by a suitable lens to form a divergent beam that illuminated the DM, hence compensating for the DM curvature arising from the biasing of the mirror [Sec. 5.3.1]. The OKO mirror allows correction of low-order optical aberrations. It has a 15mm diameter aluminium-coated circular mirror membrane made of silicon nitride, and its 37 electrodes are arranged in a hexagonal structure within a 12mm diameter circle. As explained in Sec. 5.3, 10mm diameter aperture on the DM was used to achieve better reproduction of Zernike modes, especially at the edges. This was also experimentally verified in a single pass set-up by detecting the Zernike aberration produced by the DM, using the SHWS. The aperture diameter of light incident on the DM was varied.

Light reflected by the DM was focussed by an objective lens to probe a specimen that was placed on a stage. A water immersion objective lens was used so that water filled the gap between the lens and the coverslip of the specimen to alleviate any spherical aberrations. The stage allowed raster scanning of the specimen.

Laser	*Thorlabs He-Ne* Wavelength (λ) = 633nm
Stage	Piezo-electric
Deformable mirror	*OKO Technologies* Aperture shape = circular Mirror Coating = Al Aperture Diameter = 15mm Active aperture diameter = 12mm Number of electrodes = 37 (19) Maximum deflection of the mirror centre = 9μm
Wavefront sensor	*Thorlabs Shack-Hartmann WS150* Aperture = 5.95mm × 4.76mm (max.) Maximum resolution = 1280 × 1024 pixels Maximum number of lenslets = 39 × 31 = 1209 Exposure range = 77μs – 1.36s Frame rate = 0.735 – 15Hz
Objective Lens	*63× Zeiss 1.2NA water immersion*

Table 6.1: Specifications of apparatuses used to experimentally investigate the effect of specimen structure in dual-pass direct wavefront sensing.

Light backscattered from the specimen was incident on the DM once more in the detection path, which was split by a beam-splitter and passed through a $4f$ lens system. Firstly, this $4f$ system served to demagnify the beam so that it can be picked up completely by the CCD camera on the SHWS. Secondly, it was used to collimate the convergent beam reflected by the DM. Thirdly, the lens system was used to focus the light through an axial selectivity WS pinhole, which served the essential task of filtering out out-of-focus light.

In the previous sections it was shown that the intensity in the pupil plane before the WS varies due to the backscattering of light from a specimen. The use of a pinhole for axial selectivity also blocks light. Consequently, the darker regions in the pupil will correspond to missing spots in the Hartmann spot pattern. The non-uniform intensity also gives rise to brighter regions in the pupil that may cause saturation of the CCD sensor, whereby the centroid cannot be correctly calculated. These missing centroid measurements will inevitably cause errors in wavefront measurements. Labview software was used to carry out the experiments. It was programmed to use the reference spot positions [Sec. 5.2] where a spot was missing or saturated, yielding a zero local phase gradient. The software also allowed automated measurements suited to the purpose of this experiment.

6.6.1 Experimental Procedure

During the experiments, the DM was used to induce the aberration modes Z_5 to Z_{11} inclusive, one at a time, in order to simulate specimen-induced aberrations [Sec. 6.1]. The amplitude of the Zernike modes was swept from -0.6 to 0.6 RMS radian, in steps of 0.2 RMS radian. Higher amplitudes caused the OKO membrane mirror electrode voltage to saturate. For each amplitude of the Zernike modes induced, averaging was achieved, firstly, via long exposure of the specimen while it was being scanned. Secondly, several of the resulting pupil images were recorded by the SHWS and further averaged. The aberrations read by the SHWS prior to aberration induction by the DM were recorded and the change in Zernike coefficients as a result of inducing aberrations by the DM were estimated from the averaged pupil image. The exposure time and number of images averaged were selected so as to achieve a uniform pupil intensity at the SHWS, which in turn produced steady coefficient measurements. The averaging via multiple images could have also been achieved using a single image taken at a higher exposure, but at the cost of reducing the intensity of the light source, which would otherwise saturate the CCD sensor. Additionally, several measurements of the coefficients were recorded. The multiple readings provided an averaged estimation and were used to calculate the standard deviation of the data so as to provide an indication of the repeatability of wavefront sensing.

6.6.2 Positioning Pinhole for Axial Selectivity

The pinhole used for axial selectivity must be positioned correctly. Firstly, its misplacement away from the focal plane will cause light from out-of-focus plane within the specimen to be collected by the SHWS, leading to wavefront sensing from the wrong plane, which the SHWS will detect as a defocus in the system. Secondly, if the pinhole is not centred in the focal plane, backscattered light focussing through the pinhole will be blocked, leading to missing spots in the SHWS pupil. Since the software will fill these missing spots with reference spot positions [Sec. 6.6], too many missing spots will cause the failure to correctly measure the wavefront. For small phase changes, the focal spot might only be partly blocked, but the error in measurement will be particularly high when high amplitudes of aberrations are present, and more spots will be missing.

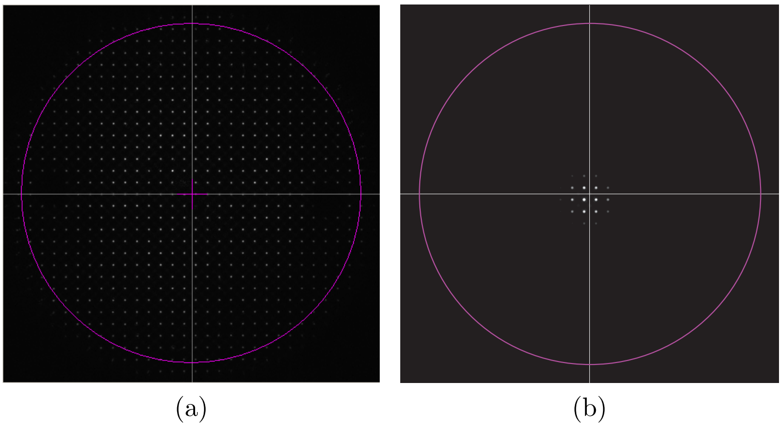
(a) (b)

Figure 6.11: Hartmann spots used as reference to align pinhole used for axial selectivity in wavefront sensing. (a) Uniform spot pattern produced by a mirror in focus, and when pinhole is correctly positioned in the focal plane. (b) Spot pattern seen on the SHWS as a result of high defocus in the system. If the pinhole is not centred, the spots are not centred in the defined SHWS aperture.

In order to position the pinhole, a mirror was placed on the stage, in the focal plane of the objective. This corresponded to a maximum signal registered by the photomultiplier tube (PMT) of the confocal microscope and zero defocus, Z_4, measured by the SHWS. The pinhole was then roughly centred with focal spot with the aid of the SHWS. When the pinhole was in the vicinity of the focal plane and allowed the focal spot to pass through fully, the SHWS showed a uniform Hartmann spot pattern and zero defocus, show in Fig. 6.11a. To accurately position the pinhole in the focal plane, ±1 RMS radian of defocus was then induced by the DM. The pinhole was then positioned along the axial direction to ensure that ±2 RMS radians of defocus was detected by the SHWS due to the dual-pass phenomenon. To centre the pinhole in the transverse direction, ±3 RMS radians of defocus was induced by the DM, sufficiently high enough to form a spot in the pupil plane of the SHWS, the spot pattern being shown in Fig. 6.11b. Displacement of the pinhole in the transverse direction will cause the spots to be off-centred in the SHWS pupil. The pinhole was therefore positioned in the transverse direction with the aid of this spot pattern.

6.6.3 Eliminating Stray Light

A lower intensity of light was expected to be backscattered as opposed to light reflected by a specular surface. Therefore, it was necessary to ensure that light reflected by system optics did not compromise measurements. Especially, since these surfaces are specular and being used in a dual-pass system, they can greatly affect wavefront measurements. The appropriately coated optics were used to prohibit significant back reflections. To ascertain this, the system was tested without a specimen. Subsequently, any light detected by the SHWS would either be reflected by the system optics, or from the surrounding. The latter was eliminated by operating in a dark room and by placing a shield around the SHWS to block any light from laboratory equipment. It was found that negligible stray light was detected by the SHWS at the exposures it was being operated.

Despite the aforementioned precautions, the SHWS was very sensitive to light during very short exposure experiments and detected back reflections mainly from the pupil of the objective. Since the intensity of light from back reflections was lesser than the actual signal from the specimens, it was set as the noise threshold in the Labview software and thereby eliminated. For stronger external signals, the software was also programmed with a differential imaging technique whereby it can save the image of the unwanted light and subtract it to achieve the required image for wavefront sensing.

6.7 System Calibration

The DM was calibrated using an interferometric set-up [76] to recreate Zernike modes up to Z_{11}. This interferometer system provided a method of system calibration that was independent of the SHWS. Higher-order modes were not included as they can only be produced by this DM in small amplitudes [73], and only the low-order modes are sufficient for accurate representation of many typical microscope aberrations [76]. It must also be noted that the DM cannot recreate pure Zernike modes and cross-talk between different modes is expected. The SHWS was calibrated using an expanded collimated beam to estimate aberrations up to Z_{15}. A few higher modes were included to analyse cross coupling [Sec. 5.2.2] due to the SHWS wavefront reconstruction.

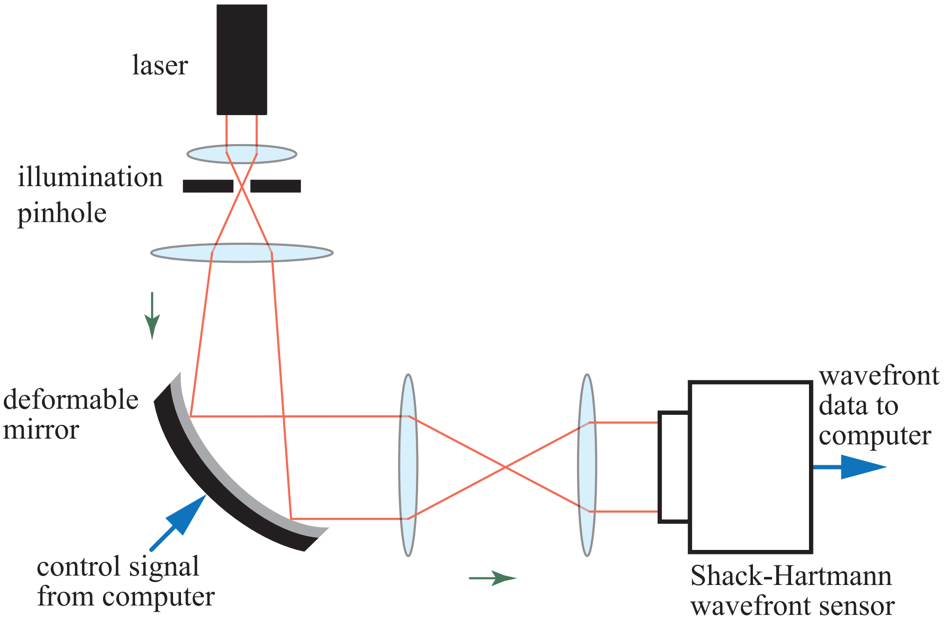

Figure 6.12: Simple schematic of a single-pass wavefront sensing system. Light reflected from the DM is fed into the WS, allowing the aberration modes created by the DM to be detected.

A single-pass wavefront sensing system was set up, as shown in Fig. 6.12. A collimated beam of diameter 10mm was reflected by the DM. The beam was demagnified to 3.6mm diameter before being incident on the SHWS. This illuminated area corresponded to using 416 lenslets for wavefront estimation within the defined circular pupil. The experiment was carried out as outlined in Sec. 6.6.1.

Fig.6.13a shows the coefficients estimated by the SHWS when astigmatism, Z_5, was induced by the DM. The black bars show the maximum change of coefficients for the modes Z_4 to Z_{15}, inclusive. For a ± 0.6 RMS radian sweep of Z_5, approximately ± 0.74 RMS radian change was observed by the SHWS, which as Fig. 6.13c shows, is 23% higher than the actual induced aberration. Additionally, small readings of Z_6 and Z_8

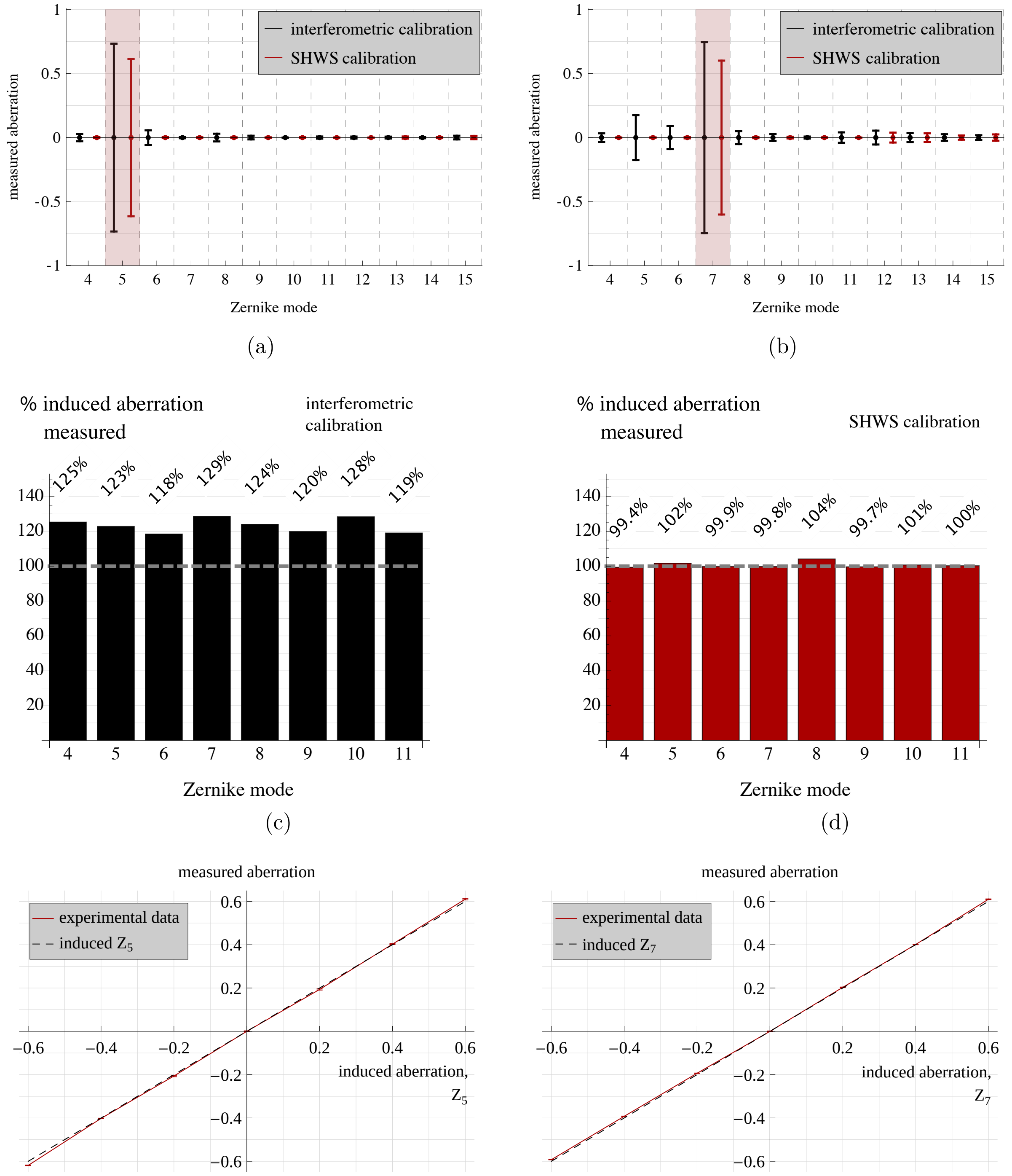

(a) (b) (c) (d) (e) (f)

Figure 6.13: Calibration of the DM. (a) – (b) For interferometrically-calibrated and SHWS-calibrated DM, maximum measured amplitude of all Zernike modes from the induction of Z_5 and Z_7, respectively, by the DM. Graphs show cross-talk with other modes. The DM-induced Zernike modes are highlighted in the graphs. (c) – (d) Bar chart shows the percentages of induced aberrations measured by the SHWS from interferometrically-calibrated and SHWS-calibrated DM, respectively. (e) – (f) Measured aberration as a function of induced aberrations of Z_5 and Z_7, respectively, for SHWS-calibrated DM.

were recorded. The disproportionate and erroneous readings may be a consequence of the sampling and gradient averaging rendered by the lenslets of the SHWS, mode cross coupling due to estimation using Zernike polynomial derivatives [Sec. 5.2.2], and cross-talk of modes due to the imperfect rendering of modes by the DM. Also, the light used to calibrate the SHWS may not be perfectly collimated. Subsequently, the measurements will be off.

To rule out any such errors during the experiment, the DM control system from interferometric calibration was trained and re-calibrated using the SHWS data. This has the effect of creating modes that are orthogonal for the SHWS. The corresponding data is shown using the red bars in Fig.6.13a. A ±0.6 RMS radian change was observed for Z_5 and readings of any other coefficients were reduced. A significant reduction of cross-talk was observed for Z_7, where the SHWS measured significant amounts of Z_5 and Z_6 prior to re-calibration. Furthermore, Fig. 6.13d shows that the re-calibration has enabled the DM to create modes in the right proportions with respect to the SHWS measurements, as all the modes are detected at approximately 100% of the amount induced.

Fig.6.13e and Fig.6.13f show a linear relationship with the DM-induced aberrations of Z_5 and Z_7, respectively, in the x-axis and the aberration measured by the SHWS in the y-axis. The dashed lines show the induced aberration, which clearly is overlapped by the experimental measurements. This is further confirmation of the bar chart of Fig. 6.13d. The error bars are too small to be visible on this scale. The maximum standard deviation observed was approximately ±0.004 radian, which is a deviation of only ±2% of the 0.2 RMS radian changes used in the experiment.

6.8 Experimental Results

With the set-up shown in Fig. 6.10, the SHWS measures aberrations from the light backscattered from volume specimens placed on the stage. Taking into account the initial system and specimen-induced aberrations detected by the SHWS, the DM was used to induce known aberrations as outlined in Sec. 6.6.1. The changes in aberration modes corresponding to the changes induced by the DM were measured from the backscattered light. These measurements were used to analyse the performance of the dual-pass direct wavefront sensing system for various specimen structures. All the experimental results herein have been obtained following these procedures. Any special settings for specific specimens have been mentioned in the pertinent sections.

6.8.1 Mirror

It was shown in Sec. 6.2.2 that a specular specimen, such as a mirror, yields twice the induced even aberrations and no odd aberrations in a dual-pass set-up. To measure this phenomenon, a mirror was placed on the specimen stage of the dual-pass wavefront sensing system of Fig. 6.10. An aperture of diameter 10mm was illuminated on the DM. The light reflected by the mirror was demagnified to 4.1mm diameter to form the input to the SHWS. As a result, 540 lenslets were used by the SHWS for aberration estimation. The measurements were taken with the exposure of the SHWS set at 523μs, except when the 50μm pinhole was used, when the exposure was set to 800μs. Averaging was not necessary for the mirror specimen, but 5 measurements were made for each amplitude induced by the DM. The multiple measurements were used for coefficient averaging, and to calculate the standard deviation of the data.

Fig. 6.14 shows the measurements made by the SHWS on induction of the even modes of astigmatisms, Z_5 and Z_6. Pinholes of numerous diameters ranging from 50μm to 600μm were used as the axial selectivity WS pinhole. Using Eq. (2.41), the diameter of the aberration-free Airy disc at the position of the pinhole was 30.9μm. It can be seen that the measurements made with the 200μm, 300μm and 600μm pinholes were almost identical to the measurements made without a pinhole in place. They show an almost two-fold maximum amplitude measurement of ±1.2 RMS radian against a ±0.6 RMS radian induction of the aberrations, as predicted by theory.

It was shown in Sec. 6.4 that the simulations suggested pinholes approximately twice

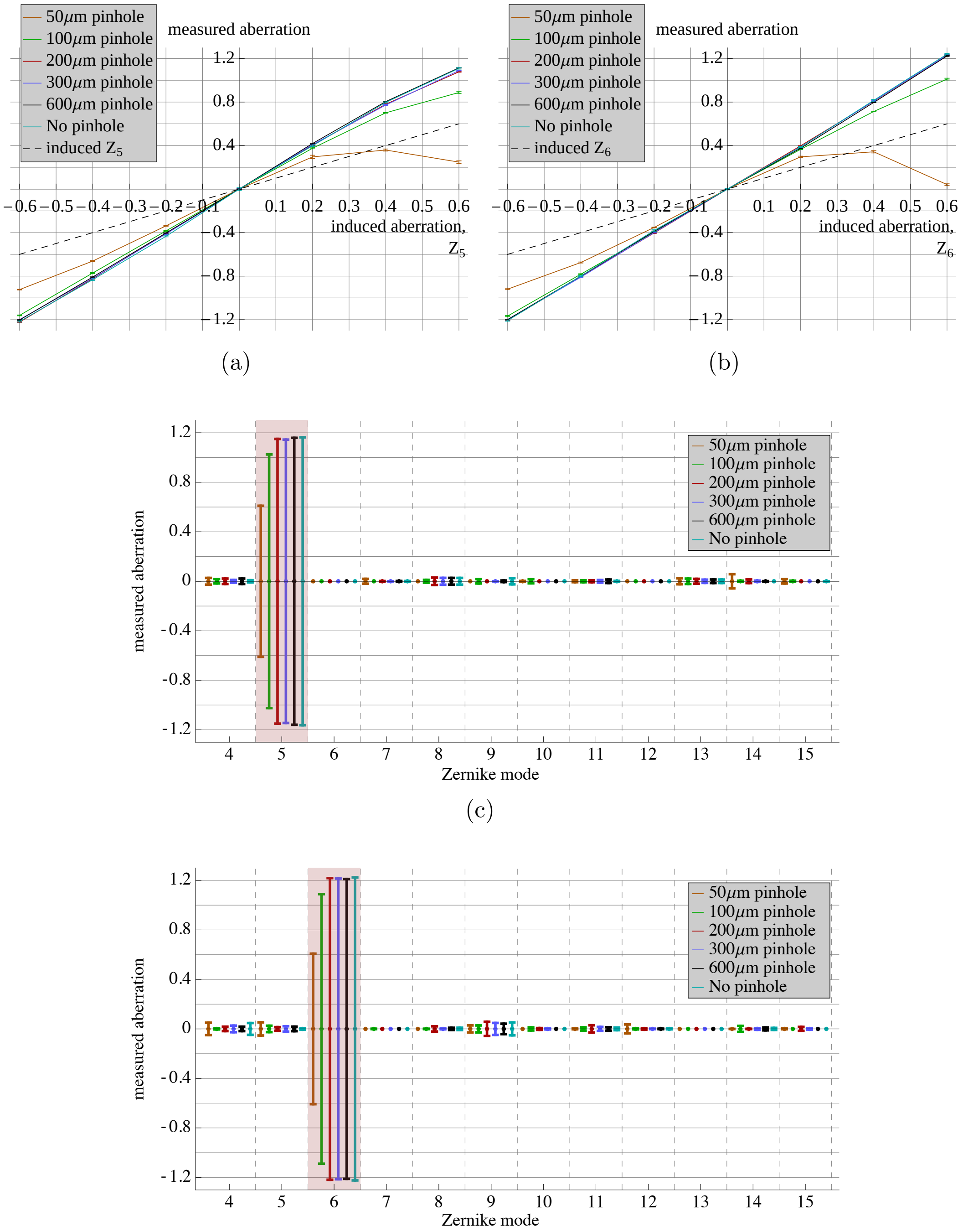

(a) (b) (c) (d)

Figure 6.14: SHWS measurements of even aberration modes Z_5 and Z_6, respectively, which were induced by a DM and reflected back by a mirror. (a) – (b) Measured aberration as a function of induced aberration. (c) – (d) Maximum measured amplitude of all Zernike modes, showing cross-talk between modes. The DM-induced Zernike modes are highlighted in the graphs.

as large as the aberration-free Airy disc would allow estimation of phase changes due to low-order aberrations within an amplitude range of ±0.5 RMS radian. A smaller pinhole in effect causes smoothing of the aberration, which means that a smaller amplitude is detected by the sensor. The 50μm pinhole was only 1.6 times larger than the Airy disc, and hence the gradient of the line from the measurements was noticeably smaller. The 100μm pinhole was 3.2 times larger than the Airy disc, and so the readings were similar to those for the pinholes larger than 100μm, for both Z_5 and Z_6. The measured aberrations for the 50μm and 100μm pinholes were smaller for the positive induced amplitudes ranging between 0.2 to 0.6 RMS radian compared to the equivalent negative amplitudes. The skewness of the readings was caused due to the slight misplacement of the WS pinhole from the focal plane, resulting in more light being blocked due to higher phase variations in one direction than in the other [Sec. 6.6.2]. Fig. 6.14c and Fig. 6.14d show that there was negligible cross-talk between the Zernike modes during the estimation of the astigmatisms.

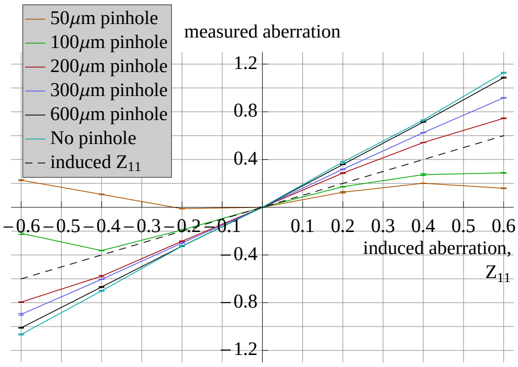

(a)

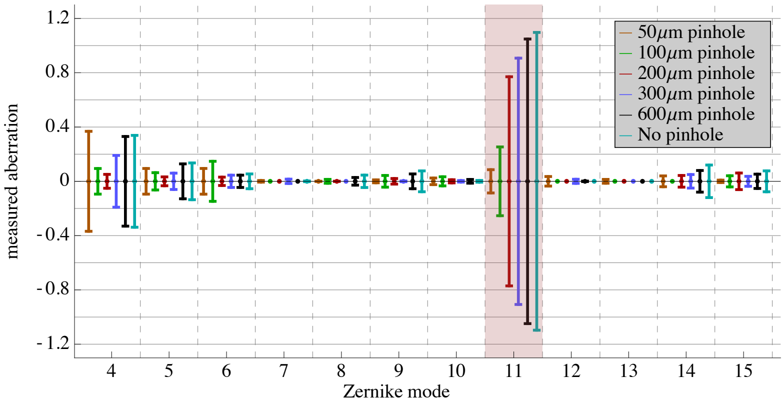

(b)

Figure 6.15: SHWS measurements of even aberration mode Z_{11}, which was induced by a DM and reflected back by a mirror. (a) Measured aberration as a function of induced aberration. (b) Maximum measured amplitude of all Zernike modes, showing cross-talk between modes. The DM-induced Zernike mode is highlighted in the graph.

Fig. 6.15 shows the measurements of Z_{11} made by the SHWS. It can be seen that the size of the WS pinhole had more effect on the first spherical aberration than on the astigmatisms. Fig. 6.15b illustrates that the 50μm and 100μm pinholes caused detection of other modes comparable to the amount of Z_{11} detected, and can therefore be said to have been too small for the purpose of successfully detecting Z_{11} for the size of the Airy disc in this set-up. The 200μm pinhole produced the least cross-talk. However, twice the amount of induced Z_{11} was not detected as predicted by theory. The experiments conducted with the 300μm and 600μm pinholes, and without a pinhole showed a ± 0.2 – ± 0.35 radian cross-talk of defocus, Z_4, against as estimation of ± 0.9 – ± 1.1 radian of Z_{11}.

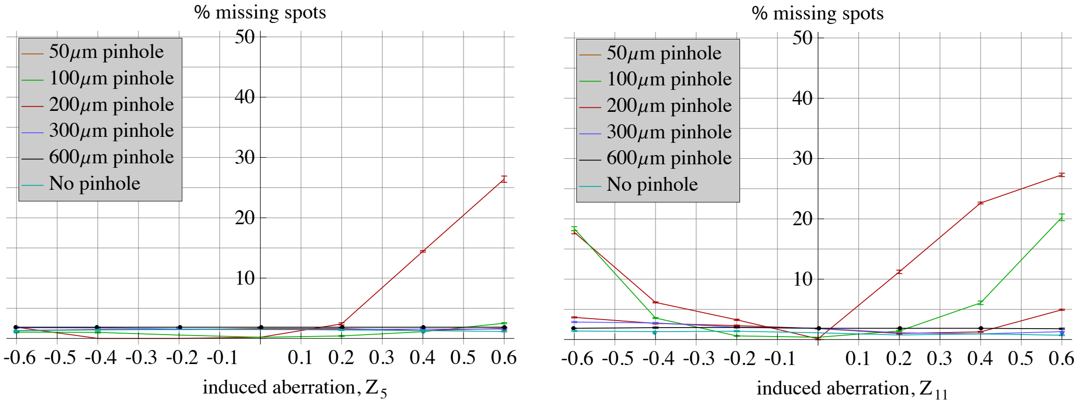

(a) (b)

Figure 6.16: Graphs showing the percentages of missing spots for various pupil sizes in the SHWS pupil due to (a) Z_5 and (b) Z_{11}.

Fig. 6.16 shows the percentages of missing spots registered within the defined 4.1mm pupil of the SHWS as Z_5 and Z_{11} were induced by the DM. Fig. 6.17a and Fig. 6.17b show the cross-sections of the phase and phase gradient in the x direction of 1 radian of Z_5 and Z_{11}, respectively. Due to the dual-pass phenomenon, the induced 0.5 radian aberration is expected to double. Hence, the cross-sections for 1 radian of aberration is shown in the graphs. It can be seen that firstly, the peak-to-peak phase for Z_{11} is about 0.92 radian higher than for Z_5, and secondly, the phase gradient of Z_{11} is much greater. Due to the high phase gradient, more rays aberrated by Z_{11} are likely to fall outside the pinhole aperture [Sec. 6.4]. Furthermore, the pinhole causes a smoothing effect, as observed in the simulations in Sec. 6.4. Therefore, it is likely that the phase due to Z_{11} appears like Z_4 after being smoothed by the pinhole. As a result, significant cross-talk of Zernike modes is observed for Z_{11} in comparison to the astigmatisms, Z_5 and Z_6.

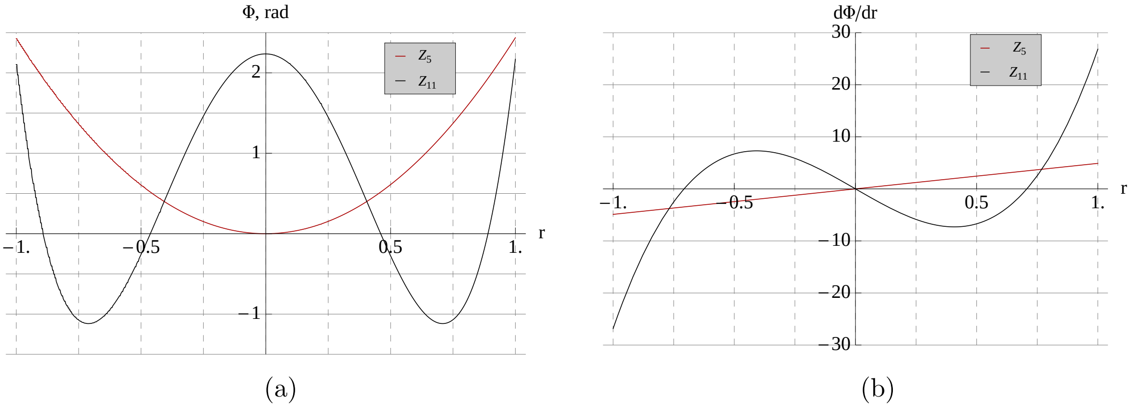

(a) (b)

Figure 6.17: Comparison of (a) phase and (b) phase gradient of Z_5 and Z_{11} along the diameter of the pupil at $\theta = 0$ radian.

Ignoring the case of the 50μm pinhole, which clearly blocked too much light, it was found that less than 2% of spots were missing during the measurements of Z_5 and Z_6. However, a maximum of 20%, 5.5% and 3% spots were missing for the 100μm, 200μm and 300μm pinholes, respectively, which caused the difference in the estimations of mode Z_{11}. The results for the 600μm pinhole show that the pinhole was large enough to yield almost identical results to the scenario without a pinhole.

Fig. 6.18 shows the percentages of the induced aberrations detected by the SHWS. It was calculated from the gradient of the best-fit linear regression lines of the preceding graphs that show the measured aberration as a function of induced aberration. The 50μm pinhole is not shown since the previous measurements showed that its usable range was too small. Aside from the results using the 100μm pinhole, nearly twice the induced amplitude of astigmatism was detected, as predicted by theory. Due to the smoothing effect of the WS pinhole, a smaller amount of Z_{11} was detected by the SHWS, with the proportion decreasing as the pinhole size decreased. Even without a pinhole in position, the SHWS failed to detect 200% of Z_{11} as would be expected in a dual-pass set-up, which could happen due to any of the aforementioned reasons. The error bars in the graphs showing measured aberration as a function of induced aberration were generated as a consequence

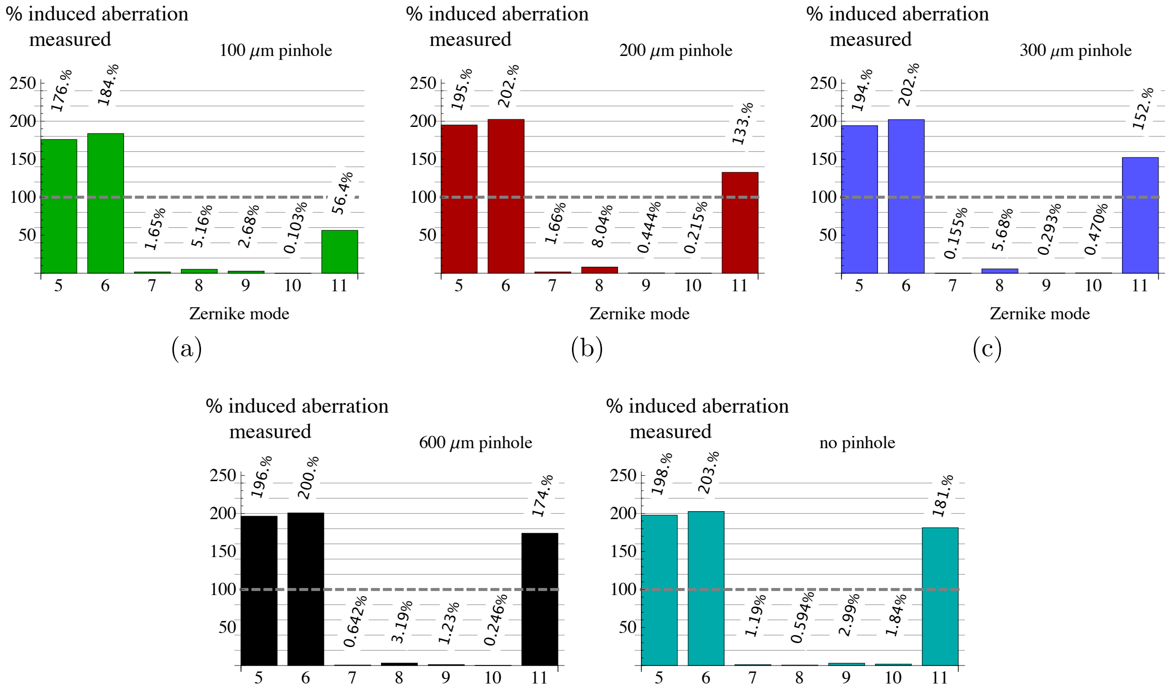

(a) (b) (c)

(d) (e)

Figure 6.18: Bar charts showing the percentages of induced aberrations detected by the SHWS from light backscattered from a mirror using (a) 100μm, (b) 200μm, (c) 300μm, (d) 600μm and (e) no WS pinhole.

of taking 5 measurements for each amplitude induced by the DM. They showed that the measurements had a maximum standard deviation of ±0.012 radian.

6.8.2 Sample of 200nm Beads Suspended in Gelatine

To test the behaviour of the dual-pass wavefront sensing system, a model specimen was created using polystyrene beads of diameter 200nm. The diameter of the aberration-free Airy disc produced by the 63× Zeiss 1.2NA water immersion lens was calculated to be approximately 644nm, using Eq. (2.41). Therefore, the beads appeared as point scatterers compared to the focal spot. A reasonable density of beads was required to model the specimen. If the density is too high, meaning that the beads are very closely packed, then the scattering would be too high, causing most of the light to be lost in the process. On the other hand, if the density of the scatterers is far too low, then also there will be negligible backscattered light. Mixtures of various densities were thus created by

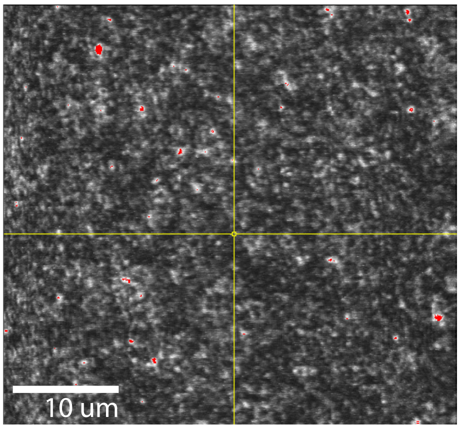

Figure 6.19: Confocal image of a sample of 200nm beads suspended in gelatine at a depth of approximately 35μm from the coverslip.

diluting the beads in water. Each mixture was mixed with powdered gelatine and then allowed to settle between a glass slide and a glass coverslip, resulting in the beads being suspended in 3D space. The specimens of different densities were tested and a suitable specimen exhibiting moderate scattering was chosen, whose confocal image is shown in Fig. 6.19.

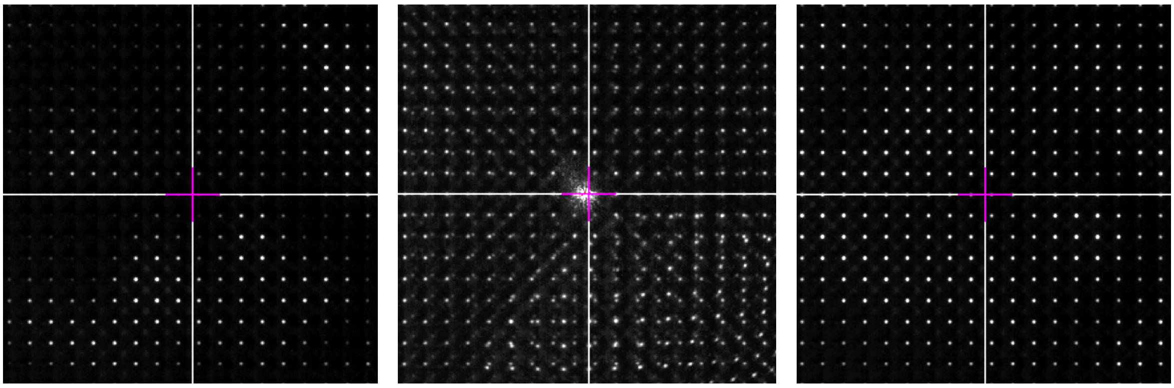
(a) (b) (c)

Figure 6.20: Sample Hartmann spot patterns from light backscattered from a sample of 200nm beads suspended in gelatine. (a) Sample was stationary and a 200μm pinhole was used for axial selectivity. The intensity across the pupil varied extensively. (b) Sample was scanned and image was averaged, and no pinhole was used. Uniform intensity was achieved, but out-of-focus light caused multiple spots within each sub-aperture domain. (c) Image was scanned and averaged, and a 200μm pinhole was used for axial selectivity. Uniform intensity was achieved across the SHWS aperture, suitable for wavefront sensing.

Fig. 6.20 shows images of spot patterns on the SHWS arising from light backscattered from the bead specimen, and illustrates the need for a pinhole for axial selectivity and averaging. Fig. 6.20a shows that a non-uniform pupil intensity was observed on the

SHWS from the stationary scattering specimen with a 200μm pinhole in position for axial selectivity. A uniform intensity was achieved by scanning and averaging the image in the pupil of the SHWS using a suitable exposure time of the CCD camera [Sec. 6.3], as Fig. 6.20b shows. However, light from out-of-focus layers were also incident on the SHWS without a pinhole in position, causing lenslets to form multiple focal spots in each sub-aperture of the SHWS. Finally, as Fig. 6.20c shows, the combination of both averaging and using a pinhole resulted in a smooth intensity across the pupil and eliminated spots arising from out-of-focus light.

To perform the averaging, the exposure of the SHWS was set to 45ms for the 200μm pinhole, and to 35ms for the 300μm and 600μm pinholes, which were much longer than the exposures used for the mirror, in Sec. 6.8.1. Further to averaging via long exposure, the pupil intensity in the SHWS was averaged using 10 consecutive frames, and coefficient averaging was performed by taking 5 measurements for each amplitude induced by the DM.

Light from back reflections were eliminated as detailed in Sec. 6.6.3. However, a strong signal was reflected by the coverslip. To avoid false measurements due to this specular surface, light had to be focussed deep within the specimen such that the pinhole used for axial selectivity blocked the reflected light. The experiment was conducted as outlined in Sec. 6.6.1.

Fig. 6.21a shows the response of the SHWS to the even aberration astigmatism, Z_5, as induced by the DM. Pinholes of diameters 200μm, 300μm and 600μm were used. The graph clearly illustrates that as the pinhole size increased, a higher proportion of Z_5 was detected. A linear relationship between the induced and measured aberration was observed. However, the correct proportion of aberration was not measured, as already predicted in the simulations [Sec. 6.2.3]. The single-pass data from Fig. 6.13a showed negligible cross-talk in the estimation Z_5 after training the DM using the SHWS. But Fig. 6.21b shows that the SHWS erroneously estimated small proportions of other modes for all three pinholes due to the backscattered light causing ambiguity, in addition to the

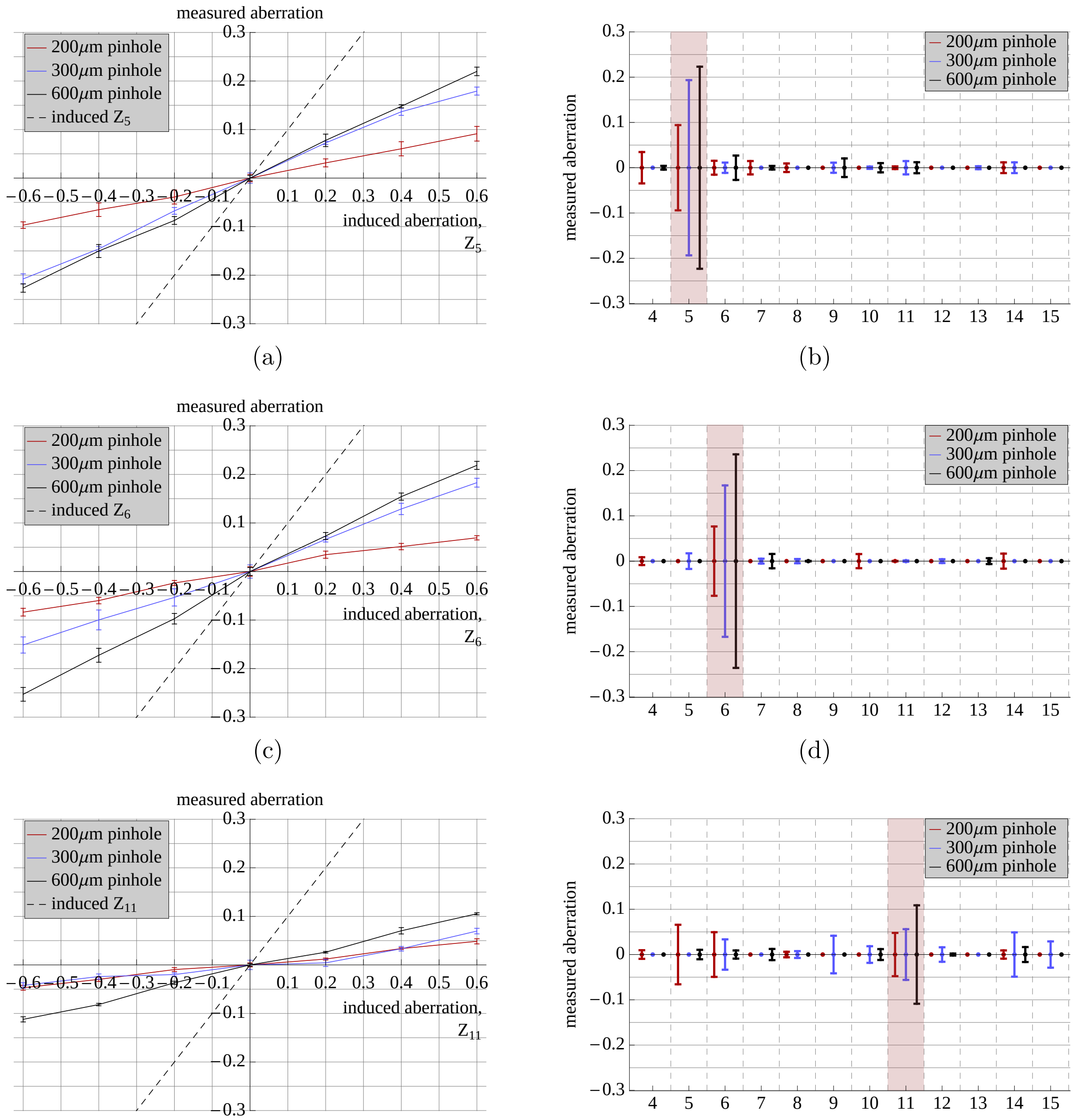

(a) (b)

(c) (d)

(e) (f)

Figure 6.21: SHWS measurements of even aberration modes Z_5, Z_6 and Z_{11}, respectively, which were induced by a DM and scattered back by a sample of 200nm beads suspended in gelatine. (a), (c) and (e) Measured aberration as a function of induced aberration. (b), (d) and (f) Maximum measured amplitude of all Zernike modes, showing cross-talk between modes. The DM-induced Zernike modes are highlighted in the graphs.

smoothing and phase gradient filtering of the pinhole [Sec. 6.4.] Fig. 6.21c and Fig. 6.21d show that similar measurements were made when Z_6 was induced by the DM.

From the gradient of the graphs in Fig. 6.21e, it is clear that a smaller proportion of the induced Z_{11} was measured compared to the astigmatisms. Fig. 6.21f shows that the SHWS detected noticeably higher proportions of other modes when the 200μm and 300μm pinholes were used, which were comparable to the detected amplitude of Z_{11}. Smaller amounts of cross-talk was observed for the 600μm pinhole. Clearly, this is a consequence of the smaller pinholes filtering out more light and giving rise to more missing spots in the SHWS, and the smoothing effect observed in the simulations [Sec. 6.8.1].

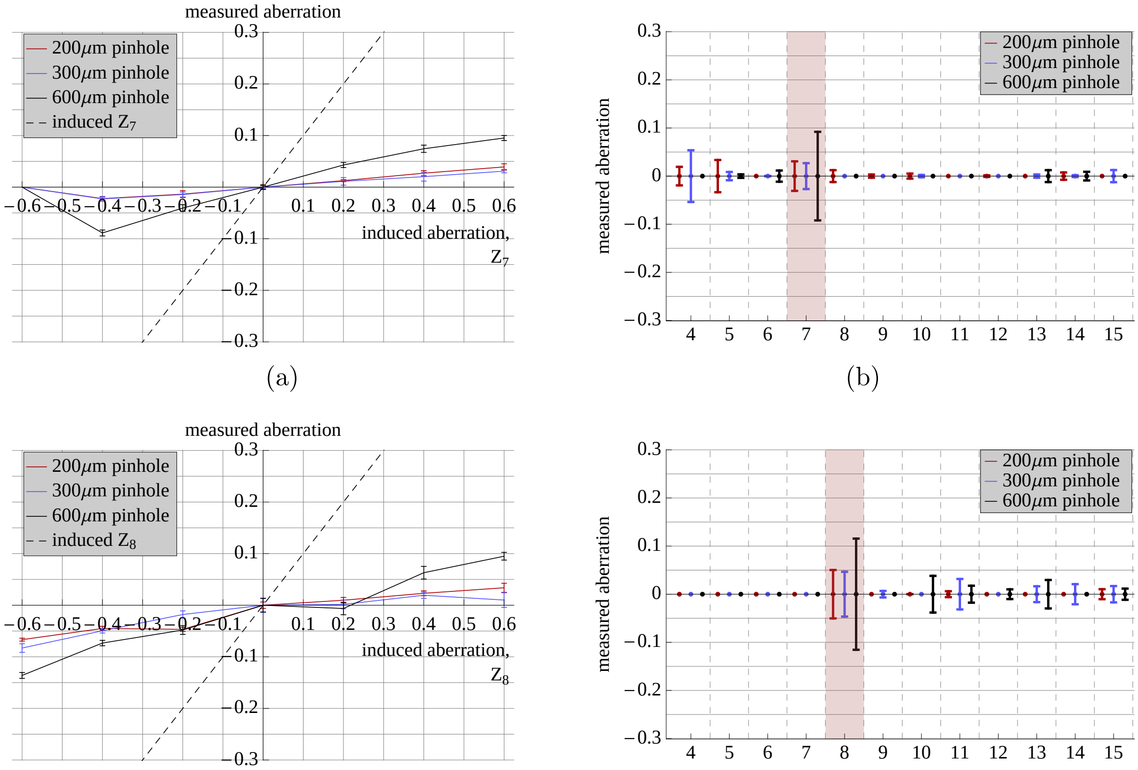

(a)

(b)

(c)

(d)

Figure 6.22: SHWS measurements of the odd aberration modes Z_7 and Z_8 (comas), respectively, which were induced by a DM and scattered back by a sample of 200nm beads suspended in gelatine. (a) and (c) Measured aberration as a function of induced aberration. (b) and (d) Maximum measured amplitude of all Zernike modes, showing cross-talk between modes. The DM-induced Zernike modes are highlighted in the graphs.

Fig. 6.22 and Fig. 6.23 show the aberration measurements made when the odd aberrations coma and trefoil, respectively, were induced by the DM. Although a linear relationship exists between the induced and measured aberrations, it appears that the filtering of the pinholes affected the coma modes more than the trefoils. As illustrated in Fig. 6.24, Z_7 has a much higher phase gradient than Z_9, and a wavefront affected by the former is thus likely to be filtered out more by a pinhole. During the experiments, the DM saturated when attempting to create -0.6 radian of Z_7. The measurement for that amplitude was ignored and set to zero, as indicated in the graph.

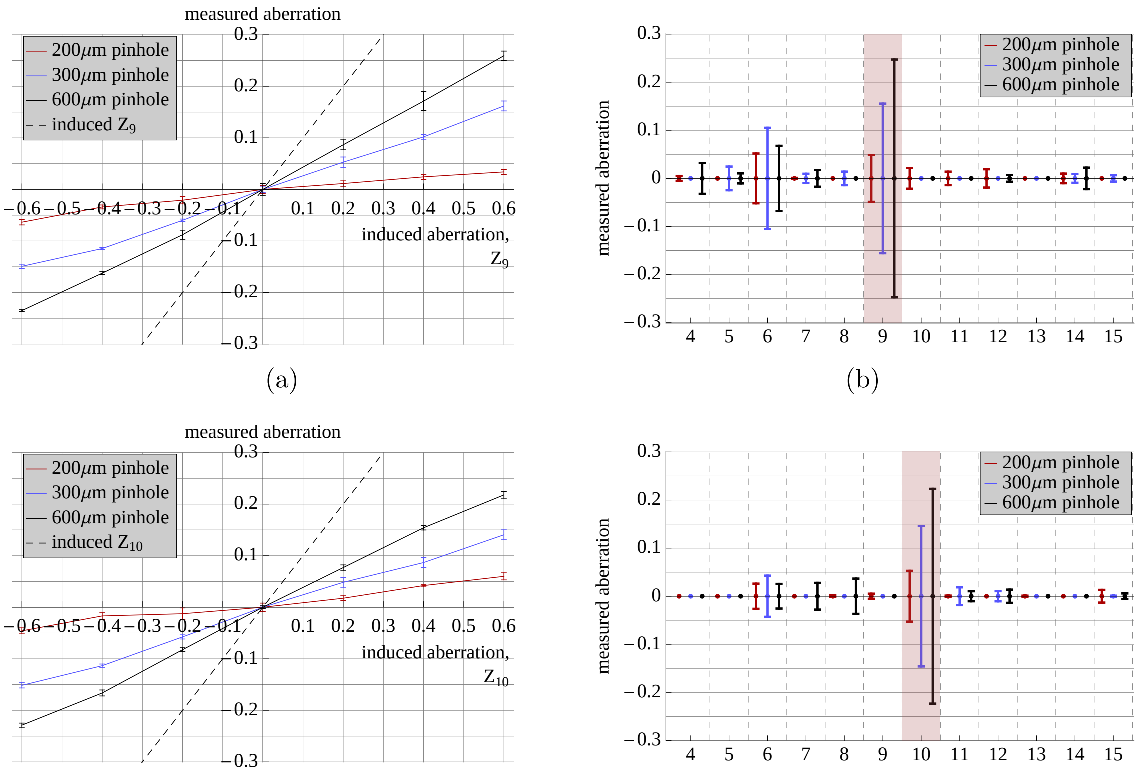

(a) (b)

(c) (d)

Figure 6.23: SHWS measurements of the odd aberration modes Z_9 and Z_{10} (trefoils), respectively, which were induced by a DM and scattered back by a sample of 200nm beads suspended in gelatine. (a) and (c) Measured aberration as a function of induced aberration. (b) and (d) Maximum measured amplitude of all Zernike modes, showing cross-talk between modes. The DM-induced Zernike modes are highlighted in the graphs.

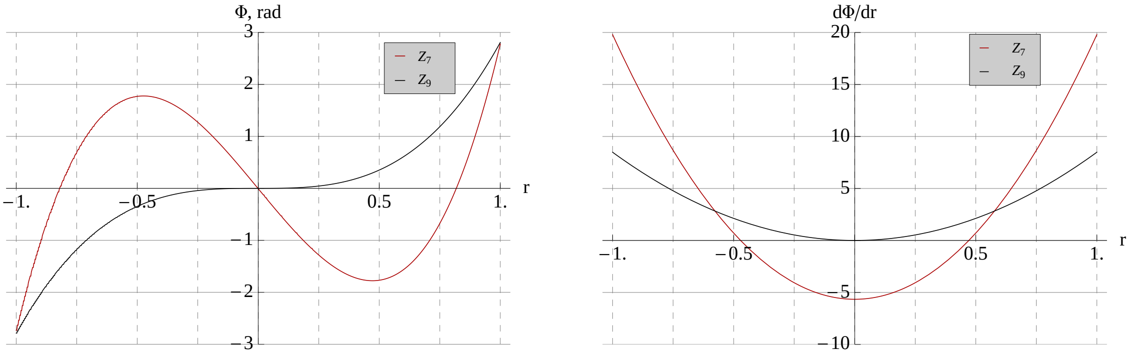

(a) (b)

Figure 6.24: Comparison of (a) phase and (b) phase gradient of Z_7 and Z_9 along the diameter of the pupil at $\theta = 0$ radian.

Some of these measurements show the presence of aberration modes other than those induced by the DM. Apart from cross coupling of Zernike modes during estimation by the SHWS, cross-talk with these other aberration modes could arise partly due to the ambiguous nature of scattering. Since the intensity of backscattered light varied across the pupil, missing spots were registered by the SHWS, leading to wrong estimation of aberrations. The size and position of the pinhole used for axial selectivity also played a key role [Sec. 6.6.2, Sec. 6.4]. Using Eq. (2.43), the axial width of the aberration-free focal spot was calculated to be 4.05 mm. Since the pinhole was centred by hand, it can be expected that the pinhole was within ±2 mm of the focal plane. As discussed in Sec. 6.6.2, an offset of the pinhole can give rise to erroneous estimation of aberrations as it blocks light. The size of the pinhole was the other contributing factor, particularly in the case of Z_{11}. As discussed in Sec. 6.4 and Sec. 6.8.1, the higher phase gradient of Z_{11} caused more light to be blocked by the 200μm and 300μm pinholes, which corresponds to the red and blue bars, respectively, in Fig. 6.21f. Due to the missing spots registered on the SHWS, reference spot positions were used, hence setting the gradient for missing spots to zero. This may potentially have caused errors as the wavefront was misrepresented using aberrations that were not present. Furthermore, the pinhole causes a smoothing effect [Sec. 6.4], which, for example, could cause the phase due to Z_{11} to appear like Z_4. The 600μm pinhole produced the better results in this experiment. Evidently, the erroneous detection of other modes cannot be eliminated in the process, but at the same time, too large a pinhole may compromise the property of axial selectivity. A smaller pinhole will be needed when imaging closer to the surface so that back reflections from the coverslip may be blocked.

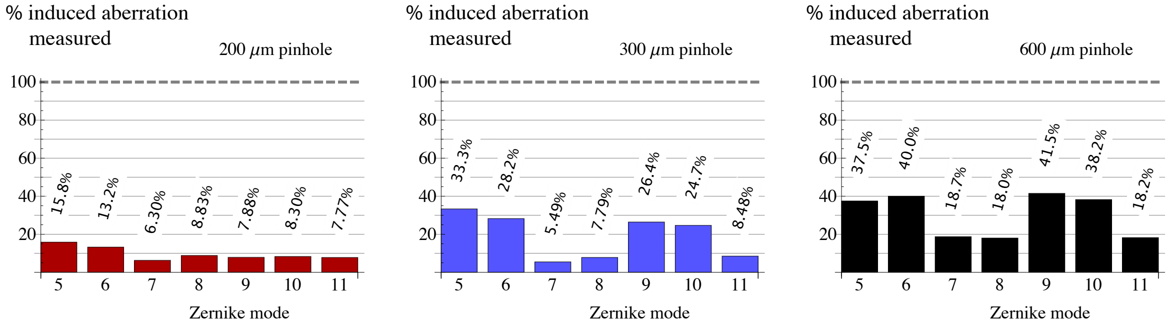

(a) (b) (c)

Figure 6.25: Bar charts showing the percentages of induced aberrations detected by the SHWS from light backscattered from a sample of 200nm beads using (a) 200μm, (b) 300μm and (c) 600μm WS pinhole.

Fig. 6.25 shows the percentages of the induced aberrations detected for each WS pinhole, calculated using the best-fit lines as outlined in Sec. 6.8.1. As the preceding graphs already showed, due to the smoothing effect of pinholes, increasing the pinhole size increased the proportion of the aberrations detected. In all cases, smaller portions of Z_7, Z_8 and Z_{11} were detected. Considering the case of the 600μm pinhole, approximately 40% of the induced Z_5, Z_6, Z_9 and Z_{10} were detected, and about 20% of Z_7, Z_8 and Z_{11} were detected. As the error bars in the graphs showing measured aberration as a function of induced aberration illustrate, the maximum standard deviation for each pinhole was observed to be less than ±0.02 radian. During the measurements, less than 2% of the spots were missing or saturated within the defined pupil of the SHWS, and were thus likely to produce negligible error in wavefront estimation [Sec. 6.8.1].

6.8.3 Sample of Artificial Collagen

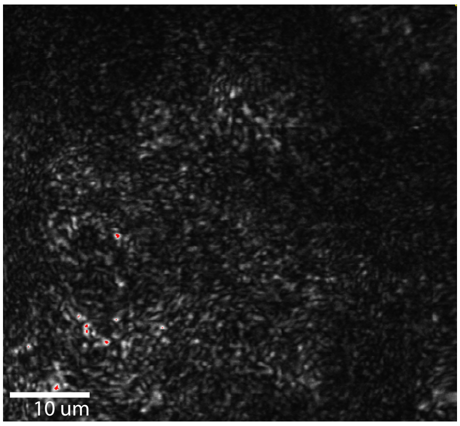

Figure 6.26: Confocal image of a sample of artificial collagen.

A sample of artificially created collagen was placed between a glass slide and a coverslip with water as the immersion medium. Given the strand-like structure of collagen, it acts as a good 3D scattering specimen. A confocal image is shown in Fig. 6.26. Averaging was accomplished by setting the exposure of the SHWS to 35ms. Averaging was achieved by taking 5 successive images when using the 300μm and 600μm pinholes, and 15 images when using the 200μm pinhole.

Fig. 6.27 shows the response of the SHWS to even aberrations induced by the DM,

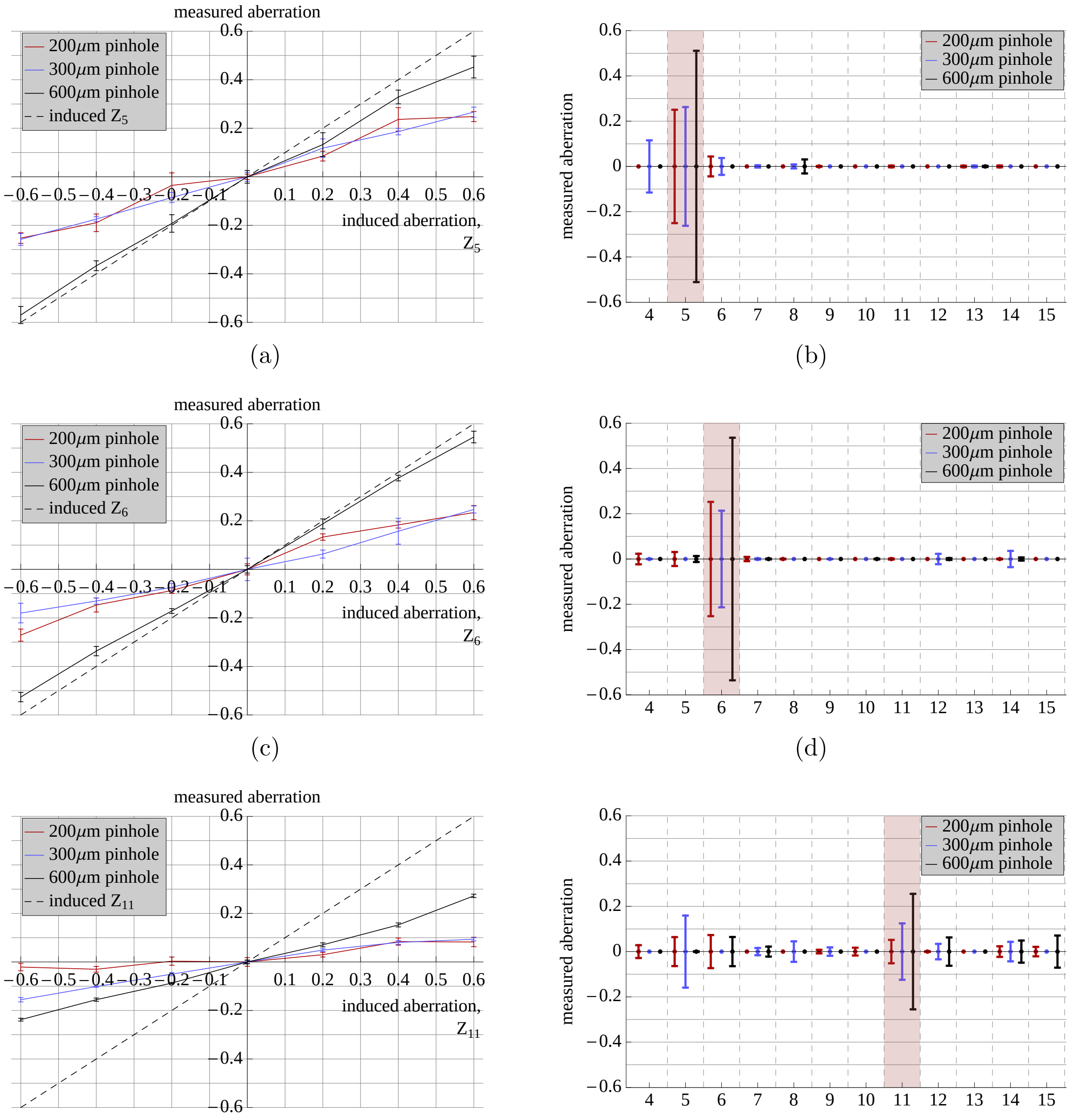

(a) (b)

(c) (d)

(e) (f)

Figure 6.27: SHWS measurements of even aberration modes Z_5, Z_6 and Z_{11}, respectively, which were induced by a DM and scattered back by a sample of collagen in water. (a), (c) and (e) Measured aberration as a function of induced aberration. (b), (d) and (f) Maximum measured amplitude of all Zernike modes, showing cross-talk between modes. The DM-induced Zernike modes are highlighted in the graphs.

and Fig. 6.28 and Fig. 6.29 show those for the odd aberrations. Looking at the graphs in the left column that illustrate measured aberration as a function of induced aberration, a linear relationship was obtained. The measurements with the 200μm and 300μm pinholes were very similar.

Analysing the graphs showing the maximum measured amplitudes of all Zernike

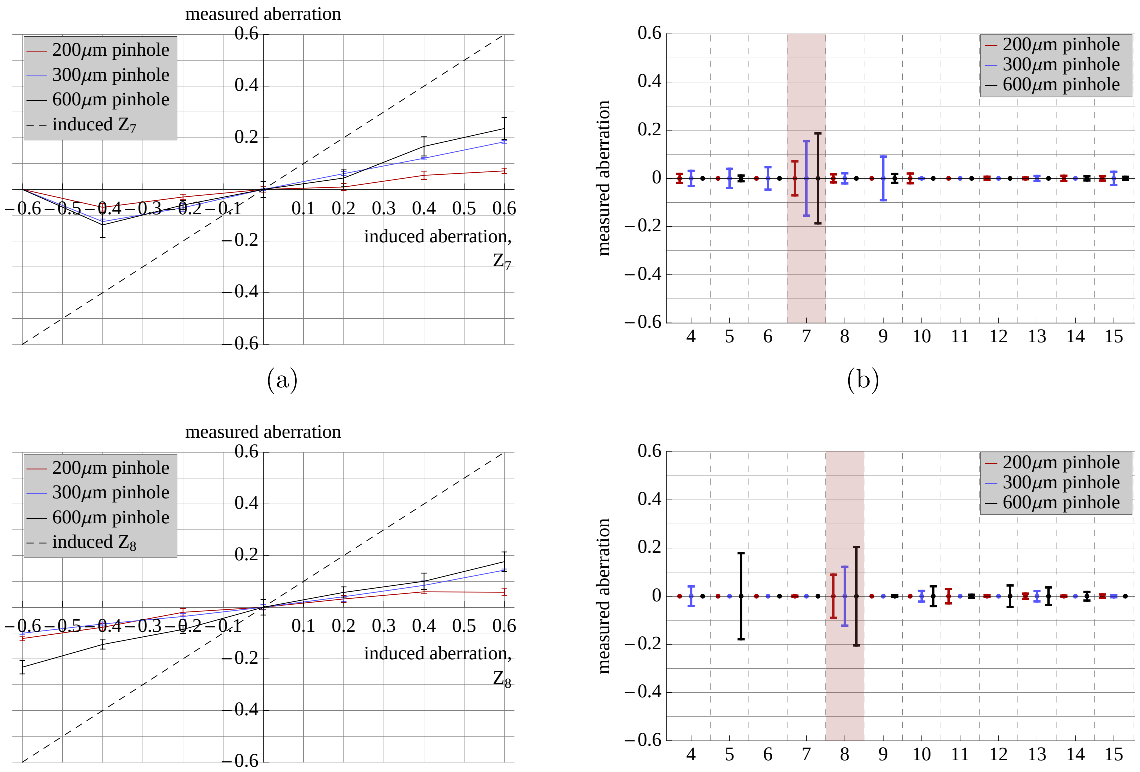

(a) (b)

(c) (d)

Figure 6.28: SHWS measurements of the odd aberration modes Z_7 and Z_8 (comas), respectively, which were induced by a DM and scattered back by a sample of collagen in water. (a) and (c) Measured aberration as a function of induced aberration. (b) and (d) Maximum measured amplitude of all Zernike modes, showing cross-talk between modes. The DM-induced Zernike modes are highlighted in the graphs.

modes, significant cross-talk was noted for the detection of Z_{11}, reasons for which are given in Sec. 6.8.1 and Sec. 6.8.2. Considerable cross-talk was also observed for Z_8 and Z_9.

From Fig. 6.30, showing the percentages of the induced aberrations measured, it can be seen that a higher proportion of both even and odd aberrations were detected with the collagen sample compared with the 200nm bead sample, shown in Fig. 6.25. This could be caused due to the better homogeneity of scattering from the collagen sample and the different sized scatterers. This shows that the measurement of aberrations depends on the structure of the specimens. Almost two-fold increase in the estimation was observed with the 600μm pinhole than with the 200μm and 300μm pinholes. Using the 600μm pinhole, almost 90% of the astigmatisms were detected, and the trefoils were detected at 50 – 60% of the induced aberrations. Yet again a lower ratio of the comas and the

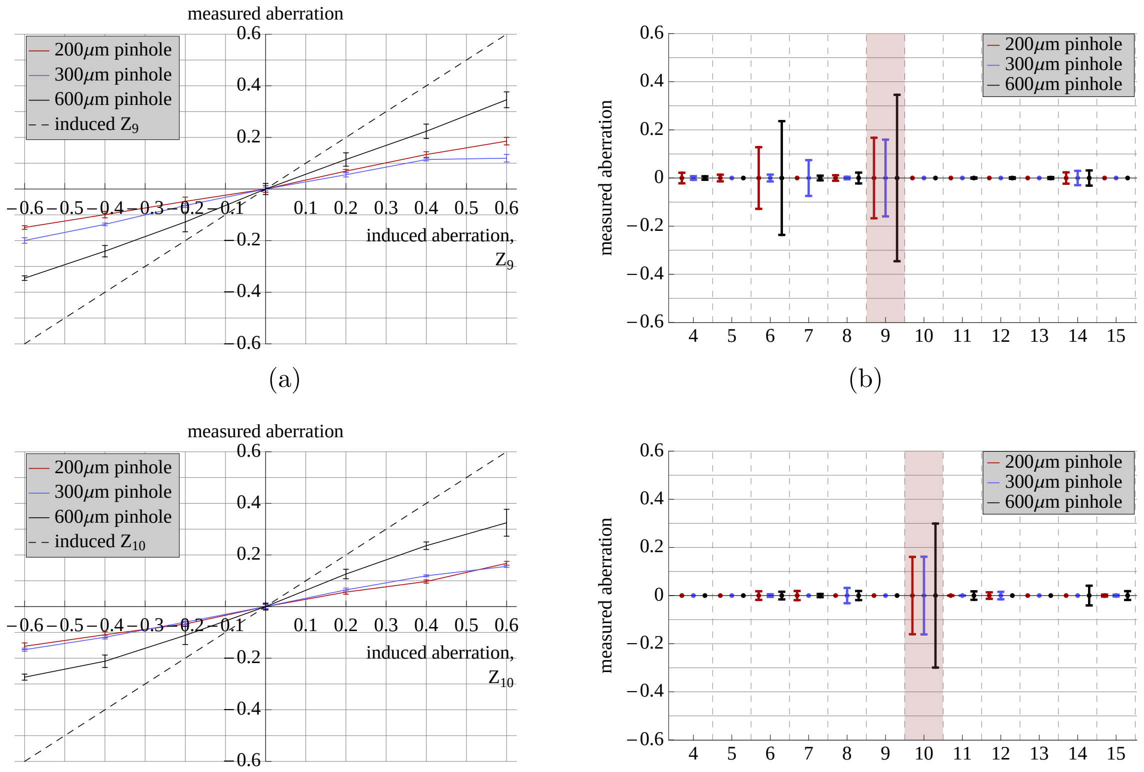

(a) (b) (c) (d)

Figure 6.29: SHWS measurements of the odd aberration modes Z_9 and Z_{10} (trefoils), respectively, which were induced by a DM and scattered back by a sample of collagen in water. (a) and (c) Measured aberration as a function of induced aberration. (b) and (d) Maximum measured amplitude of all Zernike modes, showing cross-talk between modes. The DM-induced Zernike modes are highlighted in the graphs.

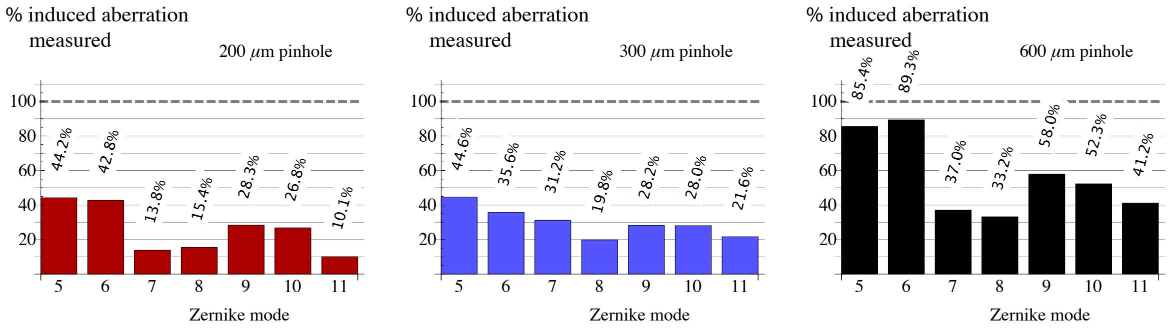

(a) (b) (c)

Figure 6.30: Bar charts showing the percentages of induced aberrations detected by the SHWS from light backscattered from a sample of collagen using (a) 200μm, (b) 300μm and (c) 600μm WS pinhole.

spherical aberration were detected, standing at around 40%, which is double the amount detected with the 200nm beads sample.

From the error bars in the preceding graphs, the readings using the 200μm and

300μm pinholes each had one maximum standard deviation of ±0.05 radian for measurements of Z_5 and Z_6, respectively. Otherwise, all the readings were consisting to within a standard deviation of ±0.02 radian. The readings using the 600μm pinhole showed a few high standard deviations of ±0.05 radian. Although higher proportions of the aberrations were measured for the collagen sample compared to the 200nm beads sample, the error margin also appeared to be larger. The averaging of 15 images did not appear to reduce the error when using the 200μm pinhole, but a smoother intensity was obtained in the pupil, whereby no spots were missing or saturated. For the 300μm and 600μm pinholes, less than 2% of the spots were missing or saturated within the defined pupil of the SHWS, and so were likely to produce negligible error in wavefront estimation [Sec. 6.8.1].

6.9 Limitations of the System

6.9.1 Dependence on Specimen Structure

Comparing the results for the sample of 200nm polystyrene beads [Sec. 6.8.2] and the sample of collagen [Sec. 6.8.3], it is quite apparent that the specimen structure plays a big role in the detection of aberrations in a dual-pass wavefront sensing system. However, if a specimen consists of large elements, at the centre, an element may reflect light as a specular surface, and at the edges, scatter the light. So to test the behaviour under such circumstances, a model specimen was created using larger glass beads ranging 3 – 10μm in diameter. A sample of suitable density was obtained in similar fashion to the 200nm beads sample [Sec. 6.8.2]. The beads were allowed to dry on a glass slide so as to yield a 2D scattering surface of beads. A 2D sample was created since the response of the system to larger features was of interest rather than testing out the capability axial selectivity of the pinhole, and as it was a simpler process than drying the beads in gelatine. Once the beads settled on the glass slide, the sample was immersed in oil of refractive index 1.32, similar to that of water, and a coverslip was then placed on top and sealed. Aberrations were estimated by the SHWS while the specimen was scanned. Image averaging was performed by taking 5 consecutive frames and coefficient averaging via 5 measurements.

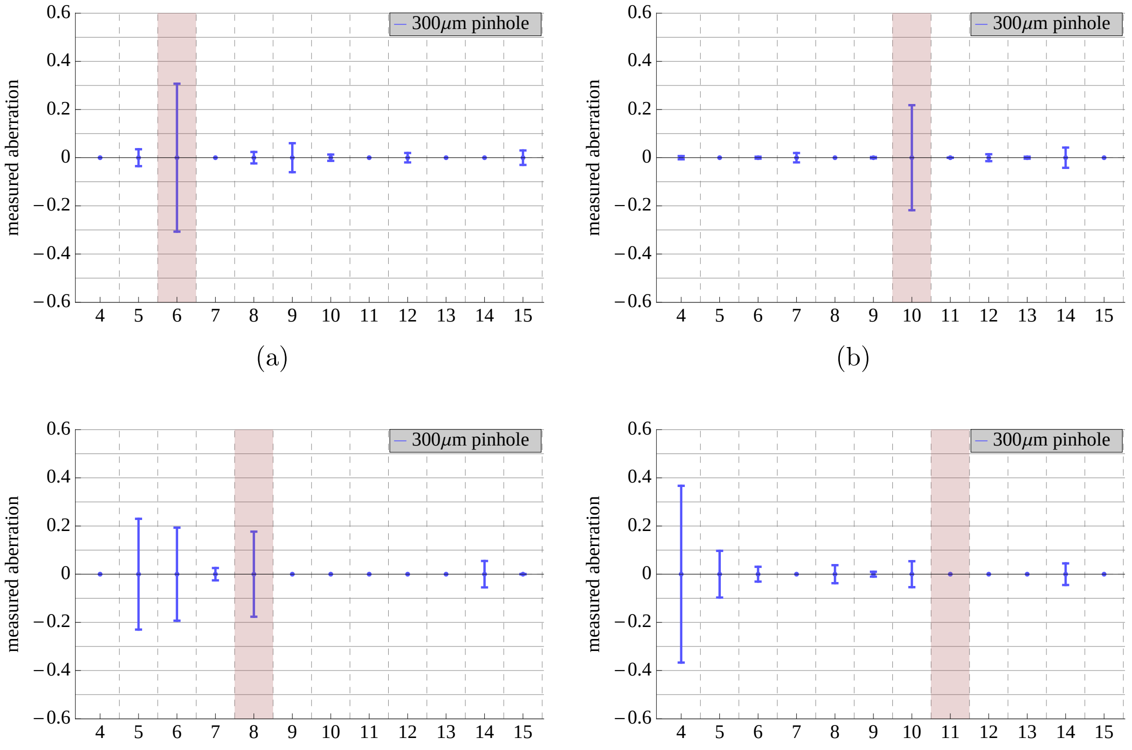

(a) (b)

(c) (d)

Figure 6.31: SHWS measurements of the aberration modes (a) Z_6, (b) Z_{10}, (c) Z_8 and (d) Z_{11}, which were induced by a DM and scattered back by a sample of large $3-10\mu$m beads. Graphs show maximum measured amplitude of all Zernike modes, showing cross-talk between modes. The DM-induced Zernike modes are highlighted in the graphs.

Experimentally, using a 300μm pinhole for axial selectivity, it was seen that some modes were detected very well. For example, as Fig. 6.31a and Fig. 6.31b show, the SHWS detected about 50% of the induced Z_6 and 40% of Z_{10} with negligible inaccurate estimation of other Zernike modes. However, some modes were detected very poorly. As Fig. 6.31c shows, although the SHWS estimated around 30% of the induced Z_8, it estimated a higher proportion of Z_5 and Z_6. Also as Fig. 6.31d shows, the SHWS completely failed to detect Z_{11} when it was induced, which was predominantly mistaken as Z_4.

Fig. 6.32 shows the percentages of induced aberrations detected by the SHWS from a sample of 100nm gold beads suspended in gelatine using 300μm and 600μm pinholes. The sample was created in the same manner as the 200nm polystyrene beads [Sec. 6.8.2]. Gold

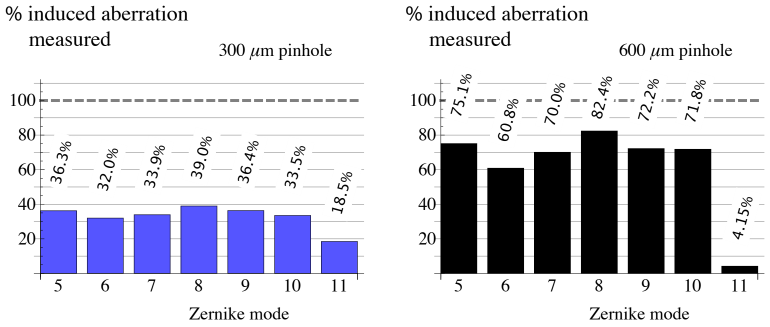

(a) (b)

Figure 6.32: Bar charts showing the percentages of induced aberrations detected by the SHWS from light backscattered from a sample of 100nm gold beads suspended in gelatine using (a) 300μm and (b) 600μm WS pinhole. The DM-induced Zernike modes are highlighted in the graphs.

being highly reflective, the sample seemingly provided very different results compared to the 200nm beads and collagen samples that were discussed in Sec. 6.8.2 and Sec. 6.8.3, respectively. It appears that both even and odd aberrations, Z_{11} aside, were detected at equal amounts, and the detection almost doubled from the use of a 300μm to a 600μm pinhole.

6.9.2 Dependence on Optics

The measurement of aberrations in the dual-pass system could vary depending on the hardware used. Instead of the 63× Zeiss 1.2NA water immersion lens, a 40× Zeiss 1.3NA oil immersion lens was used to carry out the experiments on the 200nm beads sample, and a Cobalt-Calypso laser source was used generating light of wavelength 491nm. Consequently, an aberration-free Airy disc of approximate diameter 461nm was produced, calculated using Eq. (2.41), which compares to the 644nm diameter of the aberration-free Airy disc of the system in the preceding experiments. Being just over double the diameter of the 200nm beads, the beads appeared at point scatterers in the system.

Fig. 6.33 compares the proportions of the induced aberrations detected by the SHWS for the different settings. It was found that nearly 100% of the induced astigmatisms were detected compared to only around 40% for the set-up used in the previous experiments.

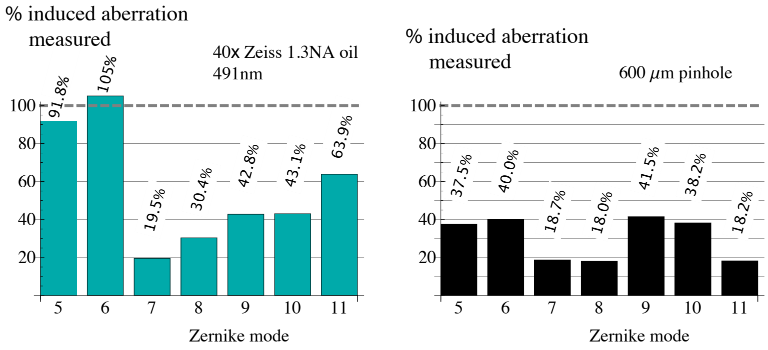

(a) (b)

Figure 6.33: Bar chart showing the ratio of measured to induced aberrations detected by the SHWS from light backscattered from a sample of 200nm beads using a 600μm WS pinhole. (a) Laser source emitting light of wavelength 491nm and a 40× Zeiss 1.3NA oil immersion lens were used. (c) Light of wavelength 633nm and a 63× Zeiss 1.2NA water immersion lens were used.

The detection of Z_{11} also increased from about 20% to 64%. The detection of coma and trefoil appeared to have been steady between 20% and 40%, respectively, as also observed in Fig. 6.33b. The increase in the detection of the even aberration modes may have occurred since the focal spot had become smaller and the scatterers thus appeared larger than in the set-up in Sec. 6.8.2. Consequently, specular reflections may have increased slightly, yielding the higher portions of even mode measurements. The difference in the measurements may also have occurred as a consequence of imaging a different region of the specimen that exhibited more specularity owing to a denser concentration of beads [Sec 6.2.3].

These results indicate that the estimation of aberrations from backscattered light could be dependent on several other factors besides specimen structure, such as, the objective lens and mounting medium.

6.10 Conclusions

The simulations and experimental results showed how the phase of backscattered light, and consequently the detection of aberrations, was affected by the dual-pass nature of the microscope system. Even aberrations add up and odd aberrations cancel out when using a specular specimen. For a single scatterer, the phase is correctly determined as only the aberrations in the detection path are detected [Sec. 6.2]. For specimens with an intermediate degree of scattering, the measured aberrations cannot be determined unambiguously.

The experimental results showed that the detection of aberrations could vary greatly from specimen to specimen. This was predicted in the theoretical simulations presented in Sec. 6.2, particularly by Eq. (6.13) through to Eq. (6.18). The nature of scattering and reflection depends upon many factors that include the size and refractive indices of the scattering features, the size of the focal spot that is governed by the illumination wavelength and the objective lens, and refractive index of the mounting medium. Aberration measurement from backscattered light also depends on these aforementioned factors, as the experiments in the previous sections show.

Averaging of frames via long exposures of the SHWS and multiple frames has allowed for uniform Hartmann spot patterns to be obtained. The axial selectivity pinhole allowed the estimation of aberrations from the focal plane by rejecting out-of-focus light. It was shown that the maximum phase gradient allowed to pass through a pinhole is directly proportional to the pinhole radius. Furthermore, the pinhole has a smoothing effect on the wavefront phase. As such, measurements using smaller pinholes yielded greater estimation error as a direct consequence of filtering out rays that deviated more due to aberrations, and due to smoothing. However, larger pinholes will allow too much light through, resulting in multiple spots registering on the SHWS. Therefore a suitable compromise has to be made. The optimum size for the pinhole depends of various other factors that govern the size of the focal spot being filtered and the size of the aberrations.

A linear response to the estimation of aberrations against the induced aberrations was achieved for a given experimental configuration and scattering specimen. The data also showed small standard deviations, suggesting good repeatability of the measurements. Although these data are not ideal for direct quantitative measurement of aberrations, they may be useful as feedback in a closed-loop adaptive correction system.

Realistically, specimens may include features that vary greatly in size, which may not appear as point scatterers to the system like the model specimens used earlier. In such cases, the system may fail to detect the correct phase altogether.

Chapter 7

Direct Wavefront Sensing using Asymmetric Illumination and Detection

Ch. 6 showed how the specular component affected aberration measurements in a dual-pass system. Subsequently, it can be assumed that the scattered component should provide a more accurate representation of the aberrations. Hence, it is desirable to use a method where the WS only measures the scattered light.

This chapter introduces a method by which predominantly the aberrations in the detection path could be detected by restricting the beam width in the illumination path, hence reducing the illumination NA. Backscattered light causes high NA detection, hence creating a system of asymmetric illumination and detection using the same high NA objective lens. This asymmetric dual-pass method has been shown in ophthalmic research of the human eye to produce better readings of both even and odd aberration modes [42, 77].

7.1 Asymmetric Illumination and Detection

Fig. 7.1a shows an illumination beam of restricted width entering the back aperture of a high NA objective lens. Looking at the close up of the focal region, shown in Fig. 7.1b, the illumination beam passes through a very narrow region of the scattering specimen. For smoothly varying aberrations, the phase variation across the narrow beam will be small. Although the beam may therefore pick up a constant phase shift, this will not be detected by the WS. The specimen causes light to scatter back in all directions. The backscattered light is aberrated by the specimen. The light that falls within the focal cone of the high NA objective lens is collected and forms the high NA detection. As a result, the dual-pass phenomenon detailed in Ch. 6 can be avoided and, in theory, a higher proportion of the odd aberrations can be detected.

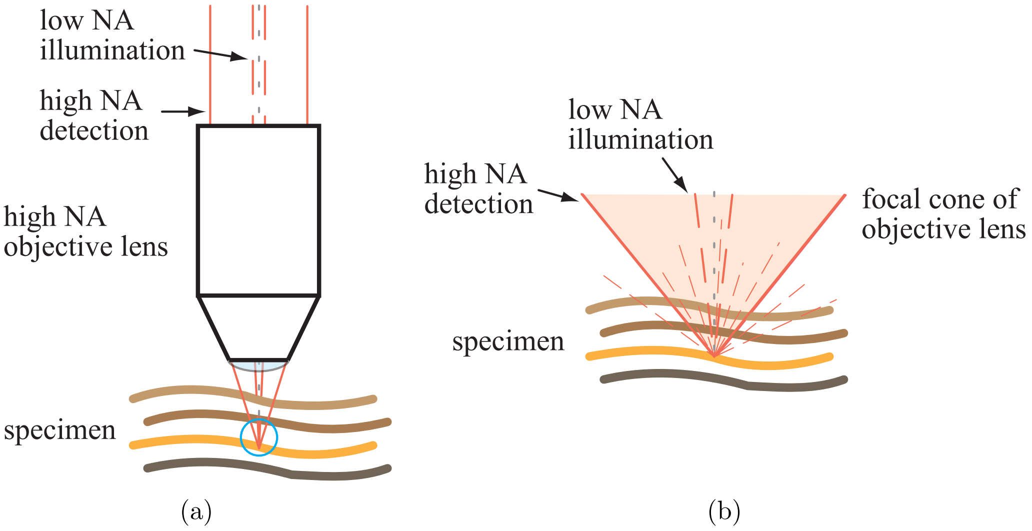

Figure 7.1: Effect of asymmetric illumination and detection on aberrations. (a) Low NA illumination is attained by reducing beam width and high NA detection is achieved due to scattering of light. (b) Closer look at asymmetric illumination and detection of region circled in (a). Light is focussed through a small region of the specimen and is negligibly affected by specimen-induced aberrations. Light is scattered back in all directions and aberrated, and those lying within the focal cone of the high NA objective form high NA detection.

Assuming a narrow beam of light, the pupil function P_1 can be modelled by the Dirac delta function. Substituting the assumption for the illumination pupil function into Eq. 6.16, the field in the entrance pupil of the WS for the asymmetric dual-pass system reduces to:

$$\bar{U}_5 = \left[(\delta \otimes O_s)\tilde{P}_1\right] \otimes \mathcal{F}\left\{d\right\} = O_s\tilde{P}_1 \otimes \mathcal{F}\left\{d\right\}. \tag{7.1}$$

Therefore, it is expected that the wavefront phase measurements will be dominated by the detection pupil function and the specimen structure, smoothed by the effect of the axial selectivity pinhole.

7.2 Experimental Design

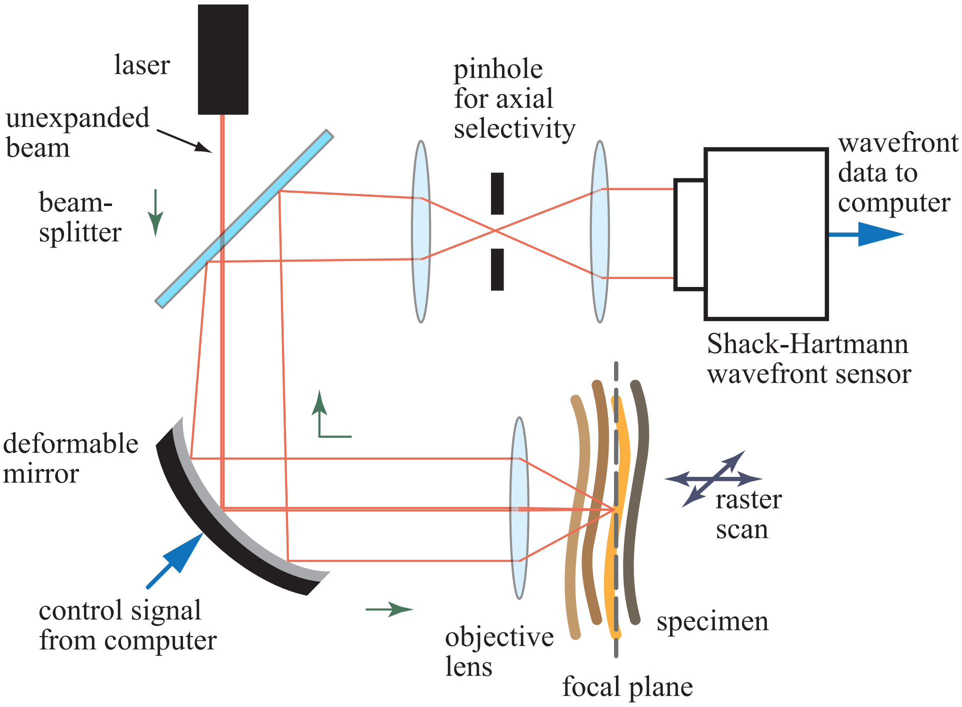

Figure 7.2: Simple schematic of a dual-pass wavefront sensing system with asymmetric illumination and detection. Light from laser is not expanded, leading to low NA illumination of the specimen. Scattering from the specimen leads to high NA detection. Some optical elements have been omitted for clarity.

Fig. 7.2 shows a simplified schematic of the experimental set-up modified from the set-up shown in Fig. 6.10. The pair of lenses expanding the light from the laser were removed to attain a beam of diameter approximately 800μm wide, which was reflected from the centre of the DM. As the light impinged a very small area of the DM in the illumination path, it was assumed to be unaffected by the aberrations of the DM. The next pair of 4f lenses (not shown in the diagram for simplification) de-magnified the beam further down to a diameter of 457μm, which was focussed by the objective lens into the specimen. The width of the beam reduced the effective NA of the lens in the illumination path from 1.2 to approximately 0.096. As explained in the previous section and Sec. 4.2.1, since the light now passed through a very small region within the specimen while being focussed through it, it was expected to be negligibly affected by specimen-induced aberrations in comparison to the expanded beam used in Sec. 6.6. Light scattered back from the focal plane within the specimen was aberrated in the detection path. The backscattered light that populated the focal cone of the objective lens filled the pupil of the objective lens, ensuring detection at the full NA of 1.2. Any specular component of the scattering will occupy the same small NA as the illumination. It should therefore be possible to separate to some degree the specular effects from the pure scattering effects. Subsequently, asymmetric illumination and detection was established, and only specimen-induced aberrations from the detection path were expected to be detected by the SHWS.

Since only aberrations in the detection path should be detected, it was expected that lower proportions of even aberration modes will be detected since phase should not add up. Contrastingly, higher proportions of odd aberration modes should be detected since phase should not cancel out.

7.3 Experimental Results

The experiments were conducted as outlined in Sec. 6.6.1. Aberrations were induced using the DM and the estimated aberrations detected by the SHWS were recorded for analysis. The following sections discuss the results from various scattering specimens.

7.3.1 Sample of 200nm Beads Suspended in Gelatine

The model scattering specimen of 200nm polystyrene beads suspended in gelatine, a 2D confocal image of which is shown in Fig. 6.19, was used to study the aberration detection capabilities of the asymmetric illumination and detection dual-pass system. The diameter of the aberration-free Airy disc produced by the 63× Zeiss 1.2NA water immersion lens was calculated to be approximately 8.05μm, applying the effective illumination NA of 0.096 in Eq. (2.41). The focal spot was, therefore, clearly much larger than the beads that should behave approximately like point scatterers. The reduction of the NA also implied that the axial width of the first zero of the focal spot increased from 1.76μm to approximately 275μm, as calculated using Eq. (2.43), but the scattered light was filtered out by the pinhole.

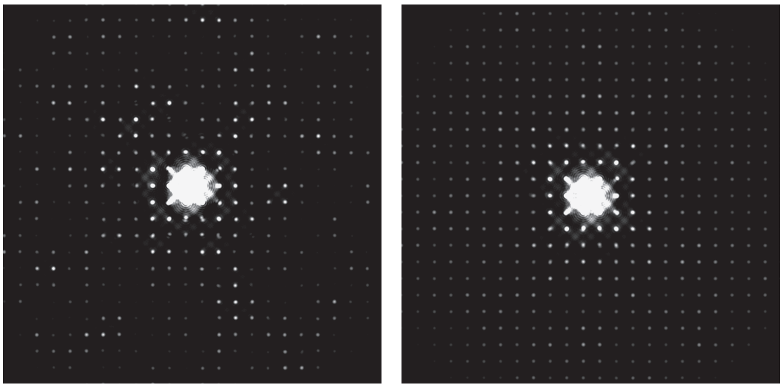

(a) (b)

Figure 7.3: Sample Hartmann spot patterns from light backscattered from a sample of 200nm beads suspended in gelatine. A 600μm pinhole was used for axial selectivity. The bright spot in the middle of the aperture resulted from direct reflection of the low NA illumination beam. (a) The specimen was stationary. Backscattered light filled up rest of the aperture. (b) The specimen was scanned and image was averaged to achieve a uniform spot pattern.

Fig. 7.3a shows the Hartmann spot pattern observed on the SHWS from light backscattered from the stationary bead specimen. Axial selectivity was achieved using a 600μm pinhole. A scattered non-uniform spot pattern was observed where spots were missing. A bright central spot was formed that arose from direct reflection of the low NA illumination. The high intensity of light confined to a small focal cone due to the reduced beam width was reflected back from the coverslip, glass slide and the specimen. A portion of the illuminating light was scattered back by the specimen in all directions. The rest of the aperture of the SHWS was filled by the backscattered light that fell within the focal cone of the objective lens in the detection path. A uniform pattern was established by averaging consecutive frames at a suitable exposure of the sensor while the specimen was scanned [Sec. 6.6.1], which is shown in Fig. 7.3b.

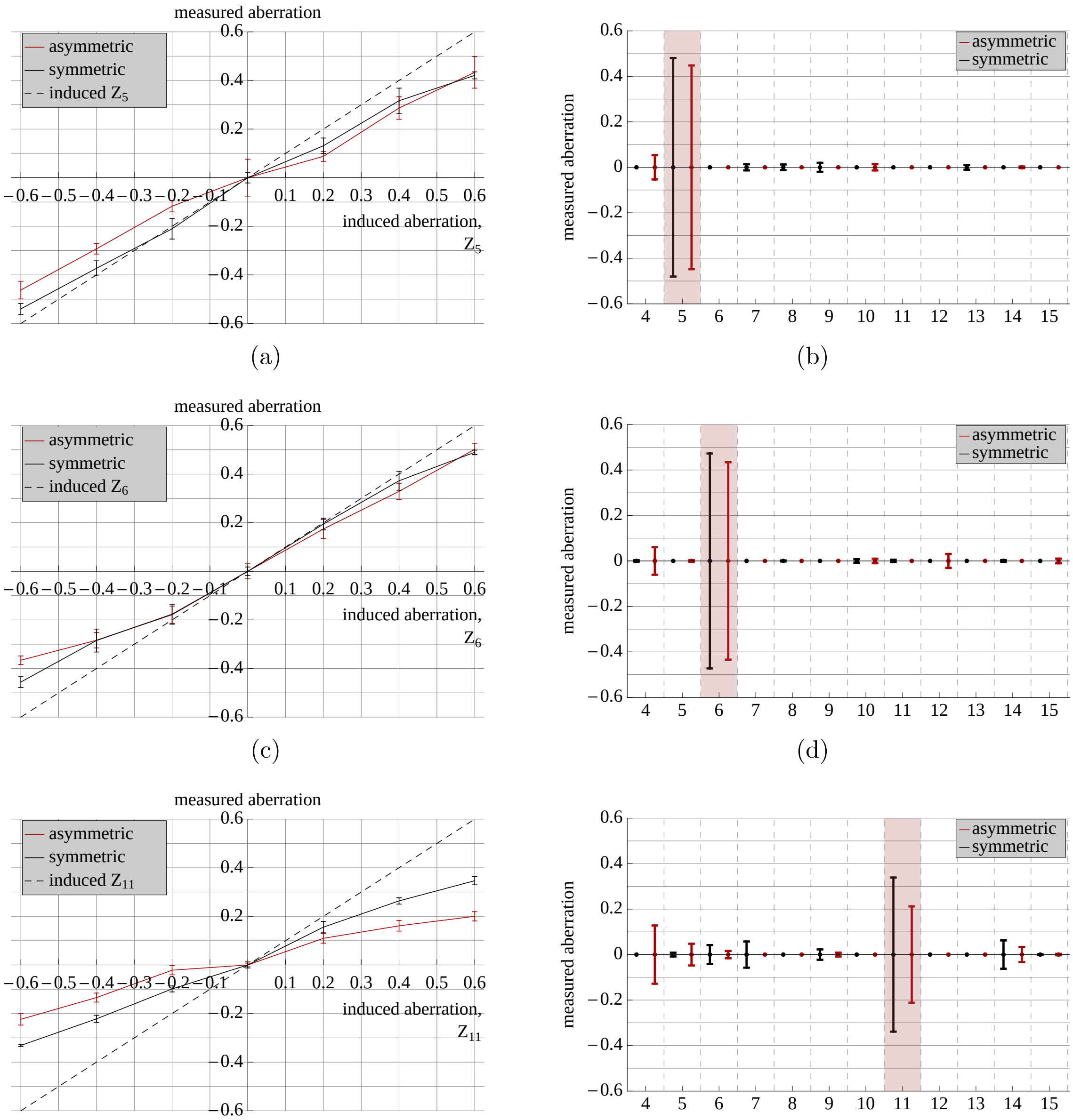

(a) (b)

(c) (d)

(e) (f)

Figure 7.4: SHWS measurements of even aberration modes Z_5, Z_6 and Z_{11}, respectively, which were induced by a DM and scattered back by a sample of 200nm beads suspended in gelatine. Asymmetric illumination was used and compared with the results from the symmetric set-up. (a), (c) and (e) Measured aberration as a function of induced aberration. (b), (d) and (f) Maximum measured amplitude of all Zernike modes, showing cross-talk between modes. The DM-induced Zernike modes are highlighted in the graphs.

Fig. 7.4 shows the SHWS measurements for the even aberration modes of astigmatism, Z_5 and Z_6, and spherical, Z_{11}. The measurements were repeated for the same specimen in the symmetric set-up of Fig. 6.10, shown in black, and asymmetric set-up of Fig. 7.2, shown in red. The amount of DM-induced aberration is shown by the dashed line in the graphs.

The experiments were performed using a 300μm pinhole for axial selectivity and at a sensor exposure of 67ms for both set-ups. 5 consecutive frames were averaged for each measurement and 5 measurements were taken for each Zernike mode amplitude induced using the DM.

The graphs show that the measurements of the astigmatisms, Z_5 and Z_6, from backscattered light were similar for both the set-ups. A difference in the proportions of readings can be observed when comparing with the results in Fig. 6.21 for the symmetric dual-pass system using a 300μm pinhole. This is due to the variability in the measurements already discussed arising from probing different regions in a specimen, or a different specimen [Sec. 6.9.1].

With the asymmetric illumination, around 7% of the spots were discarded as they saturated the sensor in the centre. Therefore, around $35 - 40$ spots were recognised as undeviated by the software out of the 540 spots used for wavefront estimation within the circular pupil, forcing the algorithm to estimate the phase gradient as zero in that central region. Effectively, the phase is clipped or flattened in the saturated centre. Consequently, the wavefront estimation was more prone to errors due to this systematic error. The asymmetric system also gave rise to slightly larger error bars compared to the corresponding symmetric system measurements. The maximum standard deviation for the symmetric set-up was observed, for example, for Z_5 at ±0.05 radian and correspondingly for the asymmetric set-up it was about ±0.08 radian. Comparable cross-talk of modes was observed between the measurements of both the systems.

A smaller proportion of Z_{11} was detected in the asymmetric set-up. Fig. 7.4f shows that in the asymmetric set-up, the SHWS estimated around ±0.12 radian of Z_4 against ±0.2 radian of Z_{11} when ±0.6 radian of Z_{11} was induced by the DM. This may have arisen due to the systematic error from the saturation. Referring back to Fig. 6.17, the cross-section of the phase distribution of Z_{11} shows a non-zero phase at the centre of the pupil and a higher phase gradient compared to the astigmatisms. The estimated

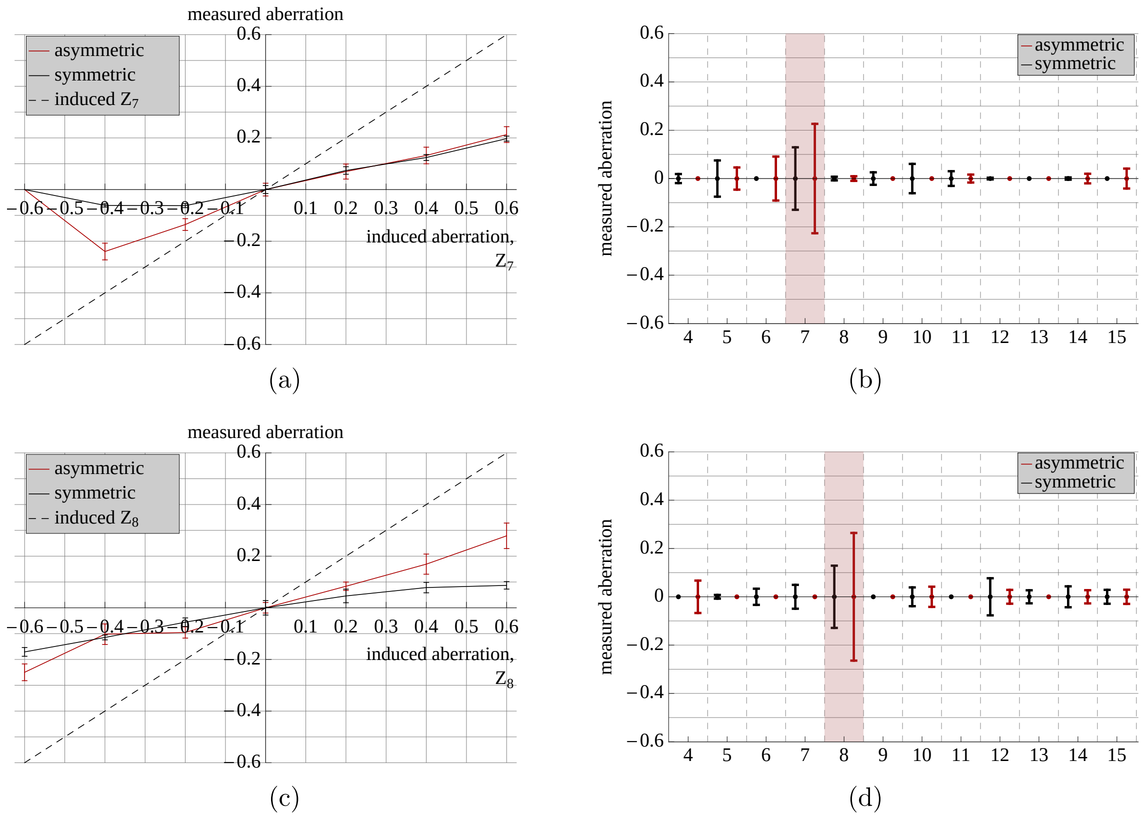

(a) (b) (c) (d)

Figure 7.5: SHWS measurements of the odd aberration modes Z_7 and Z_8 (comas), respectively, which were induced by a DM and scattered back by a sample of 200nm beads suspended in gelatine. Asymmetric illumination was used and compared with the results from the symmetric set-up. (a) and (c) Measured aberration as a function of induced aberration. (b) and (d) Maximum measured amplitude of all Zernike modes, showing cross-talk between modes. The DM-induced Zernike modes are highlighted in the graphs.

phase for Z_{11} was flattened at the centre due to saturation as the algorithm set the phase gradients for these spots to zero, whereas, the phase distributions of the astigmatisms are already flatter at the centre. The axial selectivity pinhole has already been established to cut-off the high frequency components of Z_{11} owing to the higher phase gradient of the mode [Sec. 6.8.1], which along with the 7% discarded spots due to saturation, caused the estimation error of Z_{11} in the asymmetric system.

Fig. 7.5 and Fig. 7.6 show the measurements of the odd aberrations coma and trefoil, respectively. As expected, the measured aberrations were slightly higher in the asymmetric set-up since the odd aberration phase did not cancel out. The standard deviation was still higher compared to the symmetric set-up, and cross-talk between modes was found to be in similar range.

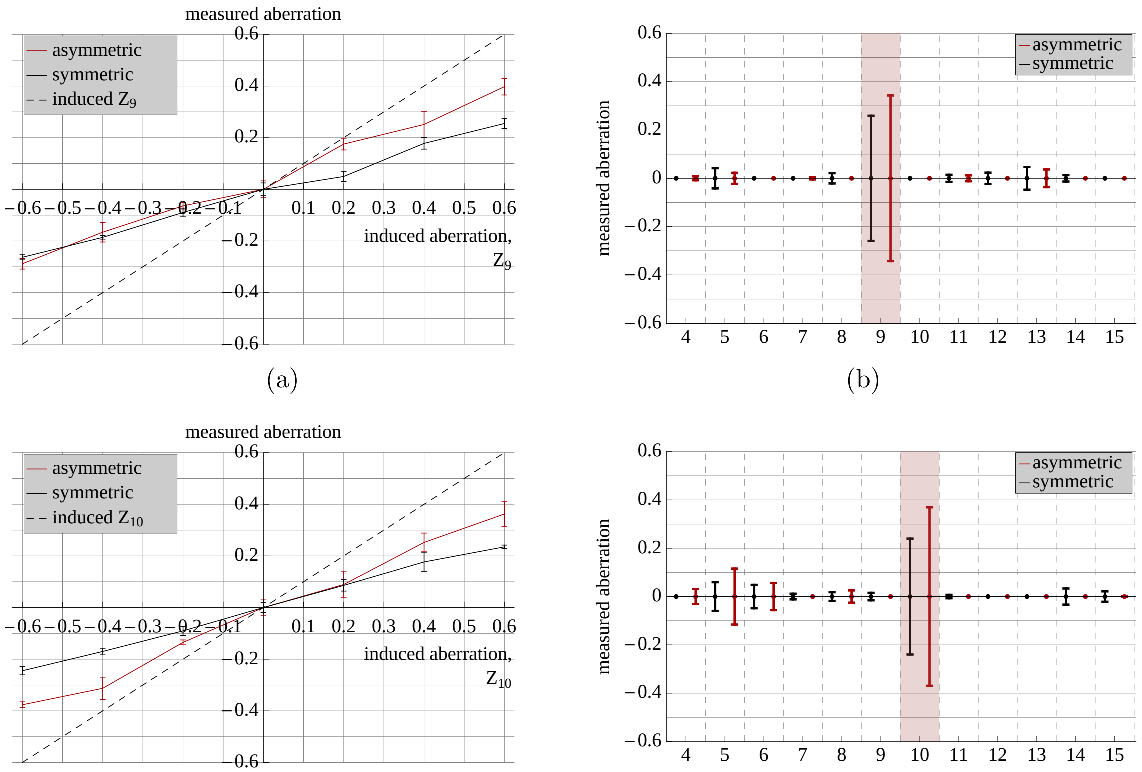

(a) (b)

(c) (d)

Figure 7.6: SHWS measurements of the odd aberration modes Z_9 and Z_{10} (trefoils), respectively, which were induced by a DM and scattered back by a sample of 200nm beads suspended in gelatine. Asymmetric illumination was used and compared with the results from the symmetric set-up. (a) and (c) Measured aberration as a function of induced aberration. (b) and (d) Maximum measured amplitude of all Zernike modes, showing cross-talk between modes. The DM-induced Zernike modes are highlighted in the graphs.

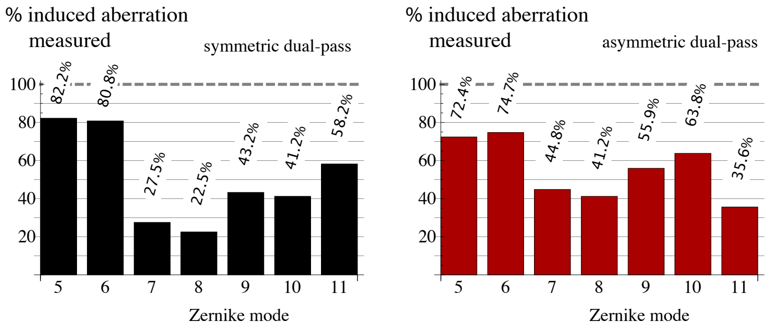

(a) (b)

Figure 7.7: Bar charts showing the percentages of induced aberrations detected by the SHWS from light backscattered from a sample of 200nm beads using (a) symmetric and (b) asymmetric illumination.

Fig. 7.7 shows the percentages of the induced aberrations detected by the SHWS and summarises what was noted from the preceding graphs. The detection of the coma modes, Z_7 and Z_8, increased by a factor of approximately 1.7 for the beads specimen when using asymmetric as opposed to symmetric illumination and detection. A slight increase was also observed for the trefoil modes, Z_9 and Z_{10}. Detection of Z_{11} reduced by a factor of 1.6 due to saturation of the sensor.

7.3.2 Sample of Artificial Collagen

The response of the SHWS to backscattered light in the asymmetric illumination and detection set-up was tested with the sample of artificial collagen. As with the beads specimen, results from the symmetric and asymmetric set-ups are compared. The experiments were undertaken using a 300μm pinhole for axial selectivity. The exposure time of the SHWS was set to 67ms with 5 frame averaging for both set-ups. 5 measurements were taken for each induced amplitude of Zernike modes.

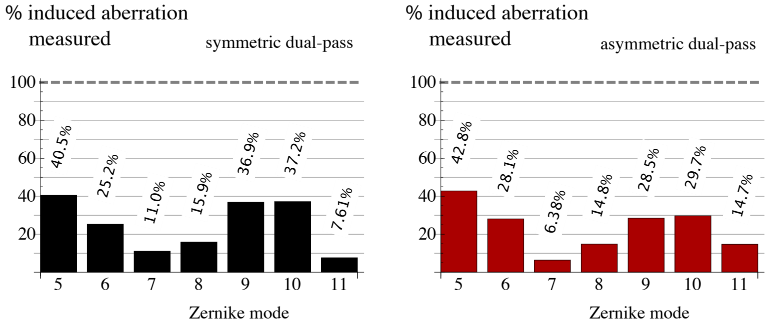

(a) (b)

Figure 7.8: Bar charts showing the percentages of induced aberrations detected by the SHWS from light backscattered from a sample of collagen using (a) symmetric and (b) asymmetric illumination.

Fig. 7.8 summarises the experimental findings by comparing the proportions of each induced Zernike mode detected by the SHWS. Clearly, the asymmetric set-up had less impact on the structure of collagen than on the beads sample. The proportions of the measured modes were noted to be similar for both the symmetric and asymmetric set-ups. However, the results for the collagen specimen showed that a higher proportion of Z_{11} was detected using the asymmetric set-up.

These results further show the dependence on specimen structure when detecting aberrations from backscattered light using direct wavefront sensing. Once again, the variability of the measurements can be noted by comparing Fig. 6.30b and Fig. 7.8a. The data from the symmetric set-ups show a marked difference in the proportions of Zernike aberration modes detected arising from scanning the specimen in a different region.

7.4 Conclusions

The results provided in this chapter showed that the asymmetric dual-pass set-up may provide better detection of odd aberration modes, over the symmetric set-up, depending on the specimen structure. For example, detection of the coma modes were almost doubled for the 200nm beads specimen [Sec. 7.3.1], whereas insignificant difference was observed for collagen [Sec. 7.3.2].

Using the asymmetric set-up resulted in saturation of the SHWS in the centre of the aperture, and consequently error in estimation had increased. The current algorithm forced the phase gradient to zero in the saturated region, hence flattening the phase. This could have a significant impact on the detection of higher-order aberration modes, and spherical aberration modes in particular, that have non-zero phase and higher phase gradients at the centre of the pupil. A more robust algorithm could perhaps leave the displacement of the saturated spots as free variables and extrapolate their values from the other phase gradient measurements.

Chapter 8

Effects of Polarisation Filtering in Direct Wavefront Sensing of Backscattered Light

In this chapter, a further method is investigated that may help avoid the dual-pass phenomenon of the symmetric dual-pass optical system. The odd aberration phase cancellation in a dual-pass set-up occurs due to specular reflections from a specimen [Sec. 6.2.2]. Therefore, if the specular component of backscattered light can be filtered out, the the odd aberration phase cancellation will be suppressed. This chapter introduces a technique by which specular reflections can be filtered out using polarisation optics.

8.1 Effects of Polarisation Filtering

Polarisation microscopy is often used to retrieve images where the generated contrast sheds useful information on specimen birefringence and dichroism. Any optical system can be converted to a polarisation instrument using crossed polarisers — a polariser is inserted in the illumination path and an analyser in the detection path. The polariser in the illumination path linearly polarises the light in one particular direction, for example, in x,

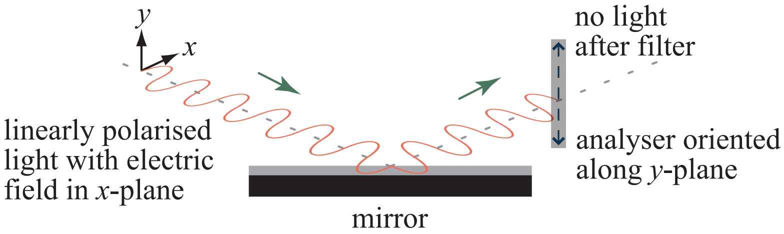

Figure 8.1: Linearly polarised light with electric field vibrating along the x-plane retains its polarisation after reflection. The polarisation analyser is oriented to allow light linearly polarised along the y-plane completely filters out the incoming light.

and the polarised light probes the specimen. The analyser is simply another polariser that is oriented to allow only light of polarisation orthogonal to that of the illumination beam to pass through. The polarisation contrast occurs due to modification of the polarised illumination by the intrinsic optical properties of the features being probed.

Fig. 8.1 shows the electric field of a linearly polarised light. Upon reflection off a specular surface, such as a mirror, the light retains its polarisation. As such, the light is completely cut off after transmission by an analyser placed in the path of the reflected light.

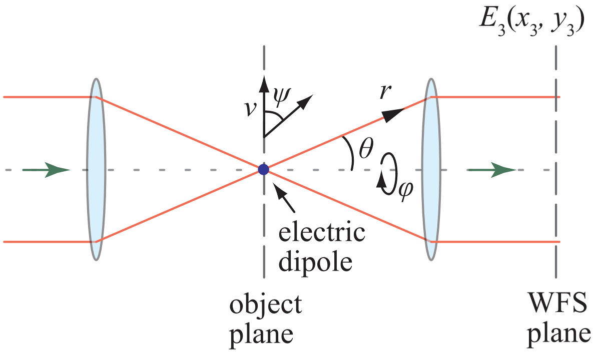

Figure 8.2: Definition of spherical polar coordinates (r, θ, φ) for the Debye vectorial theory. (v, ψ) represent the polar scanning coordinates in the object plane.

Contrastingly, light becomes partially depolarised after scattering. When sub-resolution structures are probed, the polarisation contrast occurs due to the scattering properties of the structures [78]. If the scatterers are assumed to be sub-resolution dielectric scatterers, then the scattered far field is identical to that produced by an electric dipole whose dipole moment is proportional to the incident electric field [22]. Based on the vectorial Debye theory for high NA focussing [26] and the Mie theory to analytically work out the scattering of spherical particles [22], the scattered far field for incident linearly polarised light in the pupil plane of the second lens, (x_3, y_3), of Fig. 8.2 is given by [78]:

$$
\begin{aligned}
E_3 = &\left\{\frac{p_x}{2}\left[(1+\cos\theta)-(1-\cos\theta)\cos 2\varphi\right]-\frac{p_y}{2}(1-\cos\theta)\sin 2\varphi - p_z\sin\theta\cos\varphi\right\}\boldsymbol{i}\\
&+\left\{\frac{p_y}{2}\left[(1+\cos\theta)+(1-\cos\theta)\cos 2\varphi\right]-\frac{p_x}{2}(1-\cos\theta)\sin 2\varphi - p_z\sin\theta\sin\varphi\right\}\boldsymbol{j},
\end{aligned}
\tag{8.1}
$$

where E_3 gives the electric field required to analyse the polarisation of light. p_x, p_y and p_z are the Cartesian components of the electric dipole moment, and $\boldsymbol{i}$ and $\boldsymbol{j}$ are unit vectors in the x and y directions, respectively. Eq. (8.1) is expressed in spherical polar coordinates in r, θ and φ as defined in Fig. 8.2. For light linearly polarised in the $\boldsymbol{i}$ direction and incident on the objective lens, the dipole moment is given by [78]:

$$
\boldsymbol{p} = \left[I_0(v,\alpha)+I_2(v,\alpha)\cos 2\psi\right]\boldsymbol{i} + I_2(v,\alpha)\sin 2\psi\,\boldsymbol{j} - 2jI_1(v,\alpha)\cos\psi\,\boldsymbol{k}, \tag{8.2}
$$

where v is the normalised optical coordinate given by Eq. (2.35), which represents the scanning coordinates in the object plane along with the angle ψ, and α is the semi-aperture angle of the lens. The integrals I_0, I_1 and I_2 are given by [78]:

$$
\begin{aligned}
I_0(v,\alpha) &= \int_0^\alpha \cos^{\frac{1}{2}}\theta\sin\theta\,(1+\cos\theta)\,J_0\left(\frac{v\sin\theta}{\sin\alpha}\right)\,\mathrm{d}\theta,\\
I_1(v,\alpha) &= \int_0^\alpha \cos^{\frac{1}{2}}\theta\sin^2\theta J_1\left(\frac{v\sin\theta}{\sin\alpha}\right)\,\mathrm{d}\theta,\\
I_2(v,\alpha) &= \int_0^\alpha \cos^{\frac{1}{2}}\theta\sin\theta\,(1-\cos\theta)\,J_2\left(\frac{v\sin\theta}{\sin\alpha}\right)\,\mathrm{d}\theta,
\end{aligned}
\tag{8.3}
$$

where J_0, J_1 and J_2 are the zero, first and second order Bessel functions of the first kind, respectively. Since the dipole moment $\boldsymbol{p}$ in Eq. (8.2) is considered for light polarised in the $\boldsymbol{i}$ direction, the crossed polar far field image is obtained by looking at the $\boldsymbol{j}$ component of E_3 in Eq. (8.1) and calculating the intensity using Eq. (2.9).

Fig. 8.3 shows the simulated crossed polar images of a dielectric scatterer in the

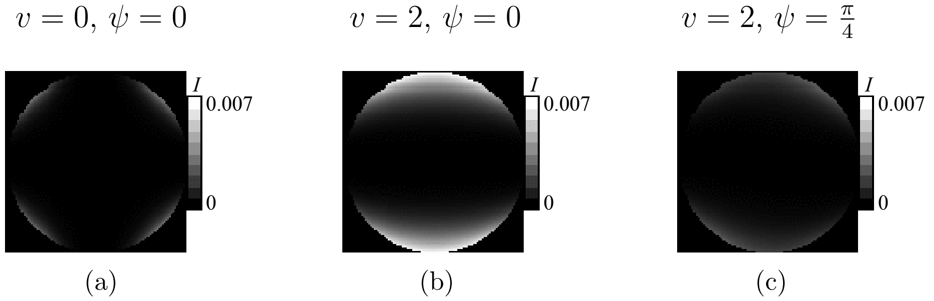

Figure 8.3: Simulated crossed polar images of a dielectric scatterer in the back focal plane at various scanning positions. Intensity pattern changes when the focus is shifted away from the scatterer in the transverse plane. (v, ψ) represent the polar scanning coordinates in the object plane.

back focal plane of a high NA objective lens for light scattered from a single dielectric scatterer. The lens had an NA of 1.2, the illumination wavelength was 633nm and the immersion medium refractive index was 1.33 for water. Fig. 8.3a shows the intensity when the sub-resolution scatterer was in focus. The maximum intensity was observed to be less than 0.7% of the normalised pupil intensity without polarisers. The pupil was mostly unfilled, with light being concentrated mainly at the four corners. This light distribution cannot be used effectively for wavefront sensing as much of the pupil is not illuminated. Fig. 8.3b shows that on shifting the focus to $v = 2$ along the x-axis, the field was observed to become stronger and more light filled the pupil along $\rho = \pm\frac{\pi}{2}$. However, the centre of the pupil was still unfilled along the x-axis. Shifting the focus to $v = 2$ and along $\psi = \frac{\pi}{4}$ radians revealed a slight asymmetric field and reduction in the strength, shown in Fig. 8.3c.

From this analysis, it can be deduced that for a scattering specimen probed in a polarisation microscope, scanning the specimen and time-averaging the back focal plane image should provide a field with more light filling the pupil. Since specularly reflected light is filtered out using crossed polarisers and only scattered light is obtained, it can be expected that the WS measurements will be less affected by the dual-pass phenomenon.

8.2 Experimental Design

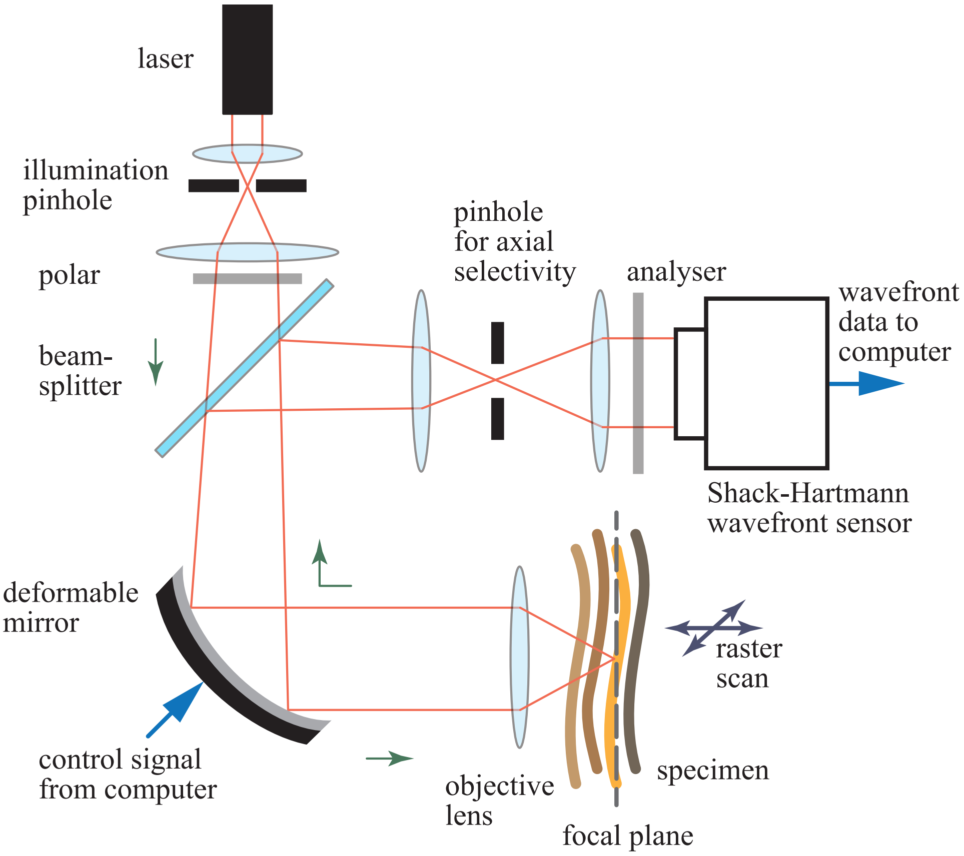

Figure 8.4: Simple schematic of a dual-pass wavefront sensing system with crossed polarisers. Polar in illumination path ensures illumination beam is linearly polarised. Analyser in detection path filters out specular reflections and allows only backscattered light to reach the SHWS.

A polarisation dual-pass wavefront sensing set-up was achieved by placing a linear polariser in the illumination path and an analyser before the SHWS in the detection path, as shown in Fig. 8.4. The polariser ensured the illumination beam from the laser was linearly polarised. Using a mirror as the specimen, the analyser was oriented to cut off the light reflected back in the detection path. It is however, impossible to filter out all the light since polarisers are not perfect. Therefore, the analyser in the set-up ensured that minimal specularly reflected light was transmitted to the SHWS. The contrast thus achieved is characterised by the extinction ratio, which is defined as the ratio of the intensity of light transmitted between parallel polarisers to that transmitted between crossed polarisers [79, 78, 80]. The extinction ratio for light collected at the

SHWS was found to be approximately 70 when an axial selectivity pinhole was absent. About 50 spots were registered on the SHWS when crossed polarisers were used, whereas the 540 lenslet domains for the defined 4.1mm pupil registered spots without polarisation filtering.

Since the placing of the crossed polarisers ensured that most of the specular reflections were filtered out, scattered light was expected to fill the aperture of the SHWS. Similar to the case with asymmetric illumination and detection, it was expected that a lower proportion of even aberration modes and a higher proportion of odd aberration modes should be detected, as expected for a single-pass system.

8.3 Experimental Results

The experiments were conducted as outlined in Sec. 6.6.1. Aberrations were induced using the DM and the estimated aberrations detected by the SHWS were recorded for analysis. The following sections discuss the results from various scattering specimens.

8.3.1 Sample of 200nm Beads Suspended in Gelatine

The 200nm polystyrene bead sample was used as a specimen to study the behaviour of direct wavefront sensing in a dual-pass imaging using polarisation filtering. The parameters of the set-up remained the same as for the symmetric system in Sec. 6.8.2. Hence, the diameter of the aberration-free Airy disc was calculated to be 644nm, using Eq. (2.41). As the beads were much smaller than the aberration-free focal spot, they should behave approximately like point scatterers..

Fig. 8.5a shows the Hartmann spot pattern from the stationary bead sample. Axial selectivity was achieved using a 300μm pinhole. Comparing with the simulation results in Fig. 8.3, it can be seen that using crossed polarisers, light had been eliminated along the x-axis. Contrastingly, a few spots were observed at the centre of the spot pattern from the

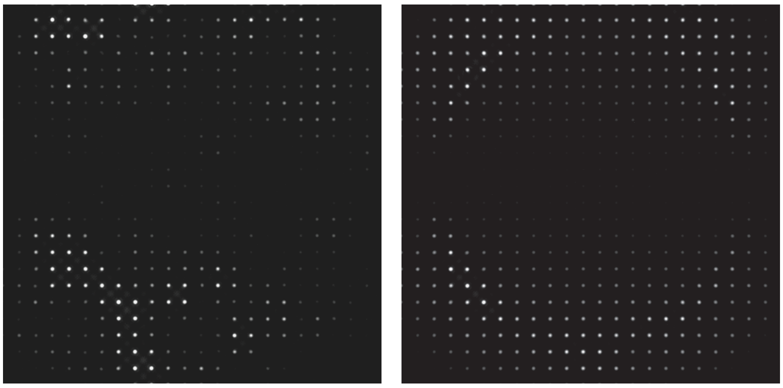
(a) (b)

Figure 8.5: Sample Hartmann spot patterns from light backscattered from a sample of 200nm beads suspended in gelatine. A 300μm pinhole was used for axial selectivity. Due to the use of crossed polarisers, there were a few dim spots at the centre of the aperture from backscattered light. (a) Hartmann spot pattern when the specimen was stationary. (b) Specimen was scanned and image was averaged to achieve a uniform spot pattern.

SHWS that resulted from depolarised scattered light and superposition of scattered light from nearby beads. The simulations also showed that by moving the focus laterally away from the dipole scatterer, the back focal plane of the objective was filled by light around the rim, but light was not present along the x-axis. Similarly, superposition of scattered light from multiple beads in the vicinity of the focal spot resulted in filling those areas of the SHWS aperture. A uniform spot pattern was achieved by time averaging using a suitable exposure of the sensor while the specimen was scanned and averaging consecutive frames captured by the SHWS, which is shown in Fig. 8.5b.

Fig. 8.6 shows the SHWS measurements for the even aberration modes of Z_5, Z_6 and Z_{11}. The measurements were repeated for the same specimen in the unfiltered set-up of Fig. 6.10, shown in black, and polarisation filtering set-up of Fig. 8.4, shown in red. The amount of DM-induced aberration is shown by the dashed line in the graphs.

The experiments were performed using a 300μm pinhole for axial selectivity. The exposure of the sensor shutter was set to 100ms for the unfiltered set-up. As expected, the crossed polarisers reduced the intensity of light significantly, so an exposure of 1361ms was used for the filtered set-up. In addition to time averaging in both set-ups, frame averaging was performed by taking 5 consecutive frames, and further averaging performed by recording 5 measurements for each Zernike mode amplitude induced by the DM.

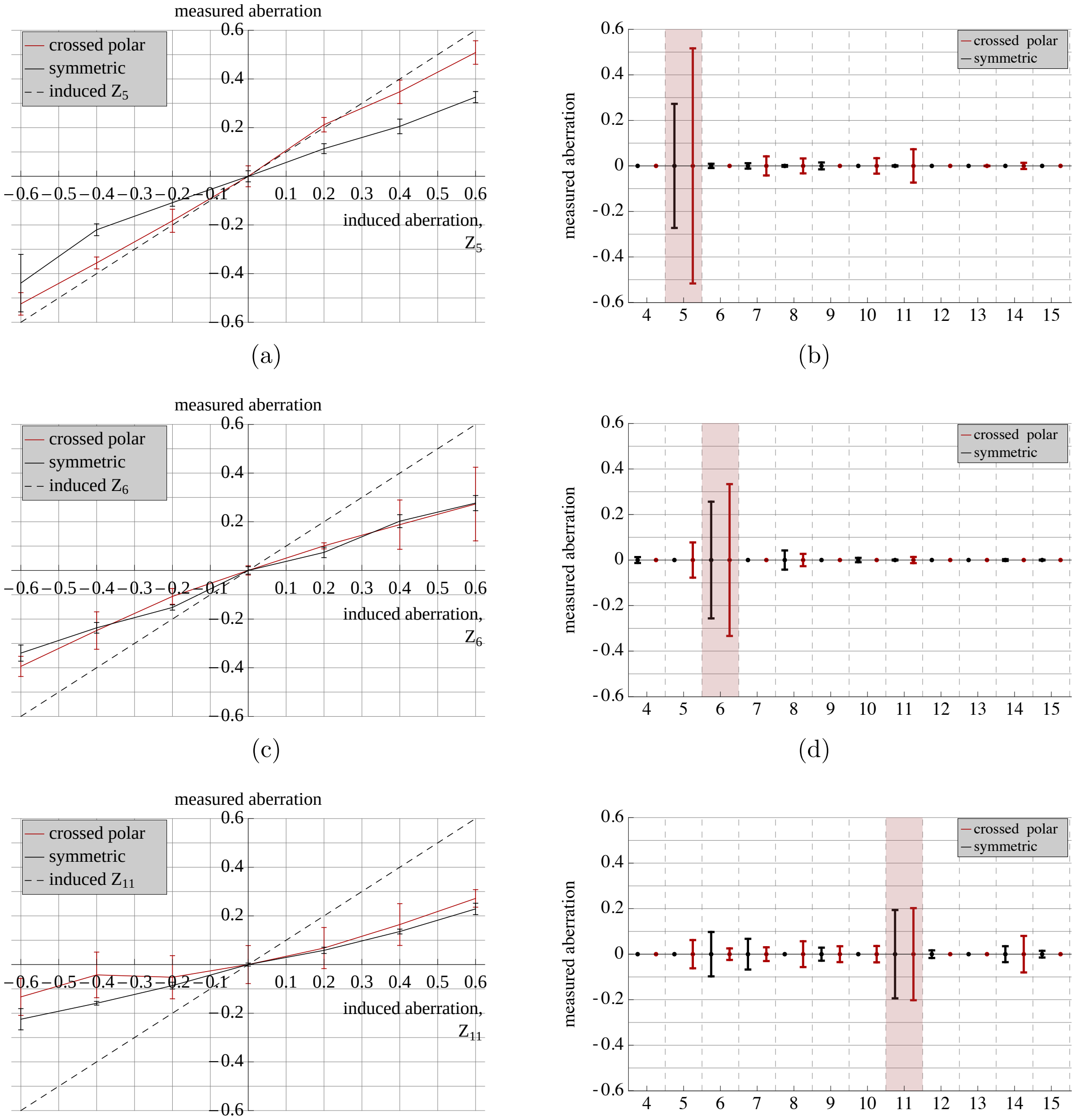

(a) (b)

(c) (d)

(e) (f)

Figure 8.6: SHWS measurements of even aberration modes Z_5, Z_6 and Z_{11}, respectively, which were induced by a DM and scattered back by a sample of 200nm beads suspended in gelatine. Polarisation filtering was used and compared with the results from the unfiltered set-up. (a), (c) and (e) Measured aberration as a function of induced aberration. (b), (d) and (f) Maximum measured amplitude of all Zernike modes, showing cross-talk between modes. The DM-induced Zernike modes are highlighted in the graphs.

The graphs show that the measurements of Z_6 and Z_{11} were similar for the unfiltered and filtered set-ups. However, a higher portion of Z_5 was detected using polarisation filtering, which the rotation of the astigmatism mode is responsible for. Fig. 8.7 shows the phase variation in the pupil plane due to astigmatism, coma and trefoil. The region approximately corresponding with the missing spots after filtering using the crossed polarisers is shown. In this region of the pupil, 12 – 13% of the spots were missing, which corresponded to 65 – 70 spots out of 540. The displacements of these spots were set to zero by the wavefront estimation software, thereby setting the phase gradient to zero. Since the spots are missing along the x-axis, data from available spots above the axis has to be used to estimate the position of the missing ones.

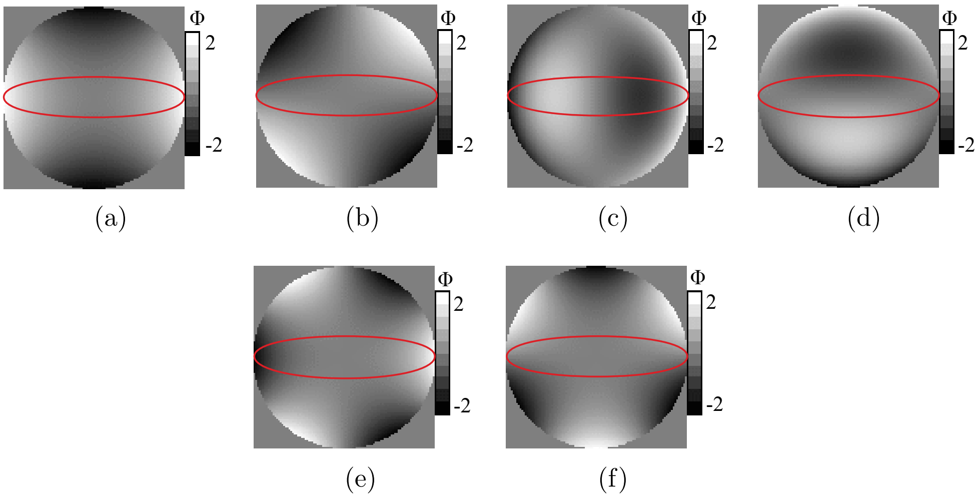

(a) (b) (c) (d)

(e) (f)

Figure 8.7: Phase in the pupil plane due to 0.6 RMS radian of astigmatisms: (a) Z_5 and (b) Z_6, comas: (c) Z_7 and (d) Z_8, trefoils: (e) Z_9 and (f) Z_{10}. The encircled region roughly corresponds with the region of missing spots in the crossed polar Hartmann spot pattern of Fig. 8.5b.

For Z_5, the phase is almost constant along the y direction in the encircled region of missing spots, and thus the phase gradient along y is close to zero. Therefore, a large estimation error did not occur for Z_5 by setting the phase gradient to zero in this region. For Z_6, there is a significant phase gradient along the y direction in the region of the missing spots. Consequently, the phase is flattened by setting the gradient to zero in the region and this has an effect on the measured coefficient. Cross-talk was observed to be small and comparable with the unfiltered versions for the even aberration modes.

Fig. 8.8 and Fig. 8.9 show the measurements of the odd aberration modes of coma and trefoil, respectively. Contrary to expectations, the measurements of the odd aberration modes using polarisation filtering were found to be smaller in magnitude in comparison with the measurements made with the unfiltered set-up. Clearly, the missing spots caused ambiguity in wavefront sensing, resulting in the smaller readings. Similar to

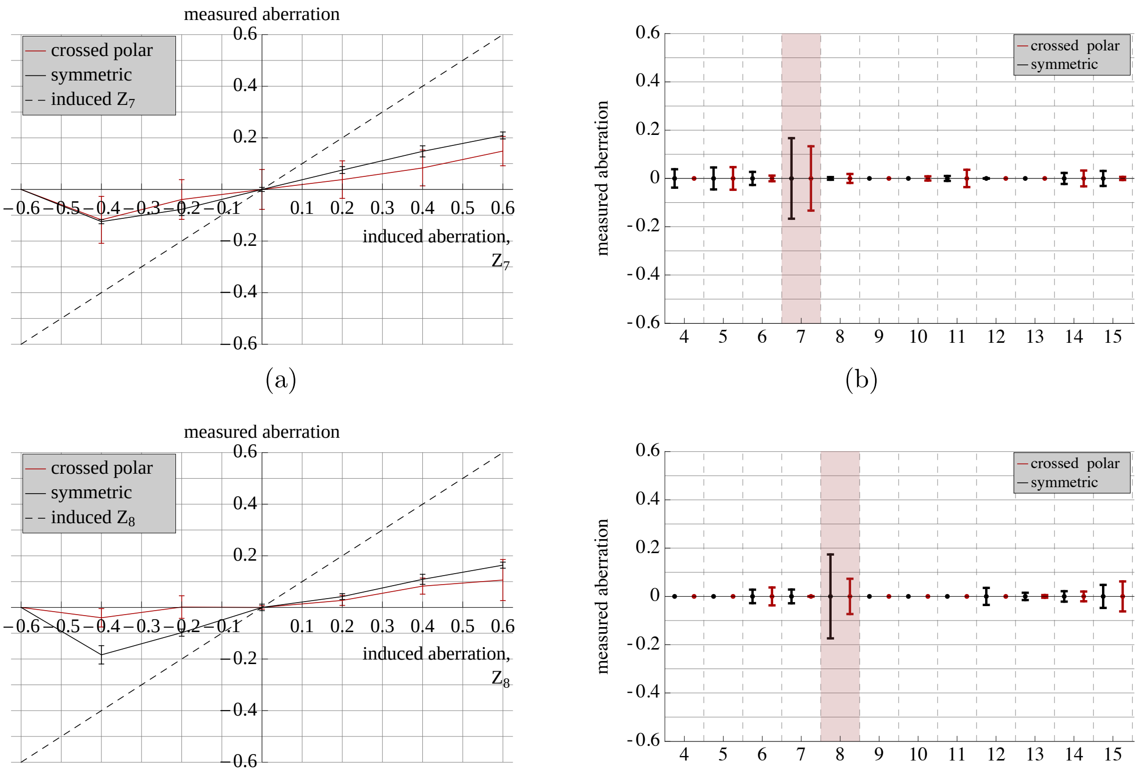

(a) (b)

(c) (d)

Figure 8.8: SHWS measurements of the odd aberration modes Z_7 and Z_8 (comas), respectively, which were induced by a DM and scattered back by a sample of 200nm beads suspended in gelatine. Polarisation filtering was used and compared with the results from the unfiltered set-up. (a) and (c) Measured aberration as a function of induced aberration. (b) and (d) Maximum measured amplitude of all Zernike modes, showing cross-talk between modes. The DM-induced Zernike modes are highlighted in the graphs.

the case of the astigmatisms, the phase along the y direction changes negligibly for Z_7, but changes from negative to positive value for Z_8 in the region of the missing spots, as Fig. 8.7 illustrates. Hence, a higher proportion of Z_7 was detected compared to Z_8.

The missing spots had a greater effect on the trefoil modes, Z_9 and Z_{10}, than the coma modes, Z_7 and Z_8, whereas a higher proportion of the trefoil modes was estimated for the unfiltered symmetric set-up. The estimation of the trefoil modes was observed to be nearly halved after filtering. In Fig. 8.7, the phase of Z_9 and Z_{10} can be seen to change more frequently between positive and negative values because of the three-fold structure of the aberration, resulting in this reduced estimation. There was negligible cross-talk during the estimation of the coma modes, but the missing spots caused a higher amount of cross-talk in the measurement of the trefoil modes.

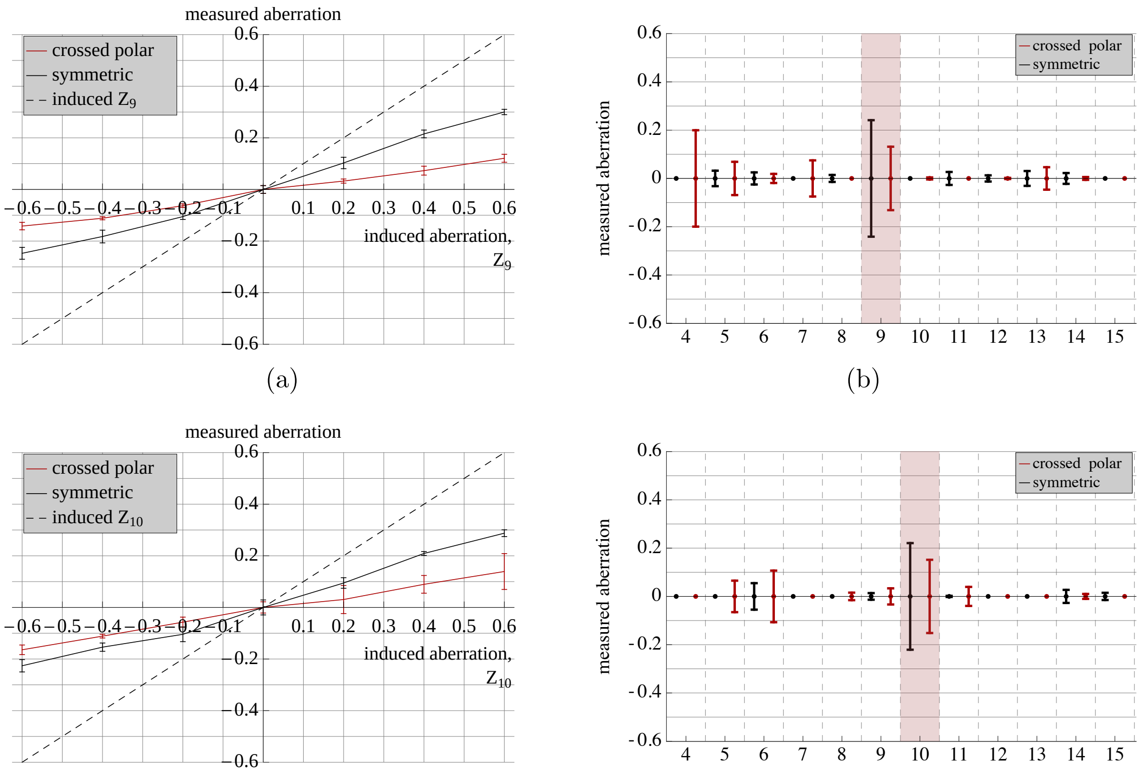

(a) (b)

(c) (d)

Figure 8.9: SHWS measurements of the odd aberration modes Z_9 and Z_{10} (trefoils), respectively, which were induced by a DM and scattered back by a sample of 200nm beads suspended in gelatine. Polarisation filtering was used and compared with the results from the unfiltered set-up. (a) and (c) Measured aberration as a function of induced aberration. (b) and (d) Maximum measured amplitude of all Zernike modes, showing cross-talk between modes. The DM-induced Zernike modes are highlighted in the graphs.

The standard deviation was less than ±0.04 radian in the unfiltered set-up, with the exception at -0.6 RMS radian of induced Z_5, where it was ±0.1 radian. This may have been due to some experimental error. However, the maximum standard deviation was observed to increase between ±0.09 to ±0.15 radian in the crossed polar set-up, arising from the estimation errors due to missing spots and low light.

Fig. 8.10 summarises the measurements made from the 200nm beads specimen. Due to the significant number of missing spots in the centre of the SHWS aperture, the Zernike modes with phase changes lying in the region of missing spots were prone to varied results. Hence, in the filtered system Z_5 yielded a higher reading compared to Z_6, and similar portions of coma and trefoil were detected. Contrastingly, in the unfiltered system, similar portions of Z_5 and Z_6 were detected, and higher portions of the trefoil

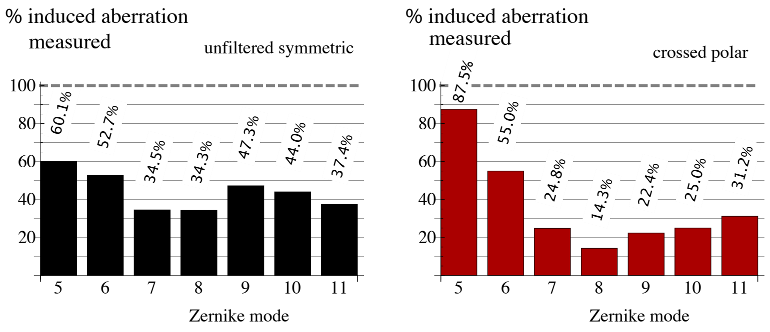

(a) (b)

Figure 8.10: Bar charts showing the percentages of induced aberrations detected by the SHWS from light backscattered from a sample of 200nm beads using (a) unfiltered and (b) polarisation filtered set-ups.

modes were detected compared to the coma modes.

8.3.2 Sample of Artificial Collagen

The effect of using polarisation filtering in direct wavefront sensing was tested using the artificial collagen sample. The unfiltered measurements were taken at 67ms exposure, averaging 5 frames, and recording 5 readings for each amplitude induced by the DM. When polarisation filtering was performed, the exposure was increased to 1361ms. A 300μm pinhole was used for axial selectivity.

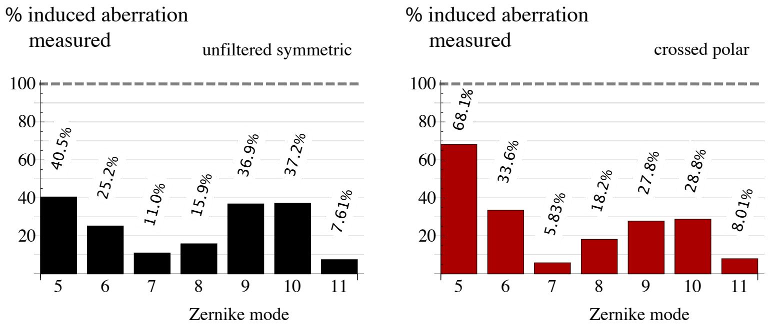

(a) (b)

Figure 8.11: Bar charts showing the percentages of induced aberrations detected by the SHWS from light backscattered from a sample of collagen using (a) unfiltered and (b) polarisation filtered set-ups.

Fig. 8.11 sums up the findings from the experiment. Similar to the 200nm beads sample [Sec. 8.3.1], portions of the even aberrations modes of Z_6 and Z_{11} detected were found similar for both the unfiltered and filtered systems. The increase in the measurement of Z_5 was noted for the collagen sample as well. The measurement of the trefoil modes also decreased by a factor of about 1.3. With the collagen sample, 7 – 10% of the spots were missing, which meant around 38 – 54 spots were set to zero displacement by the SHWS software. The maximum standard deviation of the measurements for the unfiltered system was recorded at ±0.015, and that for the filtered system at ±0.02, which showed that the errors in the measurements in these particular experiments were low.

8.4 Conclusions

The results provided in this chapter showed that performing direct wavefront sensing on backscattered light that has been polarisation filtered may not provide an advantage over the conventional system described in Ch. 6. By cutting off specular reflections using crossed polarisers, the lack of light at the centre of the back focal plane caused ambiguity in wavefront estimation, particularly in the case of aberration modes that have phase changes in those regions of darkness. Consequently, lesser portions of the various aberration modes were detected by a SHWS contrary to expectations. As proposed in Sec. 7.4, a complex algorithm would be able to extrapolate the phase gradient values of the missing spots from the available data. While this would provide a good approximation in the case of smoothly varying, and particularly lower-order, aberrations, such an algorithm is still likely to fail if the phase variations are rapid and unpredictable.

The experiments showed that for the 200nm beads and the artificial collagen samples, the unfiltered system required exposure times of the sensor of 67ms and 100ms, respectively. These exposure times were sufficient for the time averaging in order to obtain a uniform Hartmann spot pattern for wavefront sensing. However, the use of crossed polarisers reduced the intensity of light impinging on the detector. Consequently, the sensor was set to use an exposure of 1361ms. In doing so, the sensor was more susceptible to background noise, which gave rise to higher errors in the measurements. Using a longer exposure, the wavefront estimation time was also increased by more than 13 times.

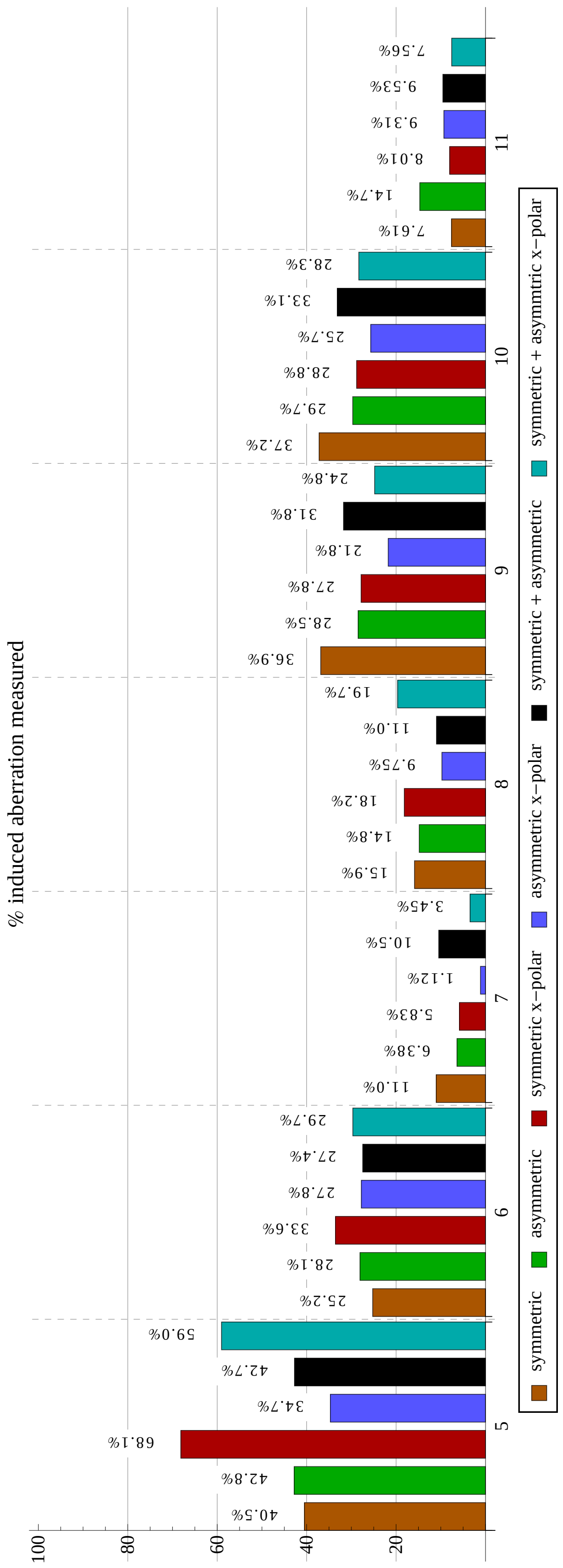

Figure 8.12: Bar chart comparing the percentages of induced aberrations detected by the SHWS from light backscattered from a sample of collagen for the symmetric, asymmetric, crossed polar set-ups and the combination of these different set-ups.

Some of the limitations of the symmetric, asymmetric and polarisation filtering set-ups could be overcome by combining these techniques. Fig. 8.12 shows a bar chart comparing the proportions of the different Zernike aberration modes from light backscattered from the sample of collagen. In addition to the data produced in Ch. 6, Ch. 7 and Ch. 8 for the symmetric, asymmetric and polarisation filtering techniques, respectively, the bar chart shows the data for polarisation filtering in asymmetric dual-pass system, combination of symmetric and asymmetric illumination and detection, and polarisation filtering in the combined symmetric and asymmetric dual-pass system.

Reiterating what was observed for the collagen sample, the detection of the even aberration modes, Z_5, Z_6 and Z_{11}, was slightly better using the asymmetric than the symmetric dual-pass set-up, represented by the left-most bars in brown and green, respectively, for each induced Zernike mode. For the odd aberration modes, Z_7 – Z_{10}, the estimated magnitudes of the modes decreased, contrary to what was expected from the theory. A combination of these two systems, whereby the specimen was illuminated by both the expanded and unexpanded beams, yielded measurements that where closer to the higher values attained from the individual set-ups. These results are represented by the black bars.

The use of polarisation filtering in the asymmetric illumination and detection system did not provide any advantage over the aforementioned systems. These results are shown by the blue bars. The measurements were similar for the even aberration modes, and smaller for the odd ones. Therefore, it would not be a very practical system to use.

Finally, the use of polarisation filtering in the combined symmetric and asymmetric dual-pass system gave similar results to the symmetric system with filtering as the symmetric system dominated the measurements. These results are given by the right-most cyan bars.

The polarisation filtering technique employed in these experiments using linearly polarised light resulted in too many missing spots, which in combination with the simple reconstruction algorithm, rendered too many estimation error. Therefore, this system may not be very practical. However, the number of missing spots could be reduced by using circularly polarised light and an appropriate analyser. For a dielectric point scatterer, this results in a circularly symmetric image in the back focal plane as opposed to the images shown in Fig. 8.3 [78, 81, 82], which fills the rim of the pupil. Some spots will still be missing in the centre of the pupil. But the reduction of missing spots, in conjunction with a better wavefront reconstruction algorithm, could give better estimations of phase aberrations.

Another possible combination of systems would be using the symmetric dual-pass set-up with polarisation filtering and the asymmetric dual-pass set-up without filtering. However, the combined system would require capturing an image from the individual system and combining them to get a Hartmann spot pattern for wavefront estimation. Ultimately, as the results were dominated by the higher measurements for the aforementioned combined systems, it can be expected that the measurements for this system would be dominated by the symmetric system with polarisation filtering, which yielded similar or higher proportions of the estimated aberrations.

Chapter 9

Adaptive Correction using Direct Wavefront Sensing in Biological Specimen Imaging

This chapter looks at adaptive correction using direct wavefront sensing. A sample of C. elegans was probed under the three variations of the dual-pass wavefront sensing system described in the preceding chapters. Adaptive correction was then attempted based on the aberration estimations made by the SHWS.

9.1 Experimental Results for a Sample of C. Elegans

The estimation of various Zernike aberration modes was investigated for light backscattered from a sample of C. elegans. Confocal images of the sample are shown in Fig. 9.4. The three adaptive optics set-ups — symmetric dual-pass, asymmetric dual-pass and polarisation filtering — described in the previous chapters were used. The aberrations were induced by the DM, backscattered by the sample, and detected by the SHWS.

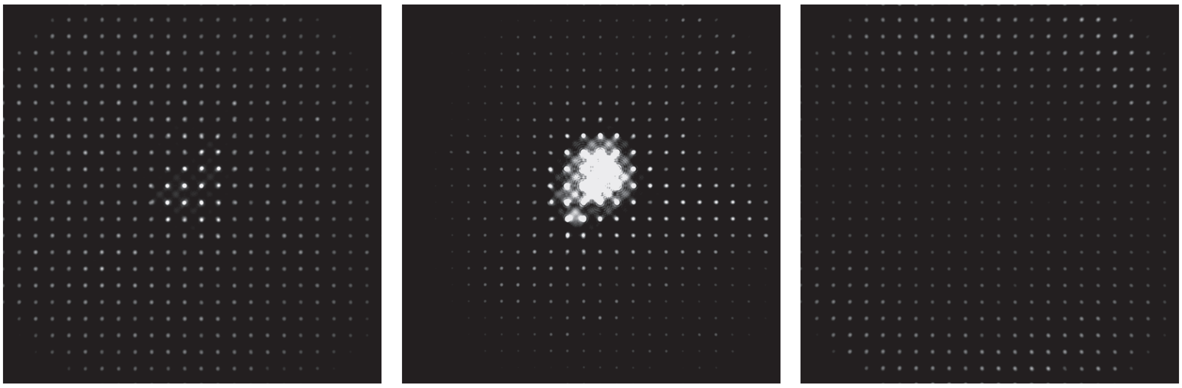
(a) (b) (c)

Figure 9.1: Sample Hartmann spot patterns from light backscattered from a sample of C. elegans in (a) a symmetric dual-pass set-up, (b) an asymmetric dual-pass set-up, and (c) a symmetric dual-pass set-up with polarisation filtering. A 600μm pinhole was used for axial selectivity. The specimen was scanned and image was averaged to achieve a uniform spot pattern in all three set-ups.

Fig. 9.1 shows sample Hartmann spot patterns from light backscattered from the sample of C. elegans for the three different optical configurations. The specimen provided uniform backscattering. In the symmetric set-up, around 1.5% of the spots were saturated when an exposure of 67ms was used on the SHWS CCD. Fig. 9.1a clearly illustrates that the few spots in the centre of the pupil are not hugely saturated so as to drastically shift the centroid of the spots. Hence, these spots can be used in the estimation process. These spots had arisen as a result of imaging the specimen close to the cover slip. Some of the light reflected back by the cover slip had passed through the axial selectivity pinhole. Subsequently, only 2% of the spots that were missing on account of being too dim were discarded during the experiment. Fig. 9.1b shows the highly saturated centre resulting from the asymmetric illumination. An exposure of 100ms was used on the sensor. In the asymmetric dual-pass system, 10 – 12% of the spots were discarded. Half of the discarded spots comprised of those saturated at the centre and the rest were missing. Fig. 9.1c shows the spot pattern obtained after polarisation filtering. Owing to filtering, a higher exposure of 1000ms was required on the SHWS to detect spots. The C. elegans sample has depolarised the light significantly to populate the centre of the pupil. Thus only 2 – 3% of the spots were too dim to be registered on the SHWS.

Fig. 9.2 shows the response of the SHWS to the DM-induced aberrations. One of

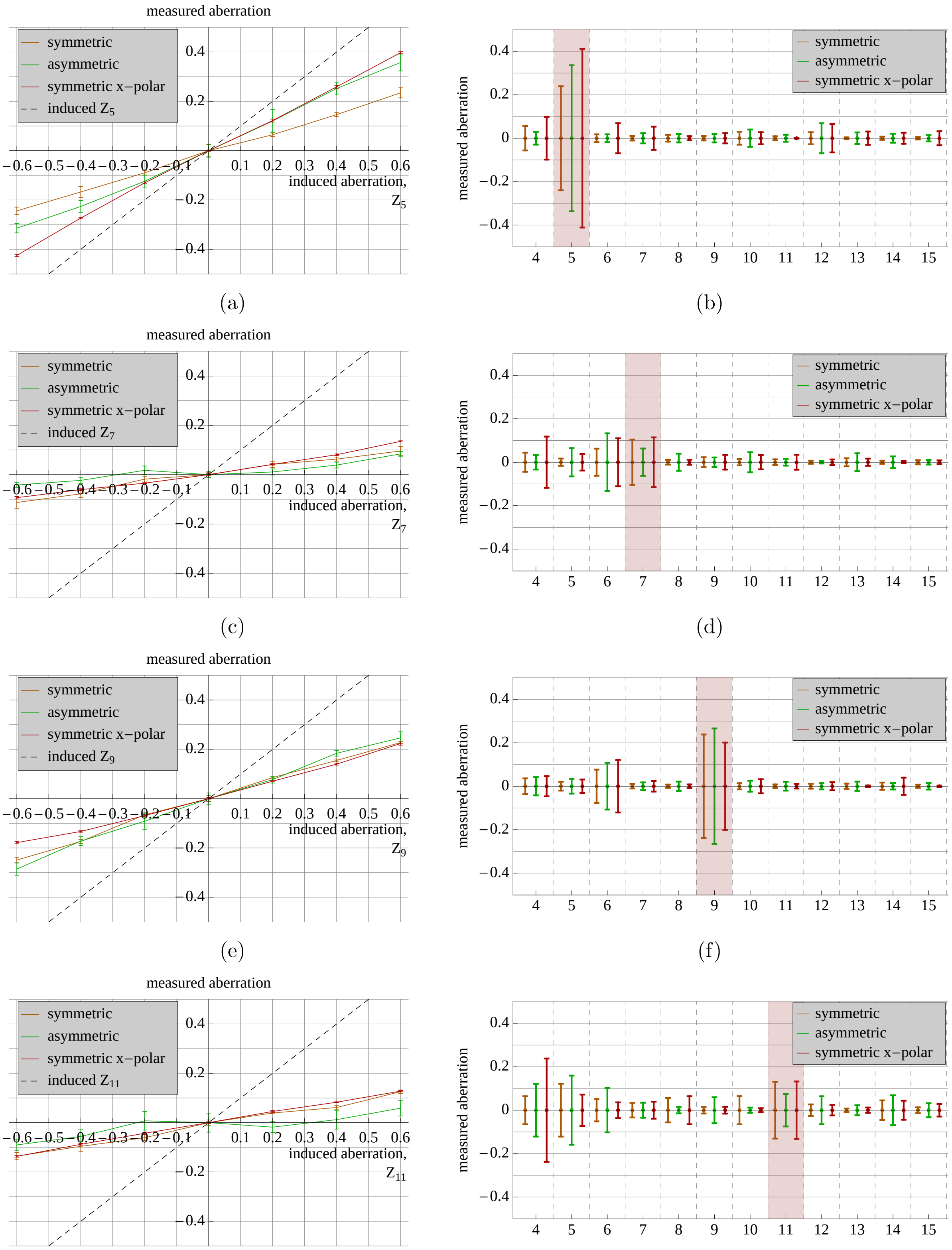

(a) (b)

(c) (d)

(e) (f)

(g) (h)

Figure 9.2: SHWS measurements of Z_5, Z_7, Z_9 and Z_{11}, which were induced by a DM and scattered back by a sample of C. elegans. Data from the symmetric and asymmetric dual-pass systems, and symmetric system with polarisation filtering are compared. (a), (c), (e) and (g) Measured aberration as a function of induced aberration. (b), (d), (f) and (h) Maximum measured amplitude of all Zernike modes, showing cross-talk between modes. The DM-induced Zernike modes are highlighted in the graphs.

the astigmatisms, comas and trefoils — Z_5, Z_7 and Z_9, respectively — are shown since they are representative of their rotated versions. The response to spherical aberration, Z_{11}, is also shown. A linear response was observed, similar to the 200nm beads [Sec. 6.8.2, Sec. 7.3.1, Sec. 8.3.1] and collagen samples [Sec. 6.8.3, Sec. 7.3.2, Sec. 8.3.2] tested in the previous chapters. Smaller proportions of the coma modes was detected compared to the trefoils due to the higher phase gradients of the former modes. Similar was the case for Z_{11}, which was detected at a lower proportion compared to the other even aberration modes of astigmatisms. The maximum standard deviation was observed to be ±0.025, ±0.045 and ±0.012 for the three respective configurations.

Using the asymmetric illumination and detection technique and the symmetric system with polarisation filtering, a high degree of cross-talk was observed for the odd aberration modes of coma and trefoil, and for spherical aberration. Such high proportions of cross-talk were not observed for the 200nm beads and collagen samples. These results suggest that these two optical set-ups may not be viable for wavefront sensing using backscattered light from a C. elegans sample.

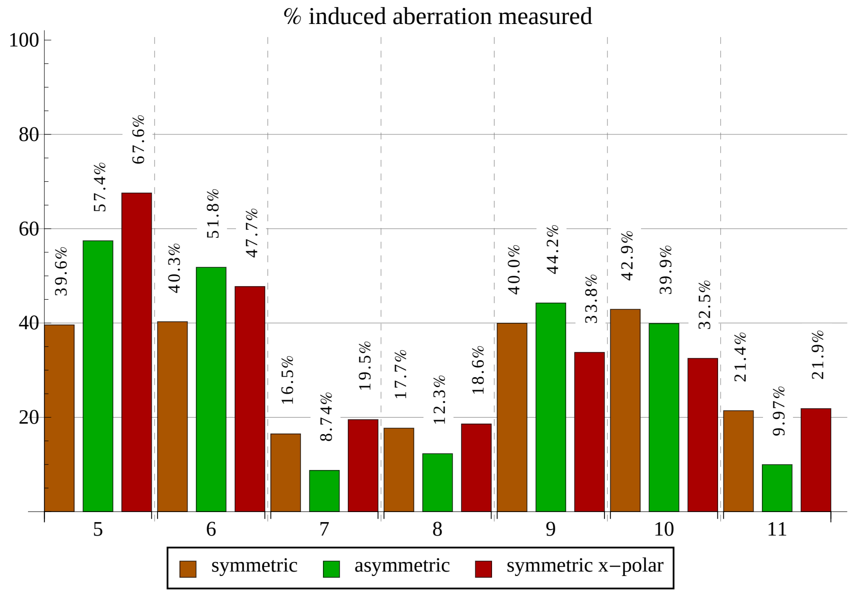

Figure 9.3: Bar chart comparing the percentages of induced aberrations detected by the SHWS from light backscattered from a sample of C. elegans for the symmetric and asymmetric dual-pass systems, and symmetric system with polarisation filtering.

Fig. 9.3 summarises the data from all three configurations by showing the proportions of each induced Zernike aberration mode detected by the SHWS. Comparing the data with Fig. 8.12, it can be noted that a higher portion of Z_7 and Z_{11} were detected when the C. elegans sample was probed using polarisation filtering. For the collagen sample probed using polarisation filtering, too many spots were missing along the x-axis, resulting in the wavefront reconstruction algorithm setting spots to their reference positions. However, the C. elegans sample yielded a considerably smaller number of missing spots that did not give rise to estimation errors caused by the algorithm.

9.2 Adaptive Correction

Adaptive correction was performed on the sample of C. elegans using the standard symmetric dual-pass optical system. The data for the symmetric set-up indicated that it was more robust in aberration estimation than the other techniques covered in this report. The system showed low numbers of missing and saturated spots, high repeatability as denoted by the small standard deviations, considerably lower cross-talk between Zernike aberration modes compared to the asymmetric dual-pass system and the symmetric set-up with polarisation filtering, and most importantly, good linearity in the measured versus induced aberrations data.

Fig. 9.4a shows the uncorrected confocal image of the C. elegans sample. The corresponding SHWS measurements are shown by the left-most bars in brown in Fig. 9.4b. At first, -0.6 radian of Z_5, -0.6 radian of Z_6 and -0.15 radian of Z_{11} were introduced to partially compensate for these detected even aberration modes. The confocal image subsequently obtained, shown in Fig. 9.4c, already showed an increase in the brightness of some features within the specimen. An increase in the total brightness by a factor of 2.3 was recorded simply by correcting the even aberration modes. The resulting coefficients detected by the SHWS are shown by the green bars in the centre of the bar chart. In the next step, 0.5 radian of Z_{10} was added to the DM to correct for that mode. A small decrease in the coefficient of Z_{10} was observed, as the red bars in the bar chart show. Simply by partially correcting for Z_{10}, the confocal image shown in Fig. 9.4d registered an increase in brightness by a factor of 3.3 compared to the uncorrected image, and a

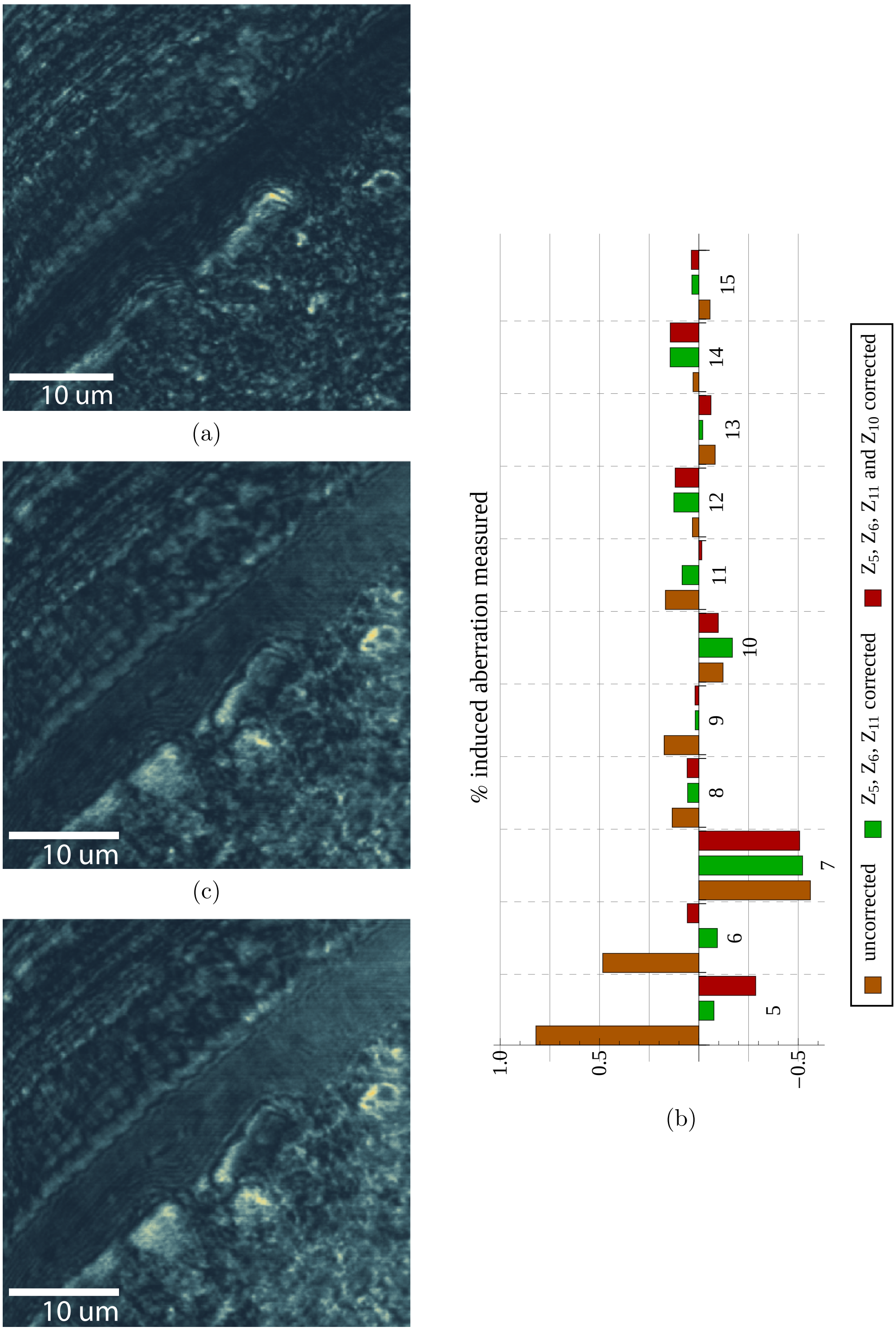

(a)

(c)

(d)

(b)

Figure 9.4: Demonstration of partial aberration correction of images of C. elegans using direct wavefront sensing. Confocal images of a sample of C. elegans: (a) without aberration correction, (c) after partial correction of modes Z_5, Z_6 and Z_{11}, and (d) after partial correction of mode Z_{10} in addition to the corrections in (c). (b) Zernike coefficients estimated by the SHWS for the uncorrected and partially corrected confocal images.

factor of 1.4 compared to the image after partial compensation of the even aberration modes. Approximately 0.5 radian of Z_7 was estimated by the SHWS, which equates to around 3 radians of the mode according to the data in Fig. 9.3. However, further correction was not attempted as the DM actuators were already saturated. Any further correction would have potentially added further aberrations.

The aberration coefficients may have varied across the field of view, but the measurements made by SHWS were averages over the image region. Hence, the correction coefficient is an average. Subsequently, while correction works in some regions, it may have made the image worse, or dimmer, for other parts of the specimen.

9.3 Conclusions

The results in this chapter demonstrated direct wavefront sensing in a dual-pass set-up for a real biological specimen, namely, C. elegans. The C. elegans sample behaved as a good scattering specimen. Linearity in the measurements of induced versus measured aberrations was observed, in line with the preceding experiments on the various model scattering specimens. Partial correction was shown to increase image brightness of particular features, indicating that the data can be used to perform adaptive correction in closed-loop.

Chapter 10

Conclusions and Discussion

This report showed how direct wavefront sensing could be performed from backscattered light in a dual-pass optical set-up in a microscope. Three different configurations were tested. The predicament of out-of-focus light was overcome by using an axial selectivity pinhole, which served much like the confocal pinhole in a confocal microscope, except that a larger aperture was used to ensure the phase variations were not cut off. It was found that the pinhole had a smoothing effect on the phase variation, and the maximum phase gradient allowed by a pinhole was directly proportional to its diameter [Sec. 6.4]. Accordingly, a larger pinhole is needed for higher-order aberrations or high amplitude aberrations. However, too large a pinhole would compromise the system by allowing out-of-focus light and causing multiple spots to form corresponding with each lenslet of the SHWS. The magnitude and order of aberrations detectable is thus restricted by the pinhole size.

Since backscattered light produces a non-uniform pupil image, homogeneity in the SHWS pupil was achieved by time averaging the pupil image. This was achieved, firstly, by setting the CCD camera of the SHWS to a long exposure time to allow time integration of the pupil while the specimen was being scanned on a stage, and secondly, by averaging multiple consecutive frames captured by the sensor [Sec. 6.3]. Subsequently, a uniform Hartmann spot pattern was obtained.

The conventional symmetric dual-pass system [Ch. 6] showed a linear response to the measurement of aberrations that were induced by a DM. The experiments showed that direct wavefront sensing using a SHWS in this manner is ill-suited for direct measurements since the actual magnitude of the aberrations cannot be estimated, but a proportion of the actual aberrations may be established. Such a system may be employed in a closed-loop adaptive optics system to compensate for aberrations in real-time, where the aberration coefficients can serve as feedback for the correction algorithm. The measurements varied from specimen to specimen, and also depended on the system optics. The data was prone to cross-talk owing to the ambiguity with backscattered light. It was also shown that the ambiguity in the measurements increased if the features of the scattering specimen were larger than the focal spot, and thus did not appear as point scatterers [Sec. 6.9.2].

The asymmetric illumination and detection set-up [Ch. 7] used an unexpanded, and consequently low NA, beam to illuminate the specimen. Backscattered light occupying the focal cone of the objective lens gave rise to high NA detection. Hence an asymmetric system was established. It was expected that as the narrow illumination beam was likely to be almost unaffected by phase aberrations, the backscattered light would provide a more true picture of the aberrations present in the specimen. However, similar proportions of aberrations were recorded as with the symmetric system. More so, higher proportions of cross-talk between aberration modes was observed. The spots in the centre of the pupil that were produced from the reflection of the low NA illumination light, saturated the sensor. These spots had to be discarded. To achieve high resolution imaging in the asymmetric illumination and detection set-up, shown in Fig. 7.2, a separate symmetric illumination and detection system has to be set up. This entails exact alignment of both the low and high NA illumination beams to ensure wavefront sensing is performed for the same region that is being imaged. Another complication arises in the imaging path as the imaging beam has to be distinguished by the detector from the wavefront sensing beam.

Using polarisation filtering in the symmetric dual-pass system [Ch. 8] enabled the filtering out of specular components of light scattered from the specimen. This would, in theory, prohibit the odd aberration cancelling effect in the dual-pass system. However, the use of polarising filtering had not significantly increased the proportions of odd aberration modes estimated. The wavefront reconstruction algorithm was partly involved in the estimation error as it simply set the local phase gradient to zero corresponding to missing spots. A better algorithm may have been able to extrapolate the phase gradients from the available data for smoothly varying phase variations. But in reality, aberrations are unpredictable and sudden changes in phase cannot be worked out by the reconstruction algorithm, especially given the number of missing spots observed at the centre of the pupil after polarisation filtering. For specimens, such as the C. elegans, that cause significant depolarisation upon scattering light, the amount of missing spots at the centre of pupil is reduced. Subsequently, higher proportions of odd aberrations, and equivalently of higher-order aberrations like spherical, were observed [Sec. 9.1].

For the asymmetric dual-pass system, the effect of illuminating the specimen off-axis by translating the unexpanded beam slightly away from the optical axis could be investigated. It was proposed that circular polarisation could be used to reduce the number of missing spots in the set-up using polarisation filtering. High dynamic range imaging [83] could be employed to all three configurations, particularly the system employing polarisation filtering, to attain information about the missing spots that are not picked up by the sensor for being too weak in intensity.

Adaptive correction was demonstrated for a sample of C. elegans. Partial correction of the even aberration modes of astigmatisms and spherical aberration already showed more than a two-fold increase in image brightness. A small amount of correction of the odd mode Z_{10} showed further enhancement. This would suggest that given the right instrument, for example, a DM with a higher stroke, near-diffraction limit could be achieved. It was observed that by taking the average coefficients over the entire field of view, the aberration correction had deteriorated the image in certain regions. Similar to computational adaptive optics involving mapping of the refractive indices of a specimen [84], the Zernike coefficients over subregions in the entire field of view could be mapped and accordingly corrected to diminish this effect.

In summary, direct wavefront sensing could be used in closed-loop AO systems where ample backscattered light is present. As the phase measurements depend on the the dual-pass configuration and specimen structure, the system is not feasible for direct quantitative measurements. However, provided a feedback system, the measurements could be used to minimise overall aberrations and restore optimum imaging performance of a system. The system does not require complex implementation, such as those using coherence-gating [20, 21, 44]. It provides a non-invasive approach to imaging by avoiding the use of fluorescent labelling [53, 54] or injecting reference beads to act as guide stars [49, 50, 51, 52].

Bibliography

[1] M. J. Booth, M. A. A. Neil, and T. Wilson, "Aberration correction for confocal imaging in refractive-index-mismatched media," *J. Microscopy*, vol. 192, pp. 90–98, November 1998.

[2] M. J. Booth, "Adaptive optics in microscopy," *Phil. Trans. R. Soc. A*, vol. 365, pp. 2829–2843, September 2007.

[3] R. K. Tyson, *Principles of Adaptive Optics.* Boca Raton, Florida: Academic Press, 2nd ed., 1998.

[4] R. A. Muller and A. Buffington, "Real-time correction of atmospherically degraded telescope images through image sharpening," *J. Opt. Soc. Am. A*, vol. 64, pp. 1200–1210, July 1974.

[5] M. J. Booth, M. A. A. Neil, R. Juškaitis, and T. Wilson, "Adaptive aberration correction in a confocal microscope," *Proc. Natl. Acad. Sci. USA*, vol. 99, pp. 5788–5792, April 2002.

[6] P. N. Marsh, D. Burns, and J. M. Girkin, "Practical implementation of adaptive optics in multiphoton microscopy," *Opt. Express*, vol. 11, pp. 1123–1130, May 2003.

[7] D. Débarre, E. J. Botcherby, M. J. Booth, and T. Wilson, "Adaptive optics for structured illumination microscopy," *Opt. Express*, vol. 16, pp. 9290–9305, June 2008.

[8] D. Débarre, M. J. Booth, and T. Wilson, "Image based adaptive optics through optimisation of low spatial frequencies," *Opt. Express*, vol. 15, pp. 8176–8190, June 2007.

[9] M. Feierabend, M. Rückel, and W. Denk, "Coherence-gated wave-front sensing in strongly scattering samples," *Opt. Lett.*, vol. 29, pp. 2255–2257, October 2004.

[10] S. Tuohy and A. Podoleanu, "Depth-resolved wavefront aberrations using a coherence-gated Shack-Hartmann wavefront sensor," *Opt. Express*, vol. 18, pp. 3458–3476, February 2010.

[11] L. Diaz-Santana and J. C. Dainty, "Effects of retinal scattering in the ocular double-pass process," *J. Opt. Soc. Am. A*, vol. 18, pp. 1437–1444, July 2001.

[12] M. Schwertner, M. J. Booth, and T. Wilson, "Characterizing specimen induced aberrations for high na adaptive optical microscopy," *Opt. Express*, vol. 12, pp. 6540–6552, December 2004.

[13] W. Denk, J. Strickler, and W. Webb, "Two-photon laser scanning fluorescence microscopy," *Science*, vol. 248, pp. 73–76, April 1990.

[14] J. W. Goodman, *Introduction to Fourier Optics.* Greenwood Village, Colorado: Roberts and Company Publishers, 3rd ed., 2005.

[15] J. Schwiegerling and D. R. Neal, *Historical development of the Shack-Hartmann wavefront sensor*, pp. 132–139. SPIE, 2005.

[16] J. W. Hardy, *Adaptive Optics for Astronomical Telescopes.* New York: Oxford University Press, 1998.

[17] J. A. Koch, R. W. Presta, R. A. Sacks, R. A. Zacharias, E. S. Bliss, M. J. Dailey, M. Feldman, A. A. Grey, F. R. Holdener, J. T. Salmon, L. G. Seppala, J. S. Toeppen, L. V. Atta, B. M. V. Wonterghem, W. T. Whistler, S. E. Winters, and B. W. Woods, "Experimental comparison of a Shack-Hartmann sensor and a phase-shifting interferometer for large-optics metrology applications," *Appl. Opt.*, vol. 39, pp. 4540–4546, September 2000.

[18] J. L. Beverage, R. V. Shack, and M. R. Descour, "Measurement of the three-dimensional microscope point spread function using a Shack-Hartmann wavefront sensor," *J. Microscopy*, vol. 205, pp. 61–75, January 2002.

[19] J. Liang, B. Grimm, S. Goelz, and J. F. Bille, "Objective measurement of wave aberrations of the human eye with the use of a Hartmann-Shack wave-front sensor," *J. Opt. Soc. Am. A*, vol. 11, pp. 1949–1957, July 1994.

[20] M. Rueckel, J. A. Mack-Bucher, and W. Denk, "Adaptive wavefront correction in two-photon microscopy using coherence-gated wavefront sensing," *Proc. Natl. Acad. Sci. USA*, vol. 103, pp. 17137–17142, November 2006.

[21] M. Rueckel and W. Denk, "Properties of coherence-gated wavefront sensing," *J. Opt. Soc. Am. A*, vol. 24, pp. 3517–3529, November 2007.

[22] M. Born and E. Wolf, *Principles of Optics.* Cambridge University Press, 7th ed., 1999.

[23] E. Hecht, *Optics.* Addison Wesley, 4th ed., 2002.

[24] T. Wilson and C. J. R. Sheppard, *Theory and Practice of Scanning Optical Microscopy.* Academic Press, 1984.

[25] T. Wilson, *Confocal Microscopy.* London: Academic Press, 1990.

[26] M. Gu, *Advanced Optical Imaging Theory.* Springer, 2000.

[27] C. W. Oates and M. Young, "Microscope objectives, cover slips, and spherical aberration," *Appl. Opt.*, vol. 26, pp. 2043–2043, June 1987.

[28] M. J. Booth and T. Wilson, "Refractive-index-mismatch induced aberrations in single-photon and two-photon microscopy and the use of aberration correction," *J. Biomed. Opt.*, vol. 6, pp. 266–272, July 2001.

[29] K. Carlsson, "The influence of specimen refractive index, detector signal integration, and non-uniform scan speed on the imaging properties in confocal microscopy," *J. Microscopy*, vol. 163, pp. 167–178, August 1991.

[30] C. J. R. Sheppard and T. Po, "Effects of specimen refractive index on confocal imaging," *J. Microscopy.*, vol. 185, pp. 366–374, March 1997.

[31] T. D. Visser, J. L. Oud, and G. J. Brakenhoff, "Refractive index and axial distance measurements in 3-d microscopy," *Optik*, vol. 90, no. 1, pp. 17–19, 1992.

[32] H. Jacobsen and S. W. Hell, "Effect of the specimen refraction index on the imaging of a confocal fluorescence microscope employing high aperture oil immersion lenses," *Bioimaging*, vol. 3, pp. 39–47, January 1995.

[33] P. J. Shaw and D. J. Rawlins, "The point-spread function of a confocal microscope: its measurement and use in deconvolution of 3-d data," *J. Microscopy*, vol. 163, pp. 151–166, August 1991.

[34] R. Cubalchini, "Modal wave-front estimation from phase derivative measurements," *J. Opt. Soc. Am. A*, vol. 69, pp. 972–977, July 1979.

[35] W. J. Tango, "The circle polynomials of zernike and their application in optics," *Appl. Phys.*, vol. 13, pp. 327–332, February 1977.

[36] R. J. Noll, "Zernike polynomials and atmospheric turbulence," *J. Opt. Soc. Am. A*, vol. 66, pp. 207–211, March 1976.

[37] W. H. Southwell, "Wave-front estimation from wave-front slope measurements," *J. Opt. Soc. Am.*, vol. 70, pp. 998–1006, August 1980.

[38] M. A. A. Neil, M. J. Booth, and T. Wilson, "New modal wave-front sensor: a theoretical analysis," *J. Opt. Soc. Am. A*, vol. 17, pp. 1098–1107, June 2000.

[39] V. N. Mahajan, "Zernike circle polynomials and optical aberrations of systems with circular pupils," *Appl. Opt.*, vol. 33, pp. 8121–8121, December 1994.

[40] D. R. Neal and J. Mansell, "Application of Shack-Hartmann wavefront sensors to optical system calibration and alignment," in *Proceedings of the 2nd International Workshop on Adaptive Optics for Industry and Medicine* (G. Love, ed.), World Scientific, 2000.

[41] P. Artal, S. Marcos, R. Navarro, and D. R. Williams, "Odd aberrations and double-pass measurements of retinal image quality," *J. Opt. Soc. Am. A*, vol. 12, pp. 195–201, February 1995.

[42] P. Artal, I. Iglesias, N. López-Gil, and D. G. Gree, "Double-pass measurements of the retinal-image quality with unequal entrance and exit pupil sizes and the reversibility of the eye's optical system," *J. Opt. Soc. Am. A*, vol. 12, pp. 2358–2366, October 1995.

[43] M. Losada and R. Navarro, "Point spread function of the human eye obtained by a dual double-pass method," *Pure and Appl. Opt.*, vol. 7, pp. L7–L13, July 1998.

[44] R. Fiolka, K. Si, and M. Cui, "Complex wavefront corrections for deep tissue focusing using low coherence backscattered light," *Opt. Express*, vol. 20, pp. 16532–16543, July 2012.

[45] J. Tang, R. Germain, and M. Cui, "Superpenetration optical microscopy by iterative multiphoton adaptive compensation technique," *Proc. Natl. Acad. Sci. USA*, vol. 109, pp. 8434–8439, May 2012.

[46] I. Vellekoop and A. Mosk, "Focusing coherent light through opaque strongly scattering media," *Opt. Lett.*, vol. 32, pp. 2309–2311, August 2007.

[47] I. Vellekoop and A. Mosk, "Phase control algorithms for focusing light through turbid media," *Opt. Comm.*, vol. 281, pp. 3071–3080, February 2008.

[48] O. Katz, E. Small, Y. Bromberg, and Y. Silberberg, "Focusing and compression of ultrashort pulses through scattering media," *Nature Photonics*, vol. 5, pp. 372–377, June 2011.

[49] R. Jorand, G. L. Corre, J. Andilla, A. Maandhui, C. Frongia, V. Lobjois, B. Ducommun, and C. Lorenzo, "Deep and clear optical imaging of thick inhomogeneous samples," *PloS one*, vol. 7, p. e35795, April 2012.

[50] O. Azucena, J. Crest, S. Kotadia, W. Sullivan, X. Tao, M. Reinig, D. Gavel, S. Olivier, and J. Kubby, "Adaptive optics wide-field microscopy using direct wavefront sensing," *Opt. Lett.*, vol. 36, pp. 825–827, March 2011.

[51] P. Vermeulen, E. Muro, T. Pons, V. Loriette, and A. Fragola, "Adaptive optics for fluorescence wide-field microscopy using spectrally independent guide star and markers," *J. Biomed. Opt.*, vol. 16, p. 076019, July 2011.

[52] X. Tao, B. Fernandez, O. Azucena, M. Fu, D. Garcia, Y. Zuo, D. Chen, and J. Kubby, "Adaptive optics confocal microscopy using direct wavefront sensing," *Opt. Lett.*, vol. 36, pp. 1062–1064, April 2011.

[53] X. Tao, O. Azucena, M. Fu, Y. Zuo, D. Chen, and J. Kubby, "Adaptive optics microscopy with direct wavefront sensing using fluorescent protein guide stars," *Opt. Lett.*, vol. 36, pp. 3389–3391, September 2011.

[54] X. Tao, J. Crest, S. Kotadia, O. Azucena, D. Chen, W. Sullivan, and J. Kubby, "Live imaging using adaptive optics with fluorescent protein guide-stars," *Opt. Express*, vol. 20, pp. 15969–15982, July 2012.

[55] R. Aviles-Espinosa, J. Andilla, R. Porcar-Guezenec, O. Olarte, M. Nieto, X. Levecq, D. Artigas, and P. Loza-Alvarez, "Measurement and correction of in vivo sample aberrations employing a nonlinear guide-star in two-photon excited fluorescence microscopy," *Biomed. Opt. Express*, vol. 2, pp. 3135–3149, October 2011.

[56] J. Cha, J. Ballesta, and P. So, "Shack-Hartmann wavefront-sensor-based adaptive optics system for multiphoton microscopy," *J. Biomed. Opt.*, vol. 15, p. 046022, July/August 2010.

[57] L. Seifert, J. Liesener, and H. Tiziani, "The adaptive Shack-Hartmann sensor," *Opt. Comm.*, vol. 216, pp. 313–319, February 2003.

[58] L. Hu, L. Xuan, D. Li, Z. Cao, Q. Mu, Y. Liu, Z. Peng, and X. Lu, "Wavefront correction based on a reflective liquid crystal wavefront sensor," *J. Opt. A: Pure Appl. Opt.*, vol. 11, p. 015511, January 2009.

[59] B. L. Roux, J. Coyne, and R. Ragazzoni, "Hierarchical wave-front sensing," *Appl. Opt.*, vol. 44, pp. 171–177, January 2005.

[60] A. Corbett, T. Wilkinson, J. Zhong, and L. Diaz-Santana, "Designing a holographic modal wavefront sensor for the detection of static ocular aberrations," *J. Opt. Soc. Am. A*, vol. 24, pp. 1266–1275, May 2007.

[61] F. Ghebremichael, G. Andersen, and K. Gurley, "Holography-based wavefront sensing," *Appl. Opt.*, vol. 47, pp. A62–A69, February 2008.

[62] R. Bhatt, S. Mishra, D. Mohan, and A. Gupta, "Direct amplitude detection of zernike modes by computer-generated holographic wavefront sensor: Modeling and simulation," *Opt. and Lasers in Eng.*, vol. 46, pp. 428–439, June 2008.

[63] G. Andersen, L. Dussan, F. Ghebremichael, and K. Chen, "Holographic wavefront sensor," *Opt. Eng.*, vol. 48, p. 085801, August 2009.

[64] R. Ragazzoni, "Pupil plane wavefront sensing with an oscillating prism," *J. Mod. Opt.*, vol. 43, no. 2, pp. 289–293, 1996.

[65] A. Vyas, M. B. Roopashree, and B. R. Prasad, "Optimization of existing centroiding algorithms for Shack Hartmann sensor," *NAC-CISS*, pp. 400–405, April 2009.

[66] A. Vyas, M. B. Roopashree, and B. R. Prasad, "Performance of centroiding algorithms at low light level conditions in adaptive optics," *Proc. Intl. Conf. Advances in Recent Technologies in Communication and Computing*, pp. 366–369, 2009.

[67] D. R. Neal, J. Copland, and D. Neal, "Shack-Hartmann wavefront sensor precision and accuracy," *Proc. SPIE*, vol. 4779, pp. 148–160, November 2002.

[68] K. L. Baker and M. M. Moallem, "Iteratively weighted centroiding for Shack-Hartmann wave-front sensors," *Opt. Express*, vol. 15, pp. 5147–5159, April 2007.

[69] L. A. Poyneer, D. W. Palmer, K. N. LaFortune, and B. Bauman, "Experimental results for correlation-based wavefront sensing," *Proc. SPIE*, vol. 5894, August 2005.

[70] S. Thomas, T. Fusco, A. Tokovinin, M. Nicolle, V. Michau, and G. Rousset, "Comparison of centroid computation algorithms in a Shack-Hartmann sensor," *Mon. Not. R. Astron. Soc.*, vol. 371, pp. 323–336, April 2006.

[71] J. Herrmann, "Cross coupling and aliasing in modal wave-front estimation," *J. Opt. Soc. Am.*, vol. 71, pp. 989–992, August 1981.

[72] R. P. Grosso and M. Yellin, "The membrane mirror as an adaptive optical element," *J. Opt. Soc. Am.*, vol. 67, pp. 399–406, March 1977.

[73] C. Paterson, I. Munro, and J. Dainty, "A low cost adaptive optics system using a membrane mirror," *Opt. Express*, vol. 6, pp. 175–185, April 2000.

[74] B. Wallace, P. Hampton, C. Bradley, and R. Conan, “Evaluation of a mems deformable mirror for an adaptive optics test bench,” *Opt. Express*, vol. 14, pp. 10132–10138, October 2006.

[75] E. Dalimier and C. Dainty, “Comparative analysis of deformable mirrors for ocular adaptive optics,” *Opt. Express*, vol. 13, pp. 4275–4285, May 2005.

[76] M. J. Booth, T. Wilson, H. Sun, T. Ota, and S. Kawata, “Methods for the characterization of deformable membrane mirrors,” *Appl. Opt.*, vol. 44, pp. 5131–5139, August 2005.

[77] R. Navarro and M. A. Losada, “Phase transfer and point-spread function of the human eye determined by a new asymmetric double-pass method,” *J. Opt. Soc. Am. A*, vol. 12, pp. 2385–2392, November 1995.

[78] T. Wilson, R. Juškaitis, and P. Higdon, “The imaging of dielectric point scatterers in conventional and confocal polarisation microscopes,” *Opt. Comm.*, vol. 141, pp. 298–313, September 1997.

[79] P. Higdon, R. Juškaitis, and T. Wilson, “The effect of detector size on the extinction coefficient in confocal polarization microscopes,” *J. Microscopy*, vol. 187, pp. 8–11, July 1997.

[80] T. Wilson, P. Török, and P. Higdon, “The effect of detector size on the signal-to-noise ratio in confocal polarized light microscopy,” *J. Microscopy*, vol. 189, pp. 12–14, January 1998.

[81] P. Török, P. Higdon, and T. Wilson, “On the general properties of polarised light conventional and confocal microscopes,” *Opt. Comm.*, vol. 148, pp. 300–315, March 1998.

[82] T. Wilson, F. Massoumian, and R. Juškaitis, “Generation and focusing of radially polarized electric fields,” *Opt. Eng.*, vol. 42, pp. 3088–3089, November 2003.

[83] J. Vargas, L. González-Fernandez, J. Quiroga, and T. Belenguer, “Shack–Hartmann centroid detection method based on high dynamic range imaging and normalization techniques,” *Appl. Opt.*, vol. 49, pp. 2409–2416, May 2010.

[84] Z. Kam, B. Hanser, M. Gustafsson, D. Agard, and J. Sedat, “Computational adaptive optics for live three-dimensional biological imaging,” *Proc. Natl. Acad. Sci. USA*, vol. 98, pp. 3790–3795, March 2001.